THE UNIVERSITY OF CHICAGO

DEFINING THE COMPARTMENTS OF THE YEAST ENDOMEMBRANE SYSTEM

A DISSERTATION SUBMITTED TO
THE FACULTY OF THE DIVISION OF THE BIOLOGICAL SCIENCES
AND THE PRITZKER SCHOOL OF MEDICINE
IN CANDIDACY FOR THE DEGREE OF
DOCTOR OF PHILOSOPHY

GRADUATE PROGRAM IN CELL AND MOLECULAR BIOLOGY

BY
KASEY J. DAY

CHICAGO, ILLINOIS
AUGUST 2017

If we assume we've arrived [at the truth],

we stop searching, we stop developing.

- Jocelyn Bell Burnell

TABLE OF CONTENTS

LIST OF FIGURES

LIST OF MOVIES

ACKNOWLEDGMENTS

First, I must thank Ben Glick, who may very well be the best boss I'll ever have. His guidance has helped me become a better writer, speaker, and thinker. He has taught me by example what it means to be a good member of the scientific community. How he manages to have an infinite supply of patience and optimism is a mystery, but I am very grateful for it.

Nike Bharucha and Sanny Papanikou provided the early laboratory guidance that made everything else possible. I am especially thankful to Sanny for helping me develop a love for microscopy and for being a wonderful friend. Ivy Fitzgerald developed several of the fluorescent proteins used to produce the stunning fluorescence images that follow. Jason Casler has been a marvelous source of conversation, ideas, and sanity checks. I am quite grateful that he decided to throw in his lot with the Glick lab. And many thanks to the other members of the lab, mostly for their hard work and helpfulness, but also for their comedic contributions.

My thesis committee has been very helpful. The discussions at our meetings have been one of the most enjoyable parts of my training. I'm also grateful to Vytas Bindokas and Christine Labno at the Light Microscopy Core for understanding that we refuse to settle for anything less than the impossible requirements of fast imaging, high resolution, and no photobleaching.

I also must thank my family for their encouragement. It's very nice to know that someone out there is unwaveringly confident in your ability to succeed—thanks, Mom and Dad. My siblings are the most terrific multilateral alliance of support. Finally, I owe a huge debt of gratitude to my husband, Josh, who has suffered through more long ramblings about the inner workings of the cell than any non-biologist should ever have to endure.

ABSTRACT

In this work, I addressed issues pertaining to endomembrane transport, compartment organization, and the mechanisms behind compartmentation. First, I assessed the role of COPI in organizing the Golgi. COPI is known to play an important role in Golgi transport, but its precise function in Golgi organization and maturation was previously unclear. A puzzling question was how a single type of coated vesicle could generate the multiple molecularly distinct stages of Golgi maturation. I used an "anchor-away" technique to rapidly inactivate COPI in yeast. In addition to defects in secretion and Golgi-to-ER retrograde traffic, COPI inactivation blocked the normal maturation kinetics of early Golgi proteins.

The continued cycling of late Golgi resident proteins revealed that COPI is a driving force behind early, but not late, Golgi maturation. COPI plays a part in recycling early Golgi proteins to younger cisternae. This work led to the proposal that AP-1 and clathrin-mediated transport is the most likely driver of late Golgi maturation.

I also aimed to clarify the poorly understood organization of yeast endosomes. The prior understanding in the field was that yeast possesses early and late endosomes, similar to the well documented endosomal organization of mammalian cells. However, key features of the mammalian endosomal network, including a clearly defined early endosome and endosomal maturation, had not been shown in yeast.

A spatiotemporal analysis of endosomal markers and endocytic cargo routes revealed three surprising findings: budding yeast lacks a mammalian-like early endosome, the yeast counterpart to the late endosome is a long-lived structure, and the yeast *trans*-Golgi network (TGN) serves the role of early and recycling endosomes. I directly visualized the targeting of endocytic material to the yeast TGN and showed that disrupting TGN exit blocks progress to downstream fates on the endocytic pathway. My results demonstrate that, remarkably, the TGN is the earliest destination for multiple types of endocytic cargoes.

These findings support a new, streamlined model for the yeast endomembrane system that has implications for the evolutionary relationship between yeast and mammalian endosomes.

The endomembrane system I describe for yeast resembles that of plants, in which the TGN also functions as an early endosome. It is possible that the early and recycling endosomal compartments and the endosomal maturation pathway represent evolutionarily novel features that permitted a more complex endosomal trafficking network in higher eukaryotes.

These studies involved a considerable amount of video microscopy to track fluorescently labeled endomembrane structures and to optimize imaging and processing methods. Temporal analysis is essential to understanding maturation, protein localization, and compartmental behavior. The movies associated with each chapter are included as supplementary files online. For reference, the first frame and a legend for each movie are provided at the end of their respective chapters.

CHAPTER 1

INTRODUCTION

Eukaryotic cells segregate functions in space and time among membrane-bound organelles. Membrane compartments include the endoplasmic reticulum (ER), Golgi complex, endosomes, lysosomes (called vacuoles in yeast), nucleus, peroxisomes, mitochondria, plastids (in plants), and plasma membrane. The Golgi complex and endosomes can be further subdivided into partially distinct functional compartments (Day et al., 2013; Huotari and Helenius, 2011). The subcellular compartmentation events that gave rise to eukaryotes enabled them to develop greater structural and functional complexity than their ancestors. With endomembrane compartments, cells could grow and take up nutrients through endocytosis, interact with their environments through secretion, and increase energy production by sequestering metabolic processes (Lane and Martin, 2010; Schlacht et al., 2014). But with compartmentation came the requirement for exchange between membrane compartments. For example, with lipid and protein synthesis concentrated in one compartment, the cell needed a way to transport the products to other compartments. Consistent with this requirement, prevailing models for eukaryotic evolution suggest that many components of the membrane trafficking machinery were already present in the last common eukaryotic ancestor (Zaremba-Niedzwiedzka et al., 2017).

Most exchange between compartments of the endomembrane system is accomplished by transport intermediates, although it should be noted that communication between organelles can occur through direct contact. The many roles of membrane contact sites, including lipid and small molecule transfer, are becoming increasingly apparent (Phillips and Voeltz, 2016). Additionally, inter-compartmental tubule formation is a commonly proposed model for exchange (Mironov et al., 1997). At the ER and Golgi, such tubules can help explain reports of rapid cargo transit kinetics (Patterson et al., 2008), but are difficult to detect and do not account for selective transport of cargo. One possibility is that tubules are transient and act in addition to transport intermediates (Glick and Luini, 2011). The most common and

well studied intermediate carriers are coated vesicles. These are small, 60-120 nm membrane structures that bud from donor membranes and fuse with acceptor membranes (Bonifacino and Glick, 2004; Jensen and Schekman, 2011).

The Biosynthetic Pathway

The cell uses vesicular transport along trafficking pathways as a way to move cargo between compartments to its final destination. In the biosynthetic pathway, newly synthesized material travels in vesicles from the ER to the *cis*-Golgi and then from the *trans*-Golgi to secretory carriers or vesicles destined for other cellular compartments. Why might a multi-compartment pathway be more advantageous than a direct route? One answer is that a pathway permits complete, sequential processing of secretory protein cargo. Once in the ER, secretory proteins undergo the first round of processing, which broadly promotes proper protein maturation. ER-targeting signal sequence peptides are cleaved, carbohydrate modifications begin, disulfide bonds form, folding is chaperoned, and misfolded proteins are policed and degraded (Barlowe and Miller, 2013). In Golgi compartments, sequential carbohydrate modifications continue and proteolytic processing occurs (Brigance et al., 2000). Final sorting into secretory carriers occurs at the late Golgi or *trans*-Golgi network (TGN).

At vesicular transport steps at the ER and TGN, biosynthetic cargo is sorted for packaging while compartment residents are generally excluded (Bard and Malhotra, 2006; Chanat and Huttner, 1991; Miller et al., 2003). Vesicular transport within the Golgi functions somewhat differently, where it is likely that cargo is generally excluded and resident proteins are transported in vesicles. This distinction is discussed in the next section. It is important to consider that while cargo moves in the anterograde direction, some material, including escaped residents and components of the transport machinery, must be returned in a retrograde recycling pathway, adding an additional layer to the biosynthetic pathway.

The Machinery of Membrane Transport

Concentration of cargo and targeting of vesicles is carried out by membrane transport machineries, which confer specificity to individual trafficking routes (Cai et al., 2007; Zerial and McBride, 2001). The implication is that for each vesicular transport route, distinct machinery is required to provide specificity of cargo selection at the donor compartment and specificity of targeting to an acceptor compartment. Thus, a cell is limited in the number of distinct inter-compartmental connections it can make by the diversity of its machineries.

One candidate for determining specificity is the coat that surrounds a vesicle. COPI, COPII, and clathrin are the major types of coats, although other complexes, such as exomer in yeast, may function as coats as well, and some types of vesicles do not use coats (Spang, 2008). The coats have distinct assembly processes, but different classes of coated vesicles bear many similarities in their overall organization, with an inner cargo adaptor layer and an outer cage layer (Faini et al., 2013). Coats polymerize in patches on the membrane bilayer's cytosolic face at the site of nascent vesicle formation, eventually encasing the budded carrier in a lattice. This polymerization helps promote membrane curvature as well as concentration of cargo, often with help from adaptor proteins (Faini et al., 2013). COPII coats Golgi-targeted vesicles originating from specific locations on the ER membrane called ER exit sites (ERES). The COPII coat assembles in two layers: the inner, cargo-associated Sec23/24 complex and the outer Sec13/31 complex (Jensen and Schekman, 2011). COPI bundles its adaptor and cage layers in one heptameric protein complex (Yip and Walz, 2011) that operates in intra-Golgi and Golgi-to-ER transport. These two transport steps are accomplished by different sub-types of COPI vesicles known as COPIa and COPIb, respectively, in plants and algae (Donohoe et al., 2007). COPIa vesicles can be found in the space between the ER and *cis*-Golgi, while COPIb vesicles are seen at the rims of medial and *trans*-Golgi cisternae. A similar distinction can be made in mammalian cells, where COPI complexes with different subunit isoforms have different localizations and appear to transport different sets of cargo (Lanoix et al., 2001; Moelleken et al., 2007). Finally, clathrin coats also function in

multiple transport pathways, forming cages on endocytic vesicles at the cytosolic face of the plasma membrane, on TGN-derived vesicles targeted to endosomes, and on TGN- or early endosome-derived retrograde recycling vesicles. Clathrin uses a wide variety of accessory and adaptor proteins to fulfill these many functions (Kirchhausen, 2000).

The coats alone are probably not sufficient to generate the specificity required for even a simple endomembrane network. For instance, clathrin-coated vesicles bud from both the TGN and the plasma membrane with distinct cargo and target compartments (Myers and Payne, 2013). For a single coat, different cargo adaptors can aid in the selection of distinct cargoes. For example, clathrin uses at least two multimeric adaptor complexes, AP-2 at the plasma membrane and AP-1 at the TGN (Myers and Payne, 2013). It is not clear how the use of different adaptors can facilitate unique targeting of clathrin-coated vesicles, however. Specifically, some evidence suggests that vesicle uncoating may not occur until the vesicle reaches its destination, possibly obscuring any signals from the enclosed adaptors (Cai et al., 2007). In this case, some additional factor is likely required to determine the destination of coated vesicles.

SNARE (soluble N-ethylmaleimide-sensitive factor attachment protein receptor) proteins are another type of trafficking machinery proposed to be a determinant of specificity (Furukawa and Mima, 2014). SNAREs are long coiled-coil proteins that drive membrane fusion from opposing membranes by zippering up in helical bundles of 4 SNAREs. Some SNAREs are type II membrane proteins, while others can attach to the membrane by posttranslational lipid anchor modifications (Malsam et al., 2008). The SNARE present on the vesicle is commonly referred to as a v-SNARE, while those on the target membrane are called t-SNAREs. This terminology has limitations because SNAREs do not only function in vesicle fusion, but can mediate fusion of compartments, as is the case with homotypic vacuole fusion (Seals et al., 2000), and following membrane fusion, v-SNAREs are present on the target membrane. A more systematic classification is based on an amino acid sequence feature of SNAREs. The center of the zippering helix, termed the '0' layer, is typically either a glutamine or an

arginine, resulting in four types of SNAREs for each cognate SNARE complex: Qa-, Qb-, Qc-, and R-SNAREs (Fasshauer et al., 1998). Frequently, the t-SNAREs are Q-SNAREs and the v-SNARE is an R-SNARE (Malsam et al., 2008).

Yeast and mammals have at least 7 sets of SNARE complexes (Jahn and Scheller, 2006), which act in distinct endomembrane routes. Different SNARE complexes operate in anterograde ER-to-Golgi transport and retrograde Golgi-to-ER transport, for example. Cognate SNARE complexes are not entirely exclusive, however, and in vitro studies suggest that some SNAREs act in multiple pathways or can fill in for other SNAREs (Tsui and Banfield, 2000). Additionally, SNAREs can only act at a relatively close range, once the vesicle and target membrane are $\sim$25 nm apart (Jahn and Scheller, 2006). Thus, the first line in vesicle recognition, and therefore targeting specificity, is more likely long-distance protein tethers, which can bind vesicles $\sim$50 nm from the target membrane (Jahn and Scheller, 2006). Endomembrane compartment tethers are more diverse than the set of SNAREs, but fall into two main groups: long coiled-coil proteins and multisubunit tethering complexes. Differences in structure and function among tethers has made it challenging to assign domains and binding partners (Yu and Hughson, 2010).

Finally, phosphoinositides and small GTPases function as regulatory components to efficiently coordinate machinery recruitment and activation of vesicle formation and fusion, ensuring that these activities occur at the right time and place. Phosphoinositides include PI(3)P (phosphatidylinositol 3-phosphate) at endosomes and PI(4)P (phosphatidylinositol 4-phosphate) at the TGN. They are regulated by kinases and phosphatases, providing tunable, organelle-specific binding platforms. Recruitment to a membrane domain is sometimes accomplished through coincidence detection of specific compartmental identifiers. For instance, the clathrin adaptor AP-1 is recruited to the TGN by binding both a Golgi GTPase and PI(4)P (Gleeson et al., 2004).

Small GTPases are generally "turned on" through membrane recruitment by a specific GEF (guanine nucleotide exchange factor), resulting in the recruitment and activation of

effector proteins. GTPases permit tight regulation through the use of GAPs (GTPase activating proteins) to "turn off" activity (Hutagalung and Novick, 2011). The GTPases most relevant to endomembrane trafficking are the Arf and Rab families. Rab GTPases have specific localizations to organelles throughout the cell, and their prevalence makes them excellent candidates for determining membrane transport specificity. Yeast possess 11 Rabs, while mammalian cells have over 60 (Hutagalung and Novick, 2011). Arf GTPases are also specifically localized to different subcellular compartments, but the best characterized Arf proteins are present on compartments of the biosynthetic pathway: Sar1 functions in COPII vesicle biogenesis at the ER and Arf1 functions at the Golgi (Gillingham and Munro, 2007). Interestingly, Arf1 initiates formation of both COPI and clathrin coated vesicles at different locations or stages within the Golgi complex (Spang, 2008). Distinct GEFs appear to recruit Arf1 for each of these types of vesicles. Still, how the same GTPase is used to direct recruitment of distinct cargo and machinery remains a fascinating puzzle. Ultimately, it is likely that each component of the membrane transport machinery –coats, adaptors, SNAREs, tethers, and GTPases –works in a coordinated effort to form and target a transport vesicle with the requisite compartmental specificity.

Golgi Organization

After the ER, the next stop on the biosynthetic pathway is the Golgi complex. By electron microscopy, the Golgi is often a striking feature. It consists of multiple membrane-bound cisternae that, in most cell types, appear as stacked, flattened sacs with rounded rims (Mogelsvang et al., 2004). Several Golgi proteins are conserved in nearly all eukaryotes (Dacks and Field, 2007), yet the Golgi can appear vastly different across organisms. The number of cisternae can vary widely, and cisternae are not stacked in some cell types, including the yeast *Saccharomyces cerevisiae*. A few eukaryotes have no discernible Golgi structures (Mowbrey and Dacks, 2009).

The cisternae of the Golgi stack are not homogeneous. Moving across the stack, cisternae differ in composition and function. The side nearest the ER, which receives newly synthesized material, is the *cis* face, while at the opposite side, this biosynthetic material is packaged at the *trans* face to be sent to its final destination (Farquhar and Palade, 1981). It follows that cargo must somehow travel across the stack, but based on morphology, it is not immediately apparent how this occurs. The mechanism for cargo transport through the Golgi has been a subject of debate for decades (Emr et al., 2009), with two main models that have alternatingly held the favor of Golgi researchers over the years: the stable compartments model and the cisternal maturation/progression model. In the stable compartments model, Golgi cisternae are long-lived, static structures that each retain their particular set of resident Golgi enzymes (Dunphy and Rothman, 1985). COPII vesicles fuse with *cis* cisternae to deliver cargo from the ER. This cargo is then incorporated into COPI vesicles and carried forward from cisterna to cisterna, and ultimately packaged into vesicles and secretory carriers that bud from the TGN (Orci et al., 1986). In the cisternal maturation model, cisternae form de novo at the *cis* face by homotypic fusion of COPII vesicles (Barlowe and Miller, 2013). The cisternae progress through the stack like a conveyor belt, from *cis* to *trans*, while COPI vesicles carry resident proteins from cisterna to cisterna in a net retrograde manner (Day et al., 2013; Glick and Malhotra, 1998). In this way, a younger *cis* cisterna matures by acquiring the resident proteins of an older *trans* cisterna. Terminally mature cisternae then disperse through the formation of secretory carriers, clathrin-coated vesicles destined for endosomes, and retrograde carriers to recycle resident proteins to younger Golgi cisternae (Papanikou and Glick, 2014).

Determining the accuracy of either model for Golgi transport has proved challenging. Although the models make very different predictions regarding the contents of COPI vesicles, some studies have found evidence of secretory cargo in COPI vesicles, while others have instead observed resident Golgi proteins in COPI vesicles (Glick and Luini, 2011). Eventually, evidence that cargoes too big to fit in COPI vesicles could traverse the Golgi stack (Bonfanti

et al., 1998) began to tip the scales in favor of the cisternal maturation model. The most convincing evidence for cisternal maturation came from budding yeast, in which nonstacked Golgi cisternae make it possible to visualize spatially distinct early and late Golgi cisternae when labeled with fluorescent tagged resident markers (Losev et al., 2006; Matsuura-Tokita et al., 2006). An early Golgi marker, the GDP-mannose transporter Vrg4, was tagged with GFP. The late Golgi-specific Arf-GEF Sec7 was tagged with a red fluorescent protein, DsRed (Losev et al., 2006). The stable compartments model predicts that green- and red-labeled Golgi cisternae should be long-lived while cargo travels between them in vesicles. In contrast, the cisternal maturation model makes the specific prediction that a green-labeled cisterna should lose the early marker GFP-Vrg4 and acquire the late marker Sec7-DsRed as it matures. Indeed, this prediction was correct: Golgi structures were consistently observed undergoing green-to-red transitions (Losev et al., 2006). While the cisternal maturation model answers questions about how biosynthetic cargo moves through the Golgi, many questions remain, particularly about the cause and function of Golgi stacking, the localization/retention of Golgi resident proteins, and the molecular drivers of maturation (Glick and Nakano, 2009).

During their transit across the Golgi stack, proteins and lipids undergo posttranslational modifications. These modifications chiefly involve the addition or removal of carbohydrate groups by glycosyltransferases and glycosidases. Carbohydrate modifications are sometimes complex and carried out sequentially, with one moiety added at a time, generating the substrate for the next glycosyltransferase (Stanley, 2011). One possible reason for the complicated cisternal structure of the Golgi is to increase the efficiency of this process by arranging posttranslational modifying enzymes across the stack according to their order of action. For instance, the mannose 6-phosphate sorting tag must be added to mammalian lysosomal hydrolases before they encounter the uncovering enzyme that enables receptor recognition, and these steps occur in the early Golgi and late Golgi, respectively (Goldberg and Kornfeld, 1983). Golgi morphology in some cells may also improve efficiency: flattened cisternae could

increase enzyme-substrate access, while cisternal stacking has been proposed to promote complete processing by delaying export from the Golgi (Zhang and Wang, 2016).

The *cis* and *trans* faces of the Golgi differ not only with respect to glycosylation enzyme localization, but also in terms of membrane transport machinery. Different tethers, SNARE complexes, and coats are concentrated at each face of the Golgi. How are resident proteins localized within the Golgi? Given the continuous, dynamic protein transport that occurs in the Golgi, resident proteins not only must be targeted initially to a particular stage of the Golgi, but must then recycle from maturing older to younger cisternae. Three major mechanisms have been demonstrated in the Golgi. For type II membrane proteins, which include glycosyltransferases, the trans-membrane domain (TMD) appears to function as a retention signal (Munro, 1998). Interestingly, the length, rather than the sequence, of the TMD regulates retention. TMD length has been shown to correspond to protein localization throughout the compartments of the secretory pathway, and is likely related to the increase in membrane thickness across the pathway, even between early and late Golgi cisternae. A protein would be retained in the compartment with a membrane thickness that most favorably accommodates its hydrophobic TMD (Sharpe et al., 2010). Under the cisternal maturation model, this difference in membrane thickness requires a change in membrane composition during maturation, which occurs as lipids are remodeled in the Golgi (Bankaitis et al., 2012). As resident proteins progress through the stack, they would segregate into retrograde vesicles to return to a compartment with a favorable membrane thickness. A second localization method, utilized by TGN proteins such as Kex2 and TGN38, employs cytoplasmic tail sequences. In contrast to the TMD mechanism, these sequences are used as retrieval signals when proteins escape to the plasma membrane or endosomes (Munro, 1998). A third type of localization mechanism involves sorting signals that are recognized by the yeast protein Vps74. Vps74 binds a specific sequence in the cytoplasmic tail of some glycosyltransferases, and targets these to COPI vesicles (Tu et al., 2008). This highlights the role COPI may play in generating localized distributions of Golgi resident proteins.

An important, but tricky question is how to classify Golgi subcompartments, or the different functional, structural, and morphological stages of the Golgi. The typical view of the past few decades identifies four stages: *cis*, medial, *trans*, and TGN. These divisions are roughly based on the localization of Golgi resident enzymes. It was apparent early on that in order to maintain directional protein transport across the stack, the *cis* and *trans* faces of the Golgi must facilitate cargo entry and exit, respectively, and therefore must be biochemically distinct (Dunphy and Rothman, 1985). The medial Golgi was established as a third subcompartment to account for the different response to a transport inhibitor observed in the middle set of cisternae (Griffiths et al., 1983). The TGN is the sorting stage of the Golgi, and the most overtly distinct subcompartment. Electron tomography of mammalian Golgi stacks shows that early cisternae are surrounded by COPI vesicles, while the *trans*-most cisterna, the TGN, produces clathrin-coated vesicles (Ladinsky et al., 1999; Mogelsvang et al., 2004). This distinction is reinforced by the response in mammals to Brefeldin A, which causes the early Golgi to collapse into the ER while the TGN segregates with endosomes (Klausner et al., 1992). Lastly, in addition to these four subcompartments, the ER-Golgi intermediate compartment (ERGIC) in mammalian cells is physically distinct from the *cis* Golgi, but nonetheless shares a great deal of the vesicular transport machinery that is found in that stage (Appenzeller-Herzog and Hauri, 2006). While these four compartments are often depicted as discrete units, fractionation and immuno-EM studies to determine the localization of glycosylation enzymes shows that these proteins sometimes have broad, overlapping distributions (Dunphy and Rothman, 1985; Kornfeld and Kornfeld, 1985). It is difficult to clearly demarcate compartments from such studies. While glycosylation enzymes and Golgi morphology vary among cell types, the transport pathways and mechanisms at the Golgi could provide a more conserved, and therefore a more relevant and universal basis for Golgi classification.

I have proposed a three-stage model for Golgi organization (Day et al., 2013). The stages are defined by their incoming and outgoing trafficking routes, and correspond to three major

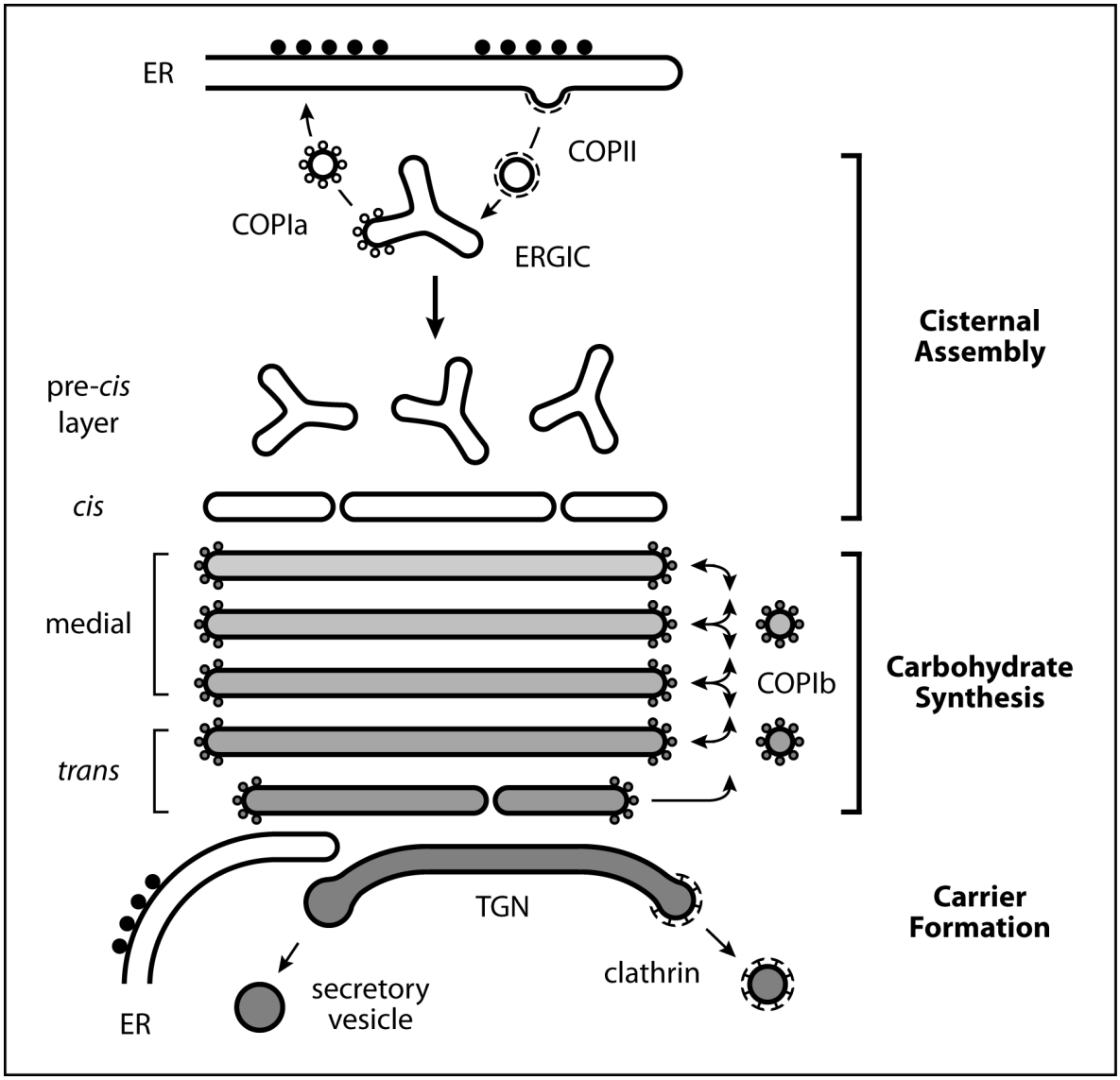

Figure 1.1: A model for Golgi compartment organization. The Golgi can be divided into three stages of maturation. During the cisternal assembly stage, COPII vesicles bud from the ER and fuse with one another to generate a new Golgi cisterna, while COPIa vesicles bud from this nascent cisterna to recycle trafficking proteins and resident ER proteins to the ER. This stage includes *cis*- Golgi cisternae, as well as ERGIC membranes in animal cells. During the carbohydrate synthesis stage, most of the oligosaccharide remodeling reactions take place, and resident Golgi proteins are transferred between cisternae by COPIb vesicles. This stage includes cisternae that are often designated medial and *trans*. During the carrier formation stage, the cisterna disintegrates to produce cargo carriers that include clathrin-coated and secretory vesicles. This stage includes cisternae that are traditionally designated TGN. (From Day et al., 2013 and Papanikou and Glick, 2014.)

functions of the Golgi (Figure 1.1). The first stage, called the "cisternal assembly" stage, forms by fusion of COPII vesicles and then grows through homotypic fusion and the addition of more COPII vesicles (Donohoe et al., 2013). The cisternal assembly stage conducts a low level of glycosylation. In situ localization of glycosylation enzymes rarely produces signal in the earliest cisternae, and the lumen of the *cis*-most cisternae in electron micrographs of plant and algal cells appears less densely stained, suggesting a lack of nucleotide sugars at this early stage (Donohoe et al., 2013; Velasco et al., 1993). The transition to the next stage would begin with the fusion of retrograde vesicles containing Golgi enzymes, including nucleotide sugar transporters. The cisternal assembly stage is therefore defined molecularly by the machinery that enables fusion of COPII vesicles from the ER and generates COPIa vesicles destined for the ER.

The second Golgi stage is the "carbohydrate synthesis" stage, where most glycosylation of protein and lipid cargoes occurs. It is worth noting, however, that some glycosylation occurs in the earliest and latest stages (Rabouille et al., 1995). This stage corresponds most closely to the medial and *trans* cisternae. In terms of membrane transport, this stage begins as cisternae gain the ability to form COPIb vesicles and lose the ability to receive COPII vesicles. Diagrams depicting the cisternal maturation model typically show COPIb vesicles at this stage traveling in a retrograde direction, carrying resident Golgi enzymes from one cisterna to the next younger cisterna (Glick et al., 1997). However, it is difficult to envision how this is accomplished mechanistically. The number of cisternae at this stage can vary significantly among species (Becker and Melkonian, 1996). In many cell types, there is not a sufficient variety of Golgi trafficking components to permit specific targeting to each cisterna in the carbohydrate synthesis stage. An alternative possibility is that COPI vesicles can "percolate" within the Golgi stack, fusing with cisternae at random (Orci et al., 2000). Polarized distributions of Golgi enzymes could be generated based on an enzyme's preference for certain properties of cisternae, such as lipid composition. As described earlier, glycosyltransferases may preferentially associate with cisternae with a membrane thickness

complementary to the length of their TMD. According to this hypothesis, an enzyme could travel in vesicles until it finds a cisterna with a suitable lipid composition, where it becomes less likely to partition into COPIb carriers (Day et al., 2013).

Finally, the "carrier formation" stage, which corresponds to the TGN, facilitates sorting and exit of cargo proteins. Clathrin-coated vesicles arise from this stage (Ladinsky et al., 1999), so part of the defining machinery of this compartment is its set of clathrin adaptors and effectors. The carrier formation stage exchanges material with endosomes and thus also functions in the sorting and transfer of proteins in the endocytic pathway, and is described in detail in the next section.

The three-stage model is a useful framework for studying the Golgi. Defining stages by membrane trafficking pathways points to trafficking machinery as a likely driver of Golgi cisternal maturation and provides a meaningful way of testing mechanisms behind Golgi maturation. For example, effectors of Golgi GTPases include coats, adaptors, and tethers. Trafficking pathways at each stage of the Golgi could be coordinated by GTPases, while a Rab GTPase cascade could cause the switch to the next stage (Papanikou and Glick, 2014). Nevertheless, like any attempt to describe dynamic biological phenomena with a concise, static diagram, this model has its shortcomings. Although there is a risk of creating a classification scheme that is too finely divided to be broadly applicable, a three-stage model may be too simple to describe the stepwise changes of Golgi transport pathways. An additional layer of classification helps to define the transitions between Golgi stages (Kim et al., 2016). For instance, at the interface between the carbohydrate synthesis and carrier formation stages, a maturing cisterna (a) acquires the machinery needed to receive retrograde clathrin-coated carriers from the oldest, *trans*-most cisternae and endosome-derived carriers and (b) gains the ability to form clathrin-coated vesicles and secretory carriers. Logically, these steps occur sequentially, rather than simultaneously. So a transitional stage could be defined by the ability to receive, but not form, clathrin-coated vesicles. In terms of machinery, this transitional stage could possess tethering machinery for clathrin-coated vesicles, but still

lack clathrin adaptors. More work will be necessary to test this hypothetical organization and determine the composition of transitional stages and what drives their timing.

Exiting the TGN

The TGN receives, sorts, and exports cargo destined for a variety of locations both within and outside of the cell. One input at the TGN is the maturing Golgi itself, which brings newly synthesized endomembrane and cell surface residents as well as secretory cargo. This material converges with another input: vesicles from multiple endosomal compartments, which recycle machinery back to the TGN and transport endocytic cargo originating from the plasma membrane (De Matteis and Luini, 2008). The outgoing routes of the TGN are even more complex. Depending on the cell type, the TGN may need to coordinate export to recycling endosomes, late endosomes, lysosomes/vacuoles, storage granules, and the cell membrane, or to specific membrane domains in polarized cells (Gleeson et al., 2004). Moreover, the TGN conducts some final biosynthetic processing of proteins and lipids (De Matteis and Luini, 2008). The enzymes that carry out this processing likely follow yet another outgoing route from terminally mature to younger TGN structures.

The TGN must coordinate protein cargoes, lipids, and machinery, into distinct transport vesicles. To accomplish this feat, the TGN, like other compartments of the endomembrane system, appears to be organized into exit subdomains that can generate one type of carrier (Pfeffer, 2003), which could be distinct from import subdomains. Visual evidence for TGN domains came from electron tomography studies in mammalian cells, which identified tubules at the TGN with distinct coated or uncoated vesicle budding profiles (Ladinsky et al., 1994; Ladinsky et al., 2002). The TGN has a heterogeneous morphology with tubular, reticulated, and vesicular regions (Clermont et al., 1995). The *trans*-most cisterna often appears to be peeling off from the Golgi stack (Ladinsky et al., 1994), which further contributes to the distinct shape and high curvature of TGN structures.

How do domains form at the TGN? Rab and Arf GTPases are the most likely candidates to coordinate sorting adaptors and transport machinery. GTPases could work in concert with lipids to generate defined domains that recruit trafficking components through coincidence detection (Pfeffer, 2003). The action of GAPs, GEFs, and feedback networks regulates GTPases that act in parallel transport processes (McDonold and Fromme, 2014). These networks could generate boundaries between TGN domains, if for example, an effector of one GTPase is a locally recruited GAP that inactivates the GTPase of a nearby domain.

It has become evident, however, that sorting of biosynthetic cargo can take time, and must begin before transport carriers form. The Golgi uses several mechanisms to sort cargo. One general sorting principle is based on TGN morphology. For example, it has been proposed that lipids and proteins in Golgi membranes could passively segregate to either flatter regions, tubules, or the rounded rims of cisternae based on their preference for membrane curvature (De Matteis and Luini, 2008). Another sorting mechanism involves post-translational modifications. Proteins with ubiquitin tags are recognized at the TGN by Gga adaptors and subsequently packaged into clathrin-coated vesicles targeted for endosomes (Costaguta et al., 2001; Scott et al., 2004). The mannose-6-phosphate receptor (M6PR) resides in the TGN and recognizes lysosomal hydrolases based on their mannose-6-phosphate glycosylation signatures. Glycosylation has also been shown to communicate sorting signals for secretory cargo (Yeaman et al., 1997). A third type of sorting mechanism involves oligomerization or clustering of proteins. For example, the TGN uses lectin-mediated crosslinking to cluster glycoproteins, resulting in their selective apical secretion (Delacour et al., 2007).

Sorting at the TGN also uses more specific mechanisms, with sequence-defined domains that coordinate cargo binding to adaptors and other machinery (Bonifacino and Traub, 2003). The cytosolic tail of the M6PR contains consensus sequences recognized by clathrin adaptors for transport to endosomes (Guo et al., 2014). AP-1 can also recognize tyrosine- and acidic dileucine-based motifs in mammalian secretory protein cargoes (Bonifacino, 2014). An interesting implication is that secretion may not be the "default" TGN exit route, as is often

assumed. It is possible that sorting signals enable either efficient packaging into secretory carriers, or perhaps more rapid exit than by bulk flow (Thor et al., 2009; von Blume et al., 2012). Specific sorting signals can be difficult to identify, however, and would ultimately need to account for a broad range of biosynthetic cargo.

One particular complication in understanding TGN sorting is the apparent functional overlap between the clathrin adaptors AP-1 and Gga. The roles of these adaptors, and even the directionality of the pathways they are involved in, have been difficult to parse. The heterotetrameric AP-1 adaptor complex was widely thought to function in trafficking from the TGN to endosomes, though a role in the retrograde trafficking route from endosomal compartments to the TGN was later invoked (Hinners and Tooze, 2003). In yeast, deletion of subunits from this highly conserved complex had no effects on trafficking (Myers and Payne, 2013). When the monomeric Gga adaptors were found to be important for TGN-to-endosome transport, possibly using the same dileucine sorting motif, the function of AP-1 became shrouded in even more confusion (Hinners and Tooze, 2003; Puertollano et al., 2001). Although it has been suggested that these adaptors function cooperatively in a single sorting mechanism (Doray et al., 2002), their roles appear to be partially redundant (Hirst et al., 2012). Recently, it was shown in yeast that these clathrin adaptors are sequentially recruited to the TGN, with AP-1 arriving after the Gga proteins, possibly resulting in different cargo specificity based on the timing of clathrin-coated vesicle formation (Daboussi et al., 2012).

The Endocytic Pathway

While the biosynthetic pathway is largely tasked with moving material to the cell surface, the endocytic pathway moves material from the cell surface to intracellular destinations. From the plasma membrane, the endocytic pathway proceeds to endosomal compartments. From endosomes, material can be recycled back to the surface, as is the case for some membrane receptors, or sent to the lysosome/vacuole for degradation, which, for example, is a way to attenuate signaling from ligand-bound receptors (Figure 1.2.

Multiple types of endocytosis exist, but clathrin-mediated endocytosis is responsible for most plasma membrane protein and lipid internalization (Engqvist-Goldstein and Drubin, 2003). Sites of endocytosis must recruit several factors: actin organizers, membrane remodelers, clathrin and cargo adaptors, and cargo modifying enzymes (Engqvist-Goldstein and Drubin, 2003). At the plasma membrane, endocytic cargo proteins are bound at their cytosolic tails and concentrated in endocytic patches by adaptors. AP-2 is a heterotetrameric adaptor in the same family as AP-1 that recognizes similar consensus sequences (Kelly and Owen, 2011). One signal for endocytosis is ubiquitin. In yeast, a ubiquitin tag is added to receptor tails upon binding by arrestin-related trafficking adaptors (ARTs), which recruit a ubiquitin ligase, often Rsp5 (Lin et al., 2008). Ubiquitin is recognized by several components of the early endocytic patch machinery. In mammalian cells, β-arrestins recognize ligand-bound receptors and target them for endocytosis (Conibear, 2010). Clathrin is recruited to the nascent patch, which protrudes inward and matures as actin and clathrin adaptor proteins are recruited. Eventually, proteins arrive to promote actin polymerization, branched actin networks, and association with myosin motors and actin cables. Dynamic cortical actin patches mark the late stages of endocytic vesicle formation (Goode et al., 2015). Following inward deformation of the membrane, scission occurs. The final events are disassembly of endocytic patch components, the vesicle's actin network, and the vesicle coat (Toret and Drubin, 2006).

Endocytic vesicles travel on actin cables to their first destination in the cell, which is an early endosome, sometimes also called a sorting endosome (Maxfield and McGraw, 2004). Here, vesicles fuse with each other and with the early endosome. The vesicles deliver cargo to be sorted into multiple pathways: either back to the cell surface, or to other endosomes, or to the TGN, either indirectly through a recycling endosome, or possibly directly (Lieu and Gleeson, 2010). The early endosome is best characterized in mammalian cells. Morphologically, this compartment often has a tubular domain and a rounded, vesicular domain. Low pH at the early endosome results in ligand release from receptors (Maxfield and Mc-

Graw, 2004). Receptors destined for recycling to the cell surface for additional rounds of internalization tend to partition into the tubular domain. The tubules can undergo scission, ultimately fusing with the plasma membrane for fast recycling or with a highly tubulated recycling endosome for slightly slower recycling (Goldenring, 2015; Hao and Maxfield, 2000). The recycling endosome can then sort and transfer material either to the TGN or to the plasma membrane. The bulk portion of the early endosome goes on to mature into a late endosome (Huotari and Helenius, 2011), which targets endocytic material for degradation by fusing with the lysosome.

The recycling and late endosomes of mammalian cells exchange material with the TGN in both directions. Recycling endosomes often serve as post-TGN sorting sites for secretory cargo that is targeted specifically to the apical or basolateral cell surface (Ang et al., 2004; Lock and Stow, 2005; Thuenauer et al., 2014). Late endosomes receive newly synthesized lysosomal hydrolases from the TGN and must recycle their receptors back to the TGN with help from machinery known as the retromer complex (Seaman, 2012). The many membrane transport routes that connect mammalian endosomal compartments, which themselves are not stable but undergo dynamic turnover, means that their protein and lipid composition is not constant. Thus, endosome identity can be difficult to define (Maxfield and McGraw, 2004). As with the Golgi, endosomal compartments can be organized in space and time at a fundamental level based on trafficking pathways. For example, the early endosome receives material from the cell surface, so it almost certainly possesses a set of SNAREs, and fusion appears to be regulated by a GTPase, Rab5 (Woodman, 2000). Furthermore, like the TGN, the mammalian early endosome is thought to segregate into Rab-defined domains (Sönnichsen et al., 2000), which mark membranes targeted to different transport routes. Finally, the early endosome, like the Golgi, undergoes maturation. Consistent with a maturation model, the early endosome residents Rab5 and its effectors are displaced and the late endosome resident Rab, Rab7, replaces them (Rink et al., 2005).

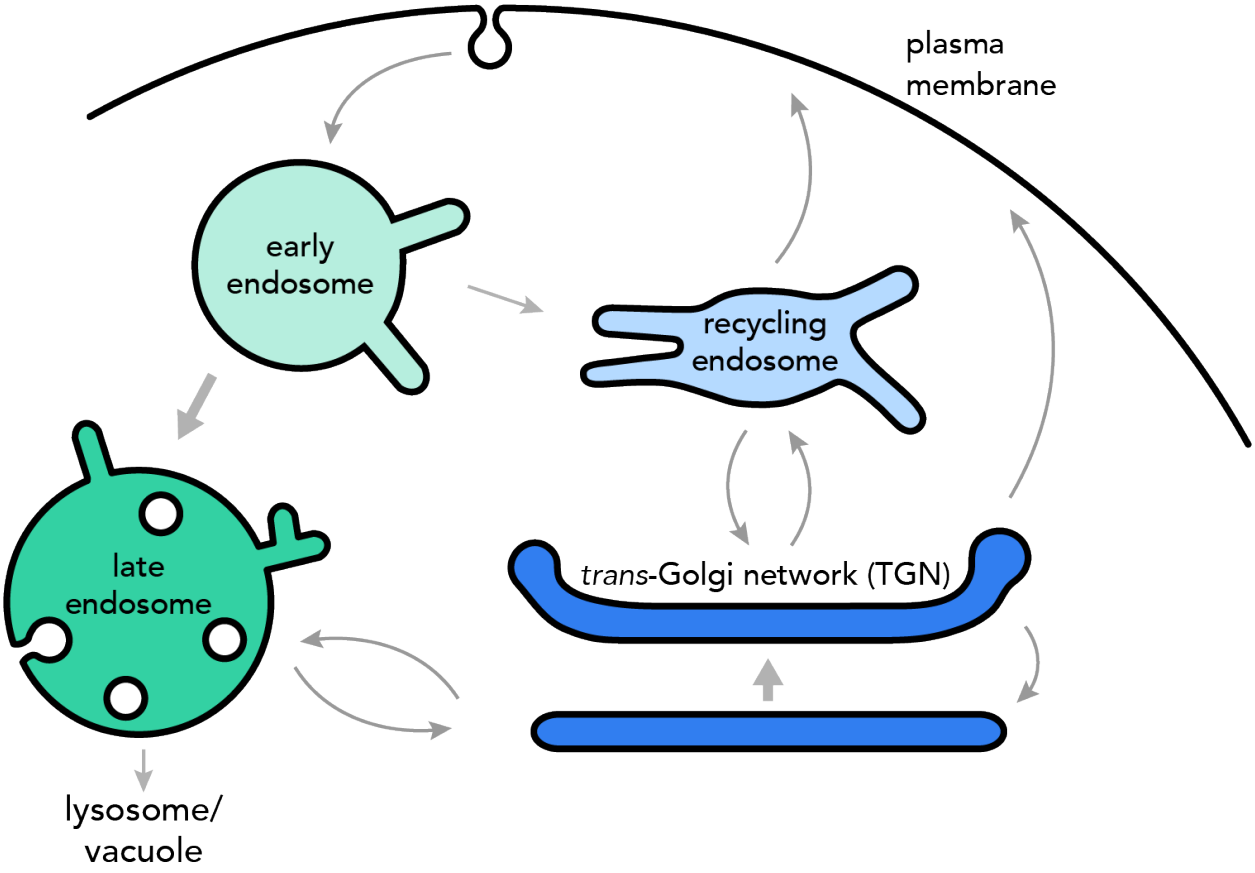

Figure 1.2: The mammalian endocytic pathway. The endocytic pathway involves transfer of material from the plasma membrane to internal organelles that sort this material, called endosomes. This material is generally either recycled back to the cell surface or sent for degradation. In mammalian cells, the recycling route passes from the first destination, the early endosome, through a recycling endosome, to the plasma membrane. The degradative route proceeds as early endosomes mature into late endosomes, which ultimately deliver their material to be degraded in lysosomes. Transport routes between the TGN and endosomes allow exchange with the biosynthetic pathway.

Perspective

The membrane trafficking field has made significant progress in identifying the machinery that drives membrane transport pathways between subcellular compartments. However, if one thinks of the endomembrane system as a wiring diagram of the cell, major gaps in the network still remain. The compartments of the biosynthetic and endocytic pathways lack comprehensive molecular definitions. Such definitions are particularly crucial for maturing compartments such as the Golgi and endosomes, where it can be difficult to determine whether a given pathway originates from an early or late version of the compartment. As described above, compartments can be defined by their incoming and outgoing trafficking pathways. This scheme is useful for reconciling static ideas of compartments with the dynamics of membrane traffic. Ultimately, a wiring diagram of the endomembrane system will require knowledge of the full set of compartments and transport routes, as well as the machinery that drives maturation or membrane exchange.

I addressed these issues using the budding yeast *S. cerevisiae*. Through an analysis of Golgi dynamics, I helped to identify a role for the COPI coat in driving the molecular transitions that underlie maturation at this compartment. I also examined the dynamics and molecular components of endosomal compartments in yeast, as well as the routes that endocytic cargoes travel between these compartments. This work resulted in a model for a simplified endomembrane system that provides a useful framework for studying trafficking pathways. Finally, through these studies, I developed improved imaging and processing techniques for visualizing yeast compartmental dynamics.

CHAPTER 2

COPI SELECTIVELY DRIVES MATURATION OF THE EARLY GOLGI

Abstract

COPI coated vesicles carry material between Golgi compartments, but the role of COPI in the secretory pathway has been ambiguous. Previous studies of thermosensitive yeast COPI mutants yielded the surprising conclusion that COPI was dispensable both for the secretion of certain proteins and for Golgi cisternal maturation. To revisit these issues, we optimized the anchor-away method, which allows peripheral membrane proteins such as COPI to be sequestered rapidly by adding rapamycin. Video fluorescence microscopy revealed that COPI inactivation causes an early Golgi protein to remain in place while late Golgi proteins undergo cycles of arrival and departure. These dynamics generate partially functional hybrid Golgi structures that contain both early and late Golgi proteins, explaining how secretion can persist when COPI has been inactivated. Our findings suggest that cisternal maturation involves a COPI-dependent pathway that recycles early Golgi proteins, followed by multiple COPI-independent pathways that recycle late Golgi proteins.

Introduction

The COPI coat was first visualized nearly 30 years ago on vesicles budding from Golgi cisternae (Orci et al., 1986). This coat was shown to consist of a soluble heptameric complex that is recruited to Golgi membranes by the small GTPase Arf1 (Serafini et al., 1991; Waters et al., 1991; Yu et al., 2012). During vesicle formation, COPI polymerizes to form a curved

This chapter is a version of a manuscript published in eLife 2015; 4, e13232 with the same title and the following author list: Effrosyni Papanikou*, Kasey J. Day*, Jotham Austin II, Benjamin S. Glick (*Contributed equally). I contributed to anchor-away validation and movie acquisition and analysis, and performed late Golgi marker recycling data acquisition and analysis; E.P. contributed to anchor-away experiments, movie analysis, EM data acquisition and analysis; J.A. II contributed to EM data acquisition and analysis; B.S.G. contributed to movie analysis.

lattice that captures specific cargoes, including p24 family proteins and certain SNAREs (Beck et al., 2009). COPI can be divided into the B subcomplex, which consists of α-, β'- and ϵ-COP, and the F subcomplex, which consists of β-, δ-, γ-, and ζ-COP (Lowe and Kreis, 1995; Gaynor et al., 1998; Lee and Goldberg, 2010; Jackson, 2014). In mammalian and plant cells, COPI vesicles bud from cisternae throughout the Golgi stack except for cisternae of the *trans*-Golgi network (TGN), which produces clathrin-coated vesicles (Ladinsky et al., 1999; Staehelin and Kang, 2008; Klumperman, 2011). Yet despite this wealth of biochemical, morphological, and structural information, the functions of COPI have been hard to elucidate.

The strongest data implicate COPI in retrograde transport to the ER. Transmembrane ER resident proteins occasionally escape from the ER, and are then retrieved from the Golgi or ER-Golgi intermediate compartment (ERGIC) in retrograde COPI vesicles (Szul and Sztul, 2011; Barlowe and Miller, 2013). Some transmembrane ER proteins contain cytosolically-oriented C-terminal KKxx-type signals, which are recognized by COPI for retrieval to the ER (Cosson and Letourneur, 1997). COPI also retrieves transmembrane ER proteins that associate with the Rer1 recycling factor, as well as transmembrane ER proteins that contain arginine-based sorting signals (Sato et al., 2001; Michelsen et al., 2007). Finally, COPI plays a role in retrieving the KDEL receptor (Orci et al., 1997), which binds escaped luminal ER proteins. Retrograde COPI vesicles are captured at the ER by the Dsl1 tethering complex in a process that involves recognition of the coat (Ren et al., 2009; Zink et al., 2009).

COPI also plays a role in intra-Golgi traffic, but the evidence is open to multiple interpretations. Initially the proposal was that COPI vesicles carry secretory cargoes forward from one Golgi cisterna to the next in a "vesicle shuttle" (Malhotra et al., 1989; Orci et al., 1989). After the discovery of COPI-mediated Golgi-to-ER recycling, the vesicle shuttle model was extended by proposing that COPI vesicles act as bidirectional carriers in the ER-Golgi system (Pelham, 1994; Rothman, 1996). However, the idea that COPI vesicles carry secretory cargoes from one cisterna to the next faced the problem that some secretory cargoes are

much larger than COPI vesicles. Examples include the cell-surface scales that are secreted by certain algae, and procollagen bundles in mammalian fibroblasts (Leblond, 1989; Becker et al., 1995).

This problem was addressed by the cisternal maturation model, which states that cisternae form at the *cis* face of the Golgi, then move through the stack to the *trans* face, then finally peel off to become secretory vesicles (Glick et al., 1997; Mironov et al., 1997; Bonfanti et al., 1998; Glick and Malhotra, 1998; Pelham, 1998). Thus, entire cisternae could act as forward carriers for secretory cargoes. COPI vesicles have been proposed to recycle resident Golgi proteins within the organelle (Rabouille and Klumperman, 2005). Consistent with this idea, resident Golgi proteins have been detected in mammalian COPI vesicles (Martnez-Menrguez et al., 2001; Malsam et al., 2005; Gilchrist et al., 2006; Pellett et al., 2013; Eckert et al., 2014)-although conflicting results have been reported in other studies (Orci et al., 2000a; Cosson et al., 2002; Kweon et al., 2004)-and the localization of some yeast and plant Golgi proteins has been shown to involve COPI (Todorow et al., 2000; Tu et al., 2008; Woo et al., 2015). Early versions of the cisternal maturation model postulated that COPI vesicles move in a directed fashion from older to younger cisternae (Glick et al., 1997; Glick and Malhotra, 1998). However, no mechanism for such directed movement has yet emerged, suggesting instead that COPI vesicles "percolate" bidirectionally between different cisternae (Orci et al., 2000b; Day et al., 2013). Regardless of the specific traffic pattern of COPI vesicles within the Golgi, the result is thought to be a net retrograde movement of resident Golgi proteins as the cisternae mature (Glick and Malhotra, 1998; Day et al., 2013).

The cisternal maturation model does not rule out additional roles for COPI in the traffic of secretory cargoes. For example, some secretory cargoes could move forward through the Golgi on a "fast track" involving anterograde COPI vesicles (Pelham and Rothman, 2000). This concept is supported by evidence that both resident Golgi proteins and secretory cargoes can be incorporated into COPI vesicles (Orci et al., 1997; Malsam et al., 2005; Pellett et al., 2013). Furthermore, COPI-dependent tubules that connect heterologous cisternae have been

implicated in anterograde traffic through the mammalian Golgi (Yang et al., 2011; Park et al., 2015).

A prediction of current models is that COPI should be required for secretion. According to the vesicle shuttle model, COPI carries secretory cargoes through the Golgi. According to the cisternal maturation model, COPI drives the maturation process, thereby continually regenerating the Golgi cisternae that serve as anterograde carriers for secretory cargoes.

A second prediction is that COPI should be required for Golgi maturation. Presumably, as a Golgi cisterna matures into a *trans*-Golgi network (TGN) compartment, COPI vesicles bud to remove resident Golgi proteins, thereby helping to drive the Golgi-to-TGN biochemical conversion (Papanikou and Glick, 2014).

Both of these predictions about the role of COPI have been tested using the yeast *Saccharomyces cerevisiae*. Golgi stacking was lost during the evolution of *S. cerevisiae* (Mowbrey and Dacks, 2009), but this yeast retains a compartmentalized Golgi that functionally resembles the stacked organelle seen in other organisms, with a late Golgi compartment that corresponds to the mammalian TGN (Papanikou and Glick, 2009; Myers and Payne, 2013). Surprisingly, when COPI function was disrupted in *S. cerevisiae* using thermosensitive mutant COPI subunits, secretion was reportedly inhibited for some proteins but not others (Gaynor and Emr, 1997). Equally surprising results were obtained when a strain with a thermosensitive mutant COPI subunit was examined by video fluorescence microscopy. Golgi maturation can be readily observed in wild-type *S. cerevisiae* cells (Losev et al., 2006; Matsuura-Tokita et al., 2006), and when the COPI mutant strain was imaged at the nonpermissive temperature, maturation was slowed but not blocked (Matsuura-Tokita et al., 2006). The mildness of these phenotypes has added to the uncertainty about how COPI acts in the secretory pathway.

Here, we have reexamined the functions of yeast COPI using a new approach. Yeast COPI was rapidly inactivated using the anchor-away method (Haruki et al., 2008; Bharucha et al., 2013), in which FK506-rapamycin binding protein (FKBP) was fused to an "anchor" protein

while FKBP-rapamycin binding domain (FRB) was fused to a COPI subunit. Addition of rapamycin caused the FRB-tagged protein to be tethered at the anchor site, thereby preventing COPI from carrying out its cellular activities.

Fluorescence microscopy revealed that COPI inactivation generated hybrid Golgi structures that contained both early and late Golgi proteins. These structures showed unusual dynamics, with an early Golgi protein often persisting for many minutes while late Golgi proteins underwent relatively normal cycles of arrival and departure. The implication is that COPI selectively drives recycling of early but not of late Golgi proteins. After COPI inactivation, the Golgi remained partially functional, indicating that recycling of early Golgi proteins is dispensable for secretion. This analysis helps to integrate the yeast data into a broader understanding of COPI function.

Results

The two subcomplexes of yeast COPI localize to the early Golgi

COPI has been assumed to operate in vivo as a stable heptameric complex (Hara-Kuge et al., 1994; Sahlmüller et al., 2011; Yip and Walz, 2011). Although COPI can be experimentally separated into the coat-like B subcomplex and the adaptor-like F subcomplex (Beck et al., 2009; Jackson, 2014), recent structural data indicate that the two subcomplexes assemble together to generate the coat (Dodonova et al., 2015). However, an earlier genetic study hinted that different yeast COPI subunits might act in distinct cellular pathways (Gabriely et al., 2007). To examine the in vivo distribution of COPI, we used fluorescence microscopy to visualize several COPI subunits in *S. cerevisiae* (Gaynor et al., 1998). The tagged subunits were Sec26 (β-COP), which is part of the F subcomplex, together with either the Sec21 (γ-COP) subunit of the F subcomplex or the Ret1 (α-COP) subunit of the B subcomplex. Gene replacement was used to tag Sec26 with GFP, and then to tag Sec21 or Ret1 with mCherry. In both cases the colocalization at punctate structures was essentially complete

(Figure 2.1A). This result suggests that the two subcomplexes of COPI are associated in vivo, at least when COPI is bound to membranes.

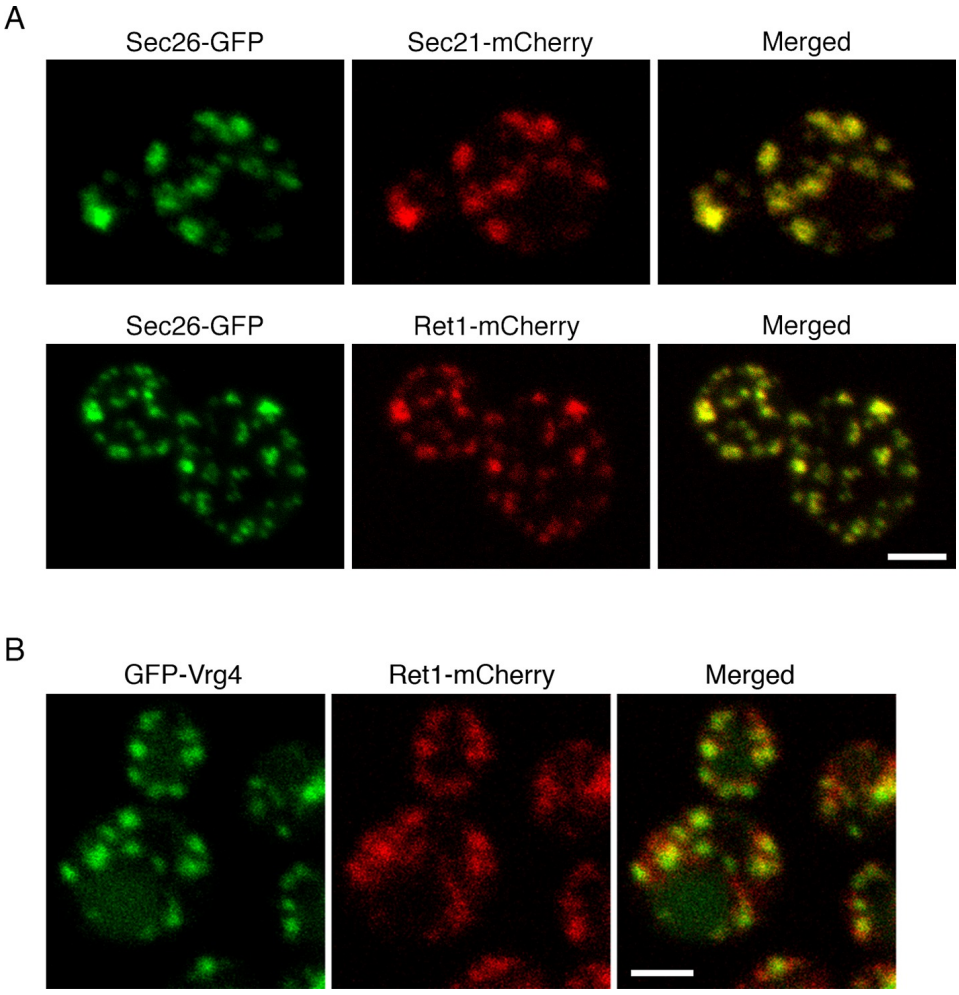

Figure 2.1: Localization of COPI subunits in yeast. (A) COPI subunits were tagged by gene replacement to generate Sec26-GFP, Sec21-mCherry, or Ret1-mCherry. Cells grown in NSD medium at 23°C were imaged by confocal microscopy, and two-color Z-stacks were average projected. Projections from the red and green channels were overlaid to generate merged images. Representative cells are shown. Scale bar, 2 μm. (B) Ret1-mCherry was expressed together with the early Golgi marker GFP-Vrg4. Imaging conditions were as in (A). Scale bar, 2 μm.

The COPI fluorescence pattern was somewhat variable depending on the cell being examined and the imaging conditions. Virtually all of the cells showed large COPI puncta, but a subset of the cells also showed small COPI puncta that may represent intermediates in Golgi assembly (Figure 2.1A) (Arai et al., 2008). COPI colocalized strongly with GFP-Vrg4,

which is a GDP-mannose transporter that marks the early Golgi (Figure 2.1B) (Dean et al., 1997; Abe et al., 2004; Losev et al., 2006). These observations fit with electron tomography studies of mammalian and plant cells, where COPI buds were detected on Golgi but not TGN cisternae (Ladinsky et al., 1999; Mogelsvang et al., 2004; Staehelin and Kang, 2008). Thus, yeast COPI is likely to act at the early Golgi.

Wild-type FRB is suitable for tagging COPI

To test the role of COPI in yeast, we turned to the anchor-away method (Haruki et al., 2008). The parental *S. cerevisiae* strain carried two mutations. First, the cells were rendered resistant to the growth-inhibiting effects of rapamycin by introducing the dominant TOR1-1 point mutation (Helliwell et al., 1994). Second, the FPR1 gene, which encodes the yeast homolog of FKBP, was deleted to ensure that FRB-tagged proteins would be trapped at the anchor site rather than binding to cytosolic Fpr1 (Lorenz and Heitman, 1995; Haruki et al., 2008). The TOR1-1 *fpr1*Δ strain grew nearly as fast as the parental strain and was fully resistant to rapamycin.

This rapamycin-resistant strain was engineered to express the originally described ribosomal Rpl13A-FKBPx2 anchor (Haruki et al., 2008), and to tag yeast COPI with FRB. Some commonly used FRB variants have the T2098L mutation, which allows binding of rapamycin derivatives (Bayle et al., 2006). The T2098L mutation has also been reported to strengthen the affinity of FRB for FKBP-rapamycin (Grünberg et al., 2010). Therefore, gene replacement was used to tag Sec21, which is essential for viability (Hosobuchi et al., 1992), with either wild-type FRB or FRB(T2098L).

The Sec21-FRB strain grew as well as the strain carrying untagged Sec21, but the Sec21-FRB(T2098L) strain showed a pronounced growth defect (Figure 2.2A). T2098L is known to be a destabilizing mutation (Stankunas et al., 2007), so we suspect that FRB(T2098L) caused degradation of tagged Sec21. Interestingly, the growth defect could be rescued by appending maltose-binding protein (MPB) (Figure 2.2A) or GFP (data not shown) to the C-terminus of

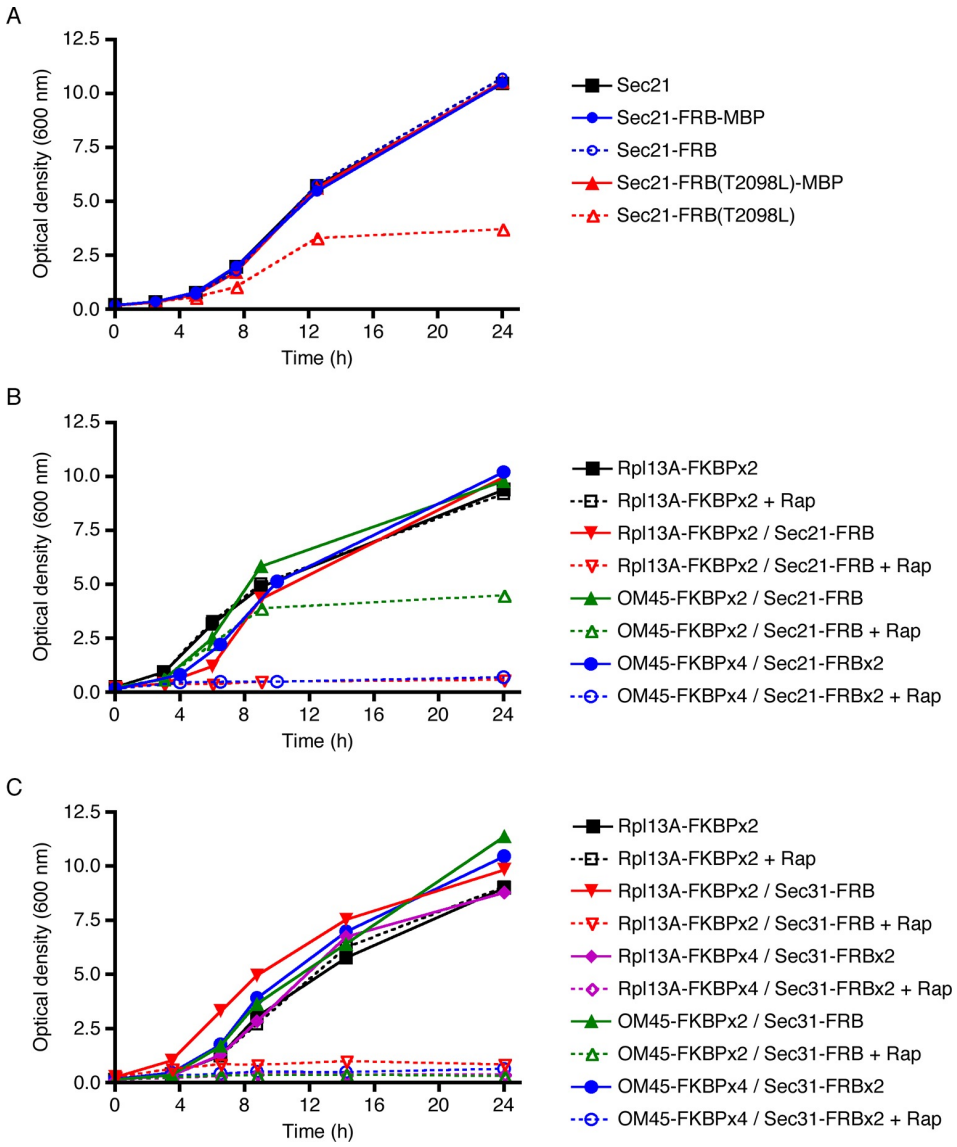

Figure 2.2: Evaluation of tag-anchor combinations by growth curve analysis. TOR1-1 *fpr1*Δ strains were grown with shaking in YPD medium at 30°C to mid-log phase, then diluted in fresh medium to an optical density at 600 nm (OD_{600}) of 0.15. Where indicated, rapamycin ("Rap") was then added to 1 μg/mL. After further incubation at 30°C, aliquots were taken at the indicated time points to measure the OD_{600}. (A) The function of Sec21 is preserved after tagging with wild-type FRB but is compromised after tagging with mutant FRB(T2098L). Gene replacement was used to extend Sec21 at the C-terminus with either wild-type FRB, or FRB(T2098L), or an FRB-MBP dual tag, or an FRB(T2098L)-MBP dual tag. A control strain expressed wild-type Sec21. (B) COPI can be inactivated by extending Sec21 with a single FRB tag followed by anchoring to ribosomes using the Rpl13A-FKBPx2 anchor, or by extending Sec21 with a double FRB tag followed by anchoring to mitochondria using the OM45-FKBPx4 anchor. (C) COPII can be inactivated by extending Sec31 with a single or double FRB tag followed by anchoring to either ribosomes or mitochondria.

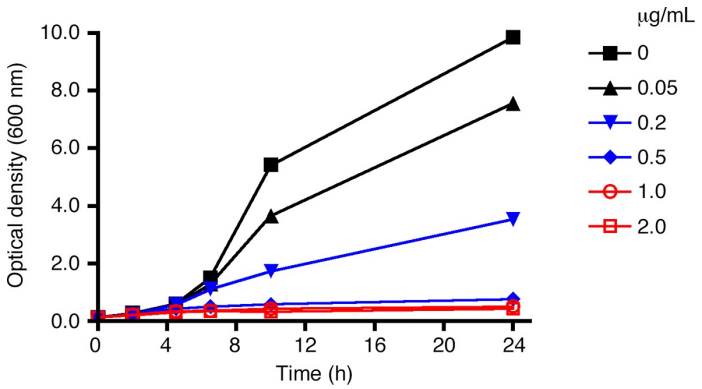

Figure 2.3: Effect of rapamycin concentration on anchor-mediated growth inhibition. As in Figure 2.2, liquid cultures from a strain expressing Sec21-FRB and the Rpl13A-FKBPx2 anchor were treated with rapamycin, and growth was tracked by measuring the optical density at 600 nm for up to 24 hr. Rapamycin concentrations are indicated in μg/mL.

FRB(T2098L). After appending MBP or GFP, the destabilized FRB(T2098L) domain was no longer at an end of the polypeptide chain, and this change may have slowed degradation (Prakash et al., 2004; Fishbain et al., 2011). Regardless of the specific mechanisms at work, these results indicate that FRB(T2098L) is unsuitable as a tag for the anchor-away method, and that wild-type FRB should be used instead.

Either ribosomes or mitochondria can serve as anchor sites

The next step was to test whether growth was inhibited when Sec21 was anchored away. Rpl13A-FKBPx2 served as an anchor on ribosomes. When this anchor was present in a rapamycin-resistant strain encoding wild-type Sec21, rapamycin addition had no effect on growth, as expected (Figure 2.2B). By contrast, when Sec21 was tagged with FRB, rapamycin completely blocked growth (Figure 2.2B). This experiment employed rapamycin at 1 μg/mL, a concentration that was sufficient for maximal growth inhibition (Figure 2.3). A similar analysis was performed using the mitochondrial outer membrane protein OM45 (Yaffe et al., 1989) as an anchor. As previously observed (Cerveny et al., 2001), tagged and overexpressed OM45 localized to mitochondria (Figure 2.4). With a strain expressing OM45-FKBPx2 and Sec21-FRB, growth was only partially inhibited by rapamycin (Figure

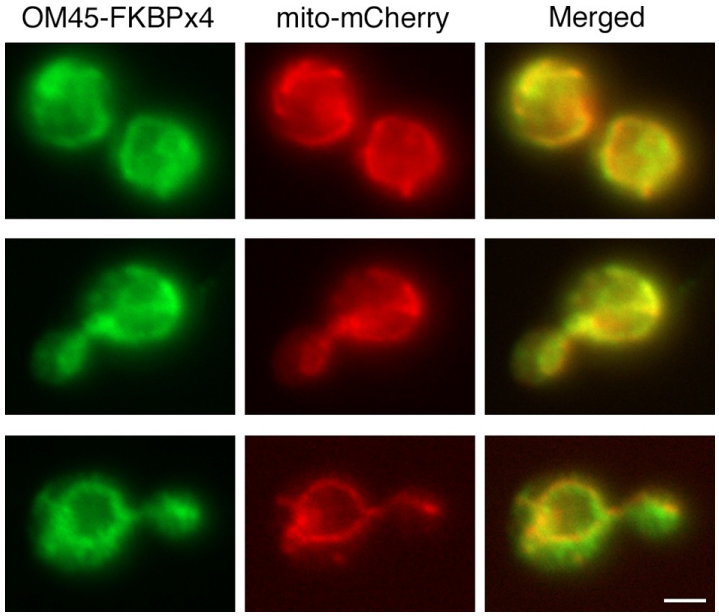

Figure 2.4: Localization of FKBP-tagged OM45 to mitochondria. Cells containing mitochondria labeled with matrix-targeted mCherry (red) were engineered to express OM45-FKBPx4, which includes a single C-terminal HA epitope tag. The cells were processed for immunofluorescence microscopy using a polyclonal rabbit anti-HA antibody followed by Alexa Fluor 488-conjugated goat anti-rabbit IgG (green). Samples were then visualized by widefield microscopy. Merged images show colocalization of the green and red signals. Scale bar, 2 μm.

2.2B). A likely explanation is that binding of FRB to FKBP-rapamycin is readily reversible (Banaszynski et al., 2005). If so, then why is the ribosomal anchor more effective than the mitochondrial anchor? We believe the answer is that ribosomes are present throughout the cytoplasm whereas mitochondria have a more restricted location. After dissociating from an Rpl13A-FKBPx2 anchor, Sec21-FRB will quickly be captured again by encountering another ribosome, whereas after dissociating from an OM45-FKBPx2 anchor, Sec21-FRB may have time to function at the Golgi before encountering another mitochondrion.

To test this hypothesis, we added a double FRB tag to Sec21 while increasing the number of FKBP domains on OM45 to four. These changes were predicted to increase the functional affinity of the anchoring interaction at mitochondria. Indeed, with a strain expressing OM45-FKBPx4 and Sec21-FRBx2, rapamycin completely blocked growth (Figure 2.2B). We also tried constructing a strain that expressed Rpl13A-FKBPx4 and Sec21-FRBx2, but growth was slow, perhaps because the functional affinity of the interaction was high enough to

compromise COPI even in the absence of rapamycin (data not shown). In conclusion, growth assays indicate that effective anchoring can be achieved using either Sec21-FRB with a ribosomal Rpl13A-FKBPx2 anchor, or Sec21-FRBx2 with a mitochondrial OM45-FKBPx4 anchor.

As a control, we verified that anchoring of COPII also caused growth inhibition, as previously observed with *Pichia pastoris* (Bharucha et al., 2013). For this purpose, we added a single- or double-FRB tag to the essential COPII coat subunit Sec31 (Salama et al., 1997). The anchors were Rpl13A or OM45, linked to either two or four copies of FKBP. As shown in Figure 2.2C, all of the strains grew well, even the one with the Rpl13A-FKBPx4/Sec31-FRBx2 combination, and rapamycin blocked growth of all of the strains, even the one with the OM45-FKBPx2/Sec31-FRB combination. Thus, the anchor-away method is effective for inactivating components of the secretory pathway, but different components vary in their sensitivities to specific tag-anchor combinations.

Anchoring Sec21 to mitochondria also displaces other COPI subunits

For further analysis, we relied mainly on the mitochondrial anchor because rapamycin-driven redistribution of labeled proteins to mitochondria can be easily visualized. The first step was to monitor the time course of the anchor-away process using Sec21-FRBx2-GFP with OM45-FKBPx4. The mitochondria were also labeled with matrix-localized mCherry. Prior to rapamycin addition, Sec21-FRBx2-GFP was present on punctate early Golgi structures that showed no consistent association with mitochondria (Figure 2.5A). At 10 min after addition of rapamycin at 23°C, Sec21-FRBx2-GFP showed substantial association with mitochondria (Figure 2.5A). Quantitation of the overlap indicated that this redistribution was maximal by 10-15 min after rapamycin addition, reaching a level of 75-80% colocalization of Sec21-FRBx2-GFP with the mitochondrial matrix marker (Figure 2.5B). We then examined strains in which Sec21-FRBx2 was nonfluorescent, with the GFP tag fused instead to other COPI subunits. Rapamycin-driven anchoring of Sec21-FRBx2 caused redistribution of Ret1-GFP

or Sec26-GFP to mitochondria (Figure 2.6). Thus, the anchor-away method redistributes the entire COPI complex.

An interesting question was whether COPI became anchored to mitochondria as an isolated complex, or whether it remained bound to Golgi membranes that became tethered to mitochondria. The anchored COPI was often punctate rather than being evenly distributed over the mitochondria (Figure 2.5A), suggesting that entire Golgi compartments were being tethered. We analyzed cells that contained GFP-Vrg4 as an early Golgi marker and Ret1-mCherry as a COPI marker, plus a blue fluorescent marker for the mitochondrial matrix (Murley et al., 2013). Rapamycin-driven anchoring of COPI to mitochondria using Sec21-FRBx2 also displaced GFP-Vrg4 (Figure 2.5C), indicating that at least some of the anchored COPI retained its association with Golgi membranes. Although anchored COPI can still bind to the Golgi, the simultaneous anchoring to mitochondria or ribosomes evidently prevents COPI from performing its essential functions.

Anchoring COPI inhibits recycling to the ER

If anchored COPI is functionally inactive as suggested by the growth curve analysis, then recycling of proteins from the Golgi to the ER should be inhibited. To test this prediction, we used a construct encoding the membrane domain (TMD) of the ER protein Sec71 fused to GFP (Sato et al., 2003). Sec71TMD-GFP localizes to the ER with the aid of the retrieval receptor Rer1 (Sato et al., 2003), which recycles from the Golgi to the ER in a COPI-dependent manner (Boehm et al., 1997; Sato et al., 2001). Control experiments confirmed that Sec71TMD-GFP was in the ER as indicated by nuclear envelope fluorescence plus additional fluorescence from peripheral ER structures (Sato et al., 2003). When Sec71TMD-GFP was expressed using an integrating vector in a wild-type strain, a bright ER signal was seen in essentially all of the cells (Figure 2.7A). By contrast, in an *rer1*Δ mutant strain, the Sec71TMD-GFP signal in the ER was faint (Figure 2.7A). The *rer1*Δ strain showed a vacuolar lumen signal as previously reported (Sato et al., 2003), although the strength of

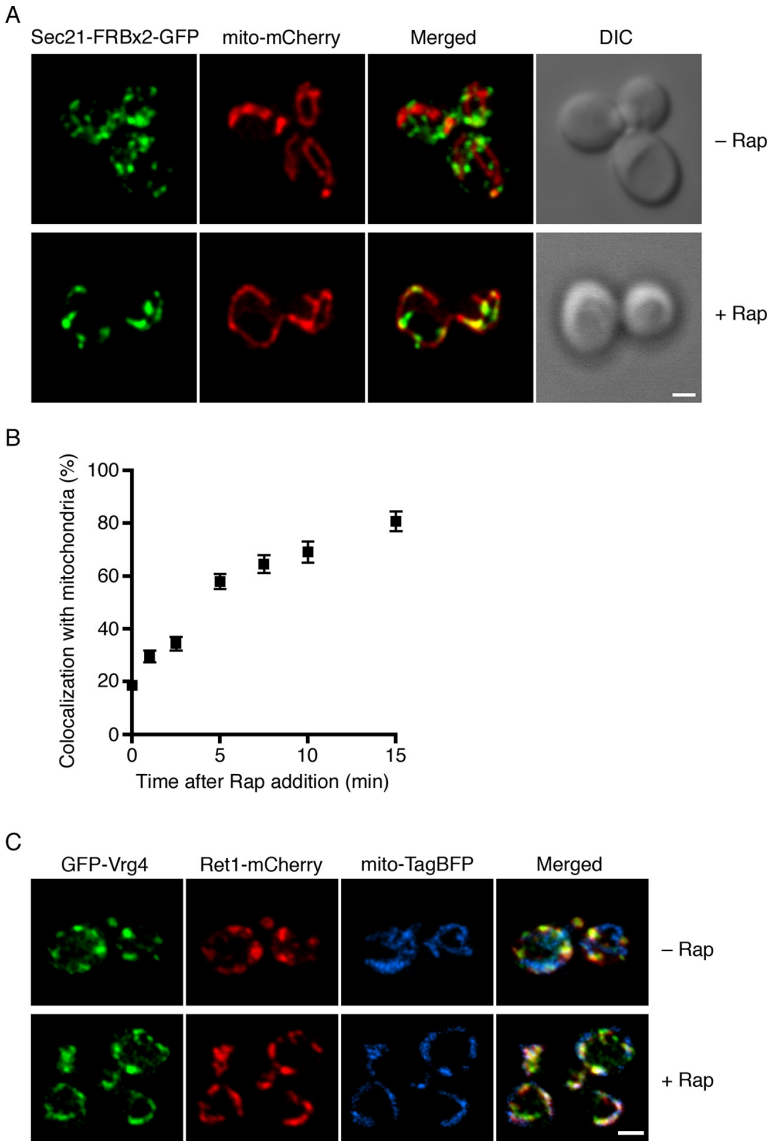

Figure 2.5: Visualization of COPI anchoring to mitochondria.(A) Sec21 tagged with FRBx2-GFP can be anchored to mitochondria containing OM45-FKBPx4. The mitochondrial matrix was labeled with mCherry. Representative cells are shown before drug treatment, and after treatment for 10 min at 23°C with 1 μg/mL rapamycin ("Rap"). Cells were imaged by confocal microscopy followed by deconvolution. Scale bar, 2 μm. (B) Maximal anchoring to mitochondria occurs within 1015 min. Anchoring of Sec21-FRBx2-GFP was quantified by measuring the fraction of the GFP signal that colocalized with the mCherry signal (Levi et al., 2010) at different times after rapamycin addition at 23°C. Approximately 2030 cells were analyzed at each time point. Error bars show s.e.m. (C) Anchoring COPI also anchors early Golgi cisternae. Sec21 was tagged with FRBx2 in a strain with the OM45-FKBPx4 mitochondrial anchor. The strain also expressed GFP-Vrg4 to label early Golgi cisternae, Ret1-mCherry to label COPI, and mito-TagBFP to label the mitochondrial matrix. Cells were imaged before or after rapamycin addition as in (A).

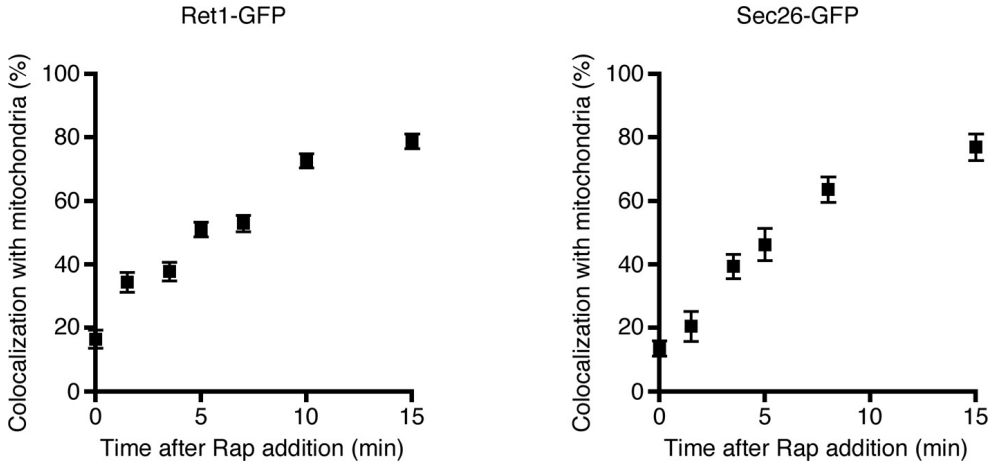

Figure 2.6: Simultaneous anchoring of multiple COPI subunits to mitochondria. Quantitation of time-dependent anchoring to mitochondria was performed as in Figure 2.5B, except that Sec21 was tagged with FRBx2 and the GFP tag was appended to either Ret1 or Sec26.

this signal varied between cells, probably because older cells had degraded more mislocalized Sec71TMD-GFP molecules and had therefore accumulated more GFP in the vacuole. These results validate the use of ER localization of Sec71TMD-GFP as a readout for Golgi-to-ER recycling.

We predicted that inactivation of COPI would prevent Rer1-dependent Golgi-to-ER recycling while allowing ER export, and would therefore reduce Sec71TMD-GFP levels in the ER. This reduction was expected to be gradual because Sec71TMD-GFP lacks a known ER export signal and should be incorporated at a low efficiency into COPII vesicles (Dancourt and Barlowe, 2010). In a control strain that contained the mitochondrial OM45-FKBPx4 anchor, addition of rapamycin had no effect on the amount of Sec71TMD-GFP in the ER, as indicated by the fluorescence signal from the nuclear envelope (Figure 2.7B,C and Figure 2.8). By contrast, when the OM45-FKBPx4 strain also contained Sec21-FRBx2 for anchoring COPI, addition of rapamycin caused progressive depletion of Sec71TMD-GFP from the ER (Figure 2.7B,C and Figure 2.8). After 60 min of rapamycin treatment, the level of Sec71TMD-GFP in the ER was comparable to that seen in the *rer1*Δ strain (dashed line in Figure 2.7C). This observation provides further evidence that anchoring to mitochondria inactivates COPI.

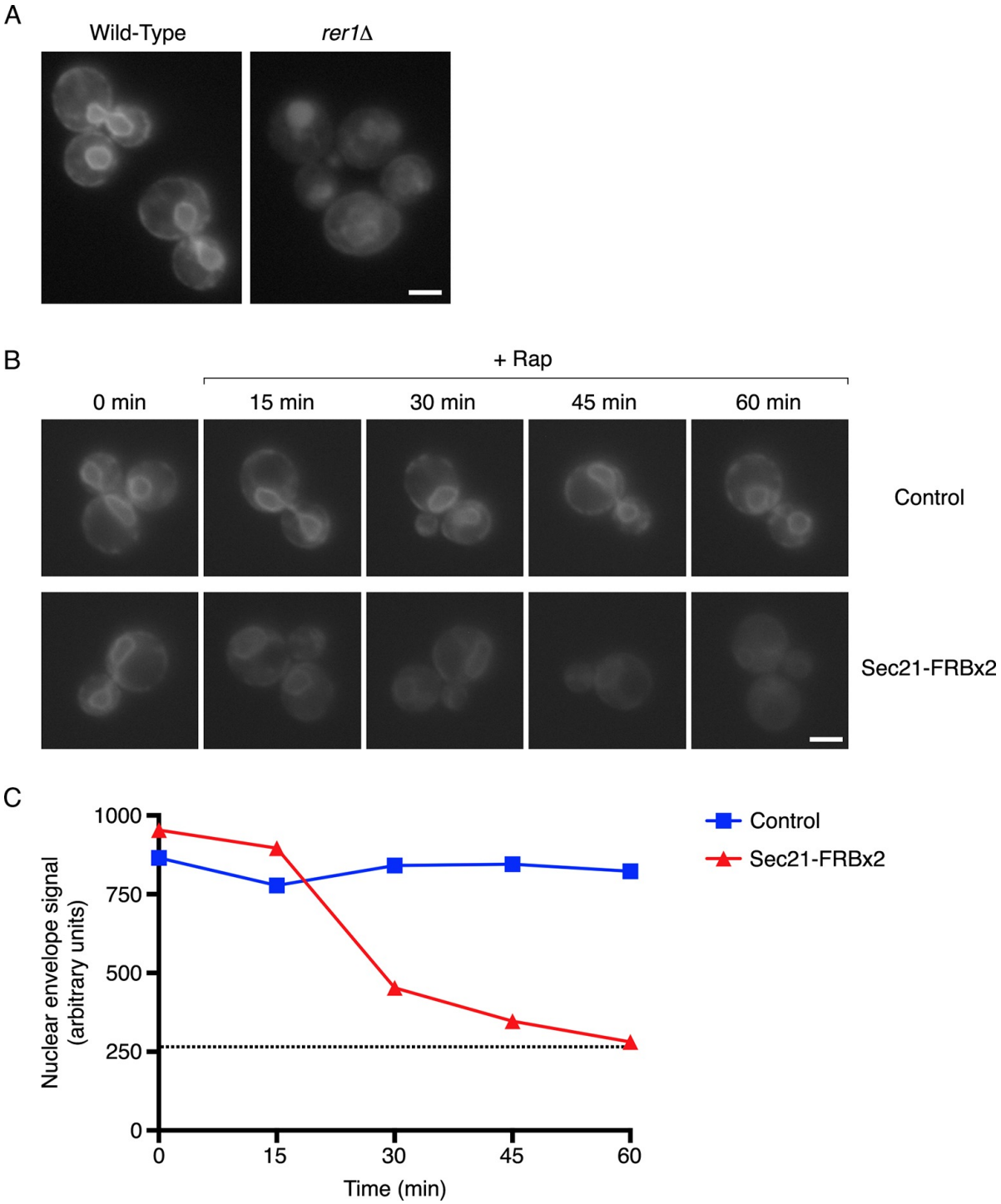

Figure 2.7: Depletion of Sec71TMD-GFP from the ER after COPI inactivation *(legend on next page)*

Figure 2.7: Depletion of Sec71TMD-GFP from the ER after COPI inactivation. (A) Sec71TMD-GFP requires Rer1 for normal ER localization. An expression vector for Sec71TMD-GFP was integrated into the wild-type JK9-3da strain or into an isogenic *rer1*Δ strain. Cells grown to log phase in NSD at 30°C were compressed beneath a coverslip and visualized in a single focal plane by widefield microscopy. Representative images taken at the same exposure are shown. Scale bar, 2 μm. (B) Anchoring of COPI causes loss of Sec71TMD-GFP from the ER. Both of the strains shown here contained integrating vectors for expressing the mitochondrial anchor OM45-FKBPx4 as well as Sec71TMD-GFP, and one strain also expressed Sec21-FRBx2 to anchor COPI. Cells growing at 30°C were incubated for 10 min with 0.0002% Hoechst 33342 to stain nuclei, followed by an additional treatment for up to 60 min with 1 μg/mL rapamycin ("Rap"). At the indicated time points after rapamycin addition, cells were compressed beneath a coverslip and visualized in a single focal plane by widefield microscopy. Representative images of GFP fluorescence are shown. Scale bar, 2 μm. (C) The data from (B) were quantified by measuring the GFP fluorescence signals from nuclei as a proxy for the ER signals. For this purpose, the signal in the blue channel was used to select nuclei in ImageJ using the Magic Wand tool. These selections were expanded by 12 pixels to include the nuclear envelope, and the GFP fluorescence from the selected areas in the green channel was quantified. Plotted are average fluorescence signals per unit area. Each data point was derived from approximately 4080 cells, and was adjusted by subtracting an average background signal from nuclei in the parental strain lacking GFP. The dashed line represents the average background-corrected nuclear fluorescence signal from *rer1*Δ cells that exhibited low to moderate vacuolar fluorescence.

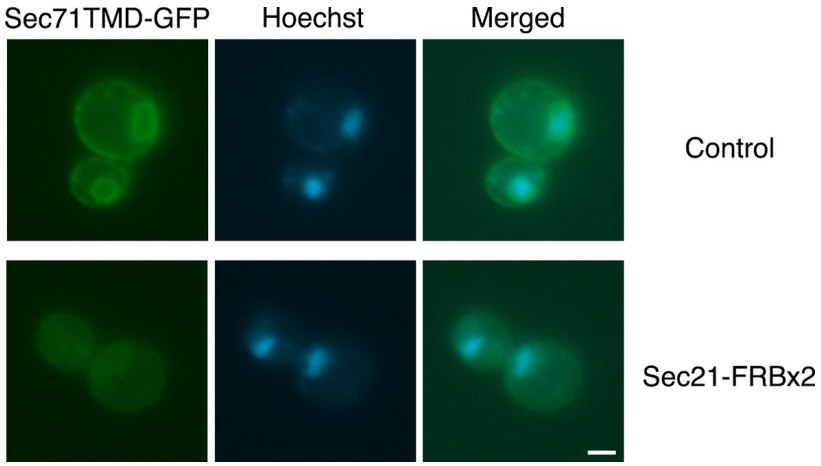

Figure 2.8: Labeling of nuclei to quantify Sec71TMD-GFP fluorescence in the nuclear envelope. Representative cells are shown from the analysis in Figure 2.7B,C at 60 min after rapamycin addition. The Sec71TMD-GFP fluorescence signal is shown in green, and cellular DNA stained with Hoechst dye is shown in blue. Hoechst-labeled nuclei were used to identify the nuclear envelope component of the Sec71TMD-GFP signal.

Anchoring COPI reduces but does not block secretion

To determine how COPI inactivation affects forward traffic through the secretory pathway, we examined general secretion. Cells were incubated at 30°C with ^{35}S-labeled amino acids during a 10-min pulse and then chased for 30 min, followed by analysis of the radiolabeled proteins secreted into the culture medium (Gaynor and Emr, 1997). This procedure was performed either with untreated cells, or with cells that had received rapamycin 10 min before the pulse.

In a control strain that contained the mitochondrial OM45-FKBPx4 anchor, a series of radioactive protein bands was detected in the absence of rapamycin, and this pattern was unchanged by addition of rapamycin (Figure 2.9A). However, when the OM45-FKBPx4 strain also contained Sec31-FRBx2 for anchoring the outer layer of the COPII coat, general secretion was completely blocked by rapamycin addition (Figure 2.9A). As a control, rapamycin had no effect on cellular protein synthesis (Figure 2.10). The inhibitory effect of anchoring Sec31-FRBx2 was expected because proteins following the conventional secretory pathway all require COPII to leave the ER (Barlowe and Miller, 2013).

When the OM45-FKBPx4 strain also contained Sec21-FRBx2 for anchoring COPI, general secretion was reduced but not abolished (Figure 2.9A). We extended this test by comparing three different anchoring configurations for COPI (Figure 2.9B). In a strain that contained the ribosomal Rpl13A-FKBPx2 anchor and Sec21-FRB, rapamycin reduced secretion to a similar extent as in the strain that contained the mitochondrial OM45-FKBPx4 anchor and Sec21-FRBx2. However, in a strain that contained the mitochondrial OM45-FKBPx2 anchor and Sec21-FRB, rapamycin had only a marginal effect on secretion. These results fit with the growth tests indicating that a single copy of FRB is sufficient to inactivate COPI using the ribosomal anchor, but that two copies of FRB are needed using the mitochondrial anchor (see above).

Figure 2.9A shows that after anchoring COPI, the secretion of some proteins was only weakly inhibited as marked by the arrow, whereas the secretion of other proteins was strongly

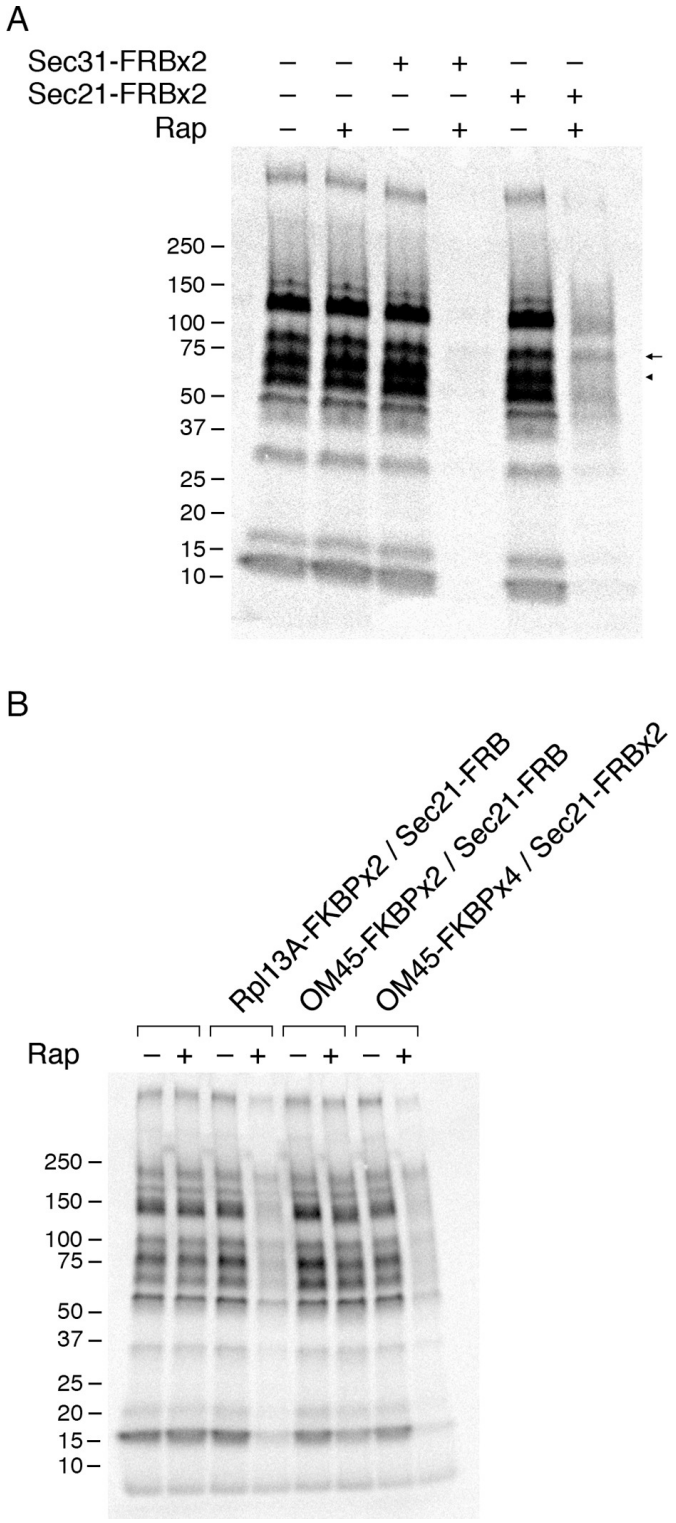

Figure 2.9: Effects of anchoring COPI or COPII on general secretion *(legend on next page)*

Figure 2.9: Effects of anchoring COPI or COPII on general secretion. (A) Anchoring COPII inhibits secretion more strongly than anchoring COPI. The yeast strains used here all expressed the mitochondrial anchor OM45-FKBPx4. Where indicated, a strain also expressed either Sec31-FRBx2 to anchor COPII, or Sec21-FRBx2 to anchor COPI. Cells growing at 30°C were either left untreated or treated for 10 min with 1 μg/mL rapamycin ("Rap"), then pulsed for 10 min with ^{35}S amino acids, then chased for 30 min. The culture medium was analyzed by SDS-PAGE and autoradiography to detect secreted proteins that had been labeled during the pulse. Numbers represent the molecular weight in kDa of marker proteins. After anchoring COPI, the arrow marks a band of secreted protein that was only partially diminished, and the arrowhead marks a band of secreted protein that was severely diminished. (B) Efficient anchoring of Sec21 requires two copies of FRB with a mitochondrial anchor but only one copy of FRB with a ribosomal anchor. General secretion was visualized by a pulse-chase procedure as in (A), except that the control strain expressed neither an anchor nor an FRB-tagged protein. Where indicated, a strain expressed either a ribosomal Rpl13A-FKBPx2 anchor or a mitochondrial OM45-FKBPx2 or OM45-FKBPx4 anchor, plus either Sec21-FRB or Sec21-FRBx2.

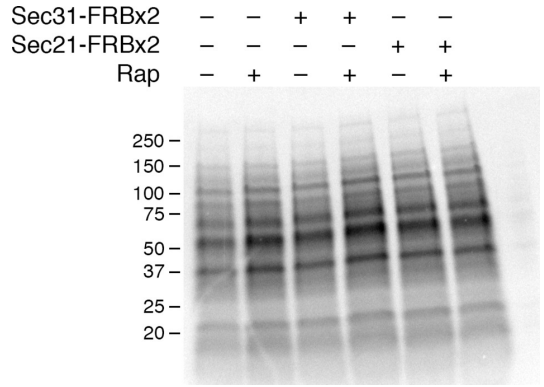

Figure 2.10: Insensitivity of cellular protein synthesis to rapamycin. The experimental procedure was identical to the one in Figure 2.9A, except that cellular proteins were analyzed rather than proteins secreted into the culture medium. A control (data not shown) confirmed that as in Figure 2.9A, rapamycin inhibited general secretion completely when COPII was anchored away, but only partially when COPI was anchored away. Numbers represent the molecular weight in kDa of marker proteins.

inhibited as marked by the arrowhead. Many proteins fell between these two extremes, showing extensive but not complete inhibition. Similar results were obtained when the rapamycin concentration was doubled to 2 μg/mL and the drug pretreatment was varied between 5 and 30 min (Figure 2.11). Moreover, when the FRBx2 tag was placed on Ret1 instead of Sec21, rapamycin inhibited growth and anchored COPI but only partially inhibited secretion (Figure 2.12), mimicking the effects seen with Sec21-FRBx2. Even when both Sec21 and Ret1

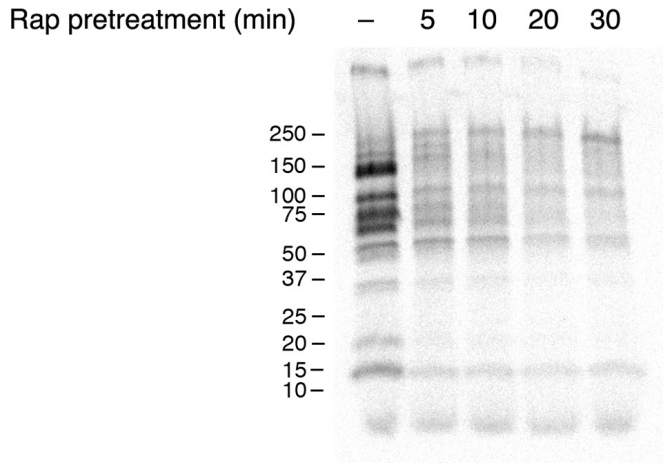

Figure 2.11: Time course of the rapamycin effect on general secretion. The yeast strain expressed the mitochondrial anchor OM45-FKBPx4, and also expressed Sec21-FRBx2 to anchor COPI. Cells growing at 30°C were either left untreated or treated for the indicated times with 2 μg/mL rapamycin ("Rap"), then pulsed for 10 min with ^{35}S amino acids, then chased for 30 min. The culture medium was analyzed by SDS-PAGE and autoradiography to detect secreted proteins that had been labeled during the pulse. Numbers represent the molecular weight in kDa of marker proteins.

were tagged with FRBx2, rapamycin did not fully inhibit secretion (Figure 2.12). Based on these data, we conclude that COPI inactivation allows general secretion to continue at a reduced level, with the magnitude of the reduction varying for different proteins.

The effects of anchoring COPI resemble the effects of the sec21-3 mutation

Because the effects of anchoring COPI are similar to those previously seen after thermal inactivation of COPI in a *sec21-3* mutant (Gaynor and Emr, 1997), we performed a direct comparison of the two approaches. Sequencing of genomic DNA from a *sec21-3* mutant strain revealed that this allele carries a single F720S point mutation. We introduced this mutation into our parental strain by gene replacement. As anticipated, the *sec21-3* mutant cells grew at 23°C but not at 37°C (Figure 2.14).

The *sec21-3* mutant was shifted to 37°C for 30 min prior to pulse-chase analysis. In parallel, anchoring to mitochondria was performed at 37°C. As shown in Figure 2.13, the *sec21-3* mutation had the same effect on general secretion as anchoring Sec21-FRBx2. In

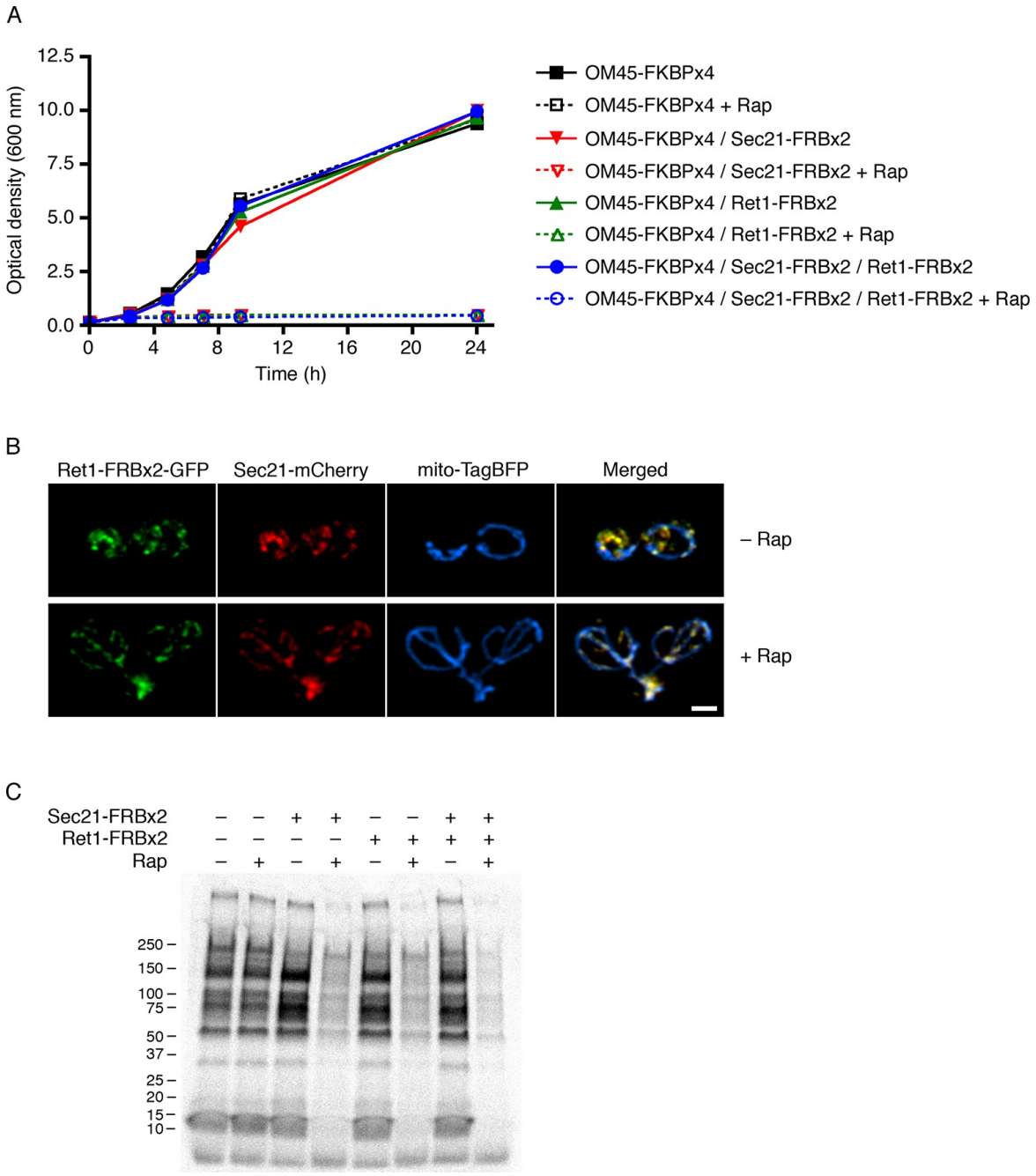

Figure 2.12: Partial inhibition of secretion after anchoring different COPI subunits. (A) Growth was monitored with or without rapamycin addition as in Figure 2.2. The parental strain carried the OM45-FKBPx4 anchor. Where indicated, the strains also carried Sec21-FRBx2 or Ret1-FRBx2 or both. (B) A strain carrying the OM45-FKBPx2 anchor was modified to express Ret1-FRBx2-GFP and Sec21-mCherry. Confocal microscopy revealed that addition of 1 μg/mL rapamycin ("Rap") for 10 min at 23°C anchored both tagged COPI subunits to mitochondria, which were labeled with mito-TagBFP. Scale bar, 2 μm. (C) The strains in (A) were subjected to pulse-chase analysis to detect general secretion as in Figure 2.9A.

both cases, secretion was inhibited to varying extents for different proteins. Anchoring Sec31-FRBx2 at 37°C completely blocked general secretion (Figure 2.13), confirming that secretion has a more stringent requirement for COPII than for COPI.

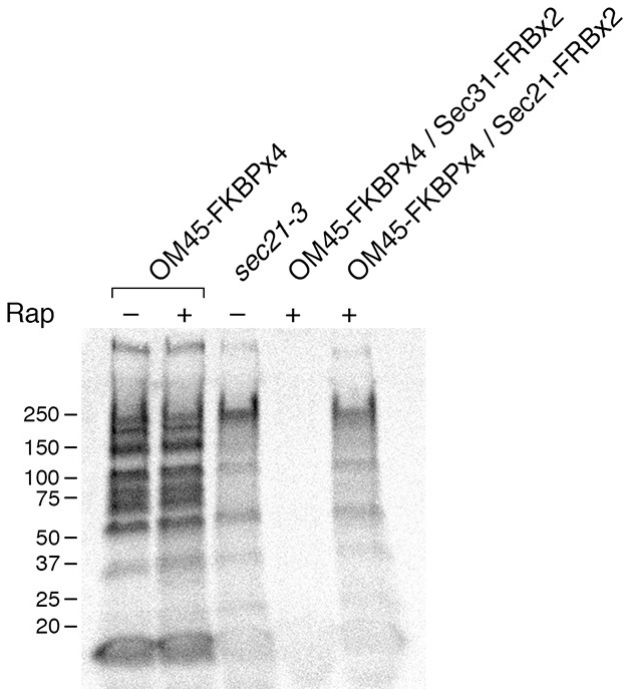

Figure 2.13: Comparison of methods for inactivating Sec21. General secretion was visualized by a pulse-chase analysis as in Figure 2.9A, except that cells were grown at 23°C and then shifted to 37°C for 30 min before the procedure. A control strain expressed the mitochondrial OM45-FKBPx4 anchor. Where indicated, a strain expressed OM45-FKBPx4 plus either Sec31-FRBx2 to anchor COPII or Sec21-FRBx2 to anchor COPI. The *sec21-3* mutation was in the parental strain background. "Rap" indicates a 10-min treatment with 1 μg/mL rapamycin prior to the pulse. Numbers represent the molecular weight in kDa of marker proteins.

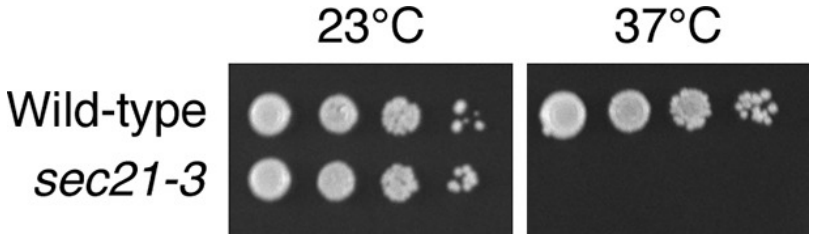

Figure 2.14: Thermosensitivity of the *sec21-3* strain. Ten μL of 10-fold serial dilutions of wild-type or isogenic *sec21-3* mutant cells were spotted in parallel on two YPD plates. The plates were then incubated for two days at either 23°C or 37°C.

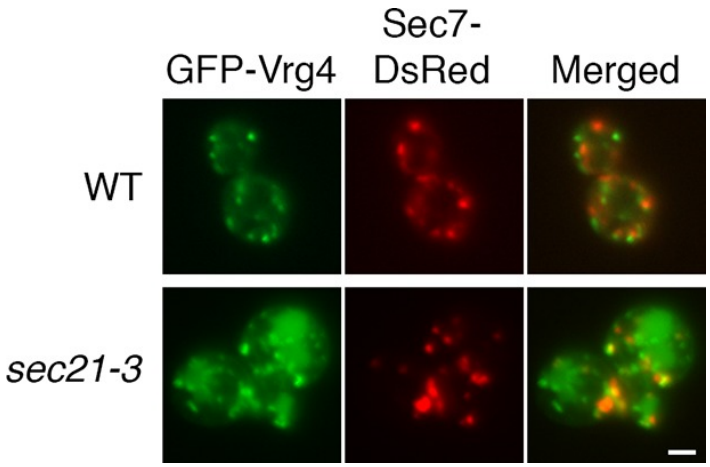

Figure 2.15: Perturbed Golgi structure in *sec21-3* cells at the permissive temperature. A wild-type strain or an isogenic *sec21-3* strain were transformed to express the early Golgi marker GFP-Vrg4 and the late Golgi marker Sec7-DsRed. Cells were imaged at 23°C by widefield microscopy. Representative cells are shown. Scale bar, 2 μm.

These results suggested that the *sec21-3* mutant strain might be useful for a fluorescence microscopy analysis of how COPI inactivation affects the Golgi. Unfortunately, when the *sec21-3* strain was transformed to express the early Golgi marker GFP-Vrg4 and the late Golgi marker Sec7-DsRed (Losev et al., 2006), Golgi organization was perturbed even at the permissive temperature. Compared to a wild-type control strain, the size of the labeled puncta was more variable, and a greater fraction of the GFP-Vrg4 marker was found in non-punctate structures (Figure 2.15). Thus, the anchor-away approach is preferable for microscopy because Golgi organization should be normal prior to rapamycin addition.

Anchoring COPI leads to formation of hybrid Golgi structures

We asked whether Golgi organization was altered by inactivating COPI. The first test employed fluorescence microscopy with GFP-Vrg4 and Sec7-DsRed. As previously observed (Losev et al., 2006), early and late cisternae appeared as distinct puncta in the absence of rapamycin (Figure 2.16A). In a strain carrying the OM45-FKBPx4 anchor and wild-type Sec21, addition of rapamycin had no effect on this pattern (Figure 2.16A). However, in a

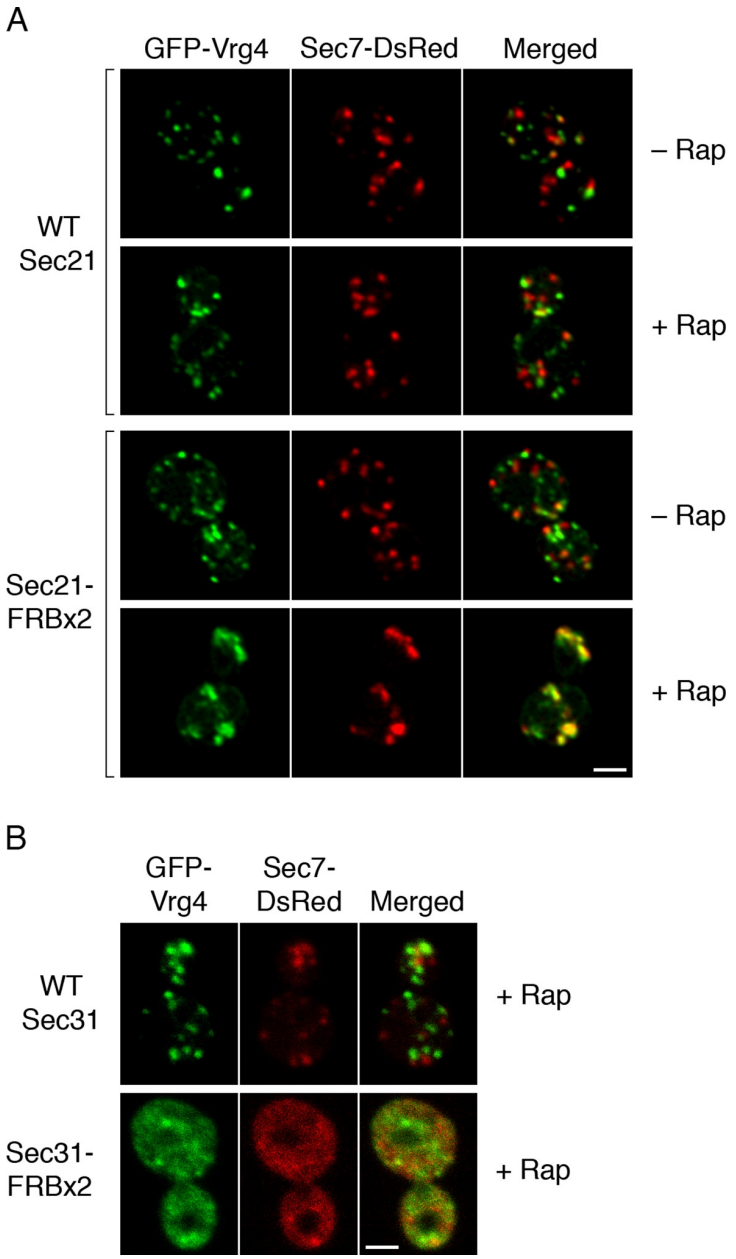

Figure 2.16: Effects of anchoring COPI or COPII on Golgi organization. (A) Anchoring COPI leads to association of early and late Golgi markers. A strain carrying the OM45-FKBPx4 anchor was transformed to express the early Golgi marker GFP-Vrg4 and the late Golgi marker Sec7-DsRed. A derivative strain also expressed Sec21-FRBx2 to anchor COPI. Cells were grown and imaged as in Figure 2.1, except that the confocal images were deconvolved. "+ Rap" indicates a 10-min treatment with 1 μg/mL rapamycin prior to imaging. Scale bar, 2 μm. (B) Anchoring COPII does not lead to association of early and late Golgi markers. The experiment was performed with rapamycin addition as in (A), except that the strain expressed Sec31-FRBx2 to anchor COPII, and deconvolution was omitted. Similar results were seen when COPII was anchored to mitochondria by incubating with rapamycin for 10 min as in the figure, or for 20 min (data not shown).

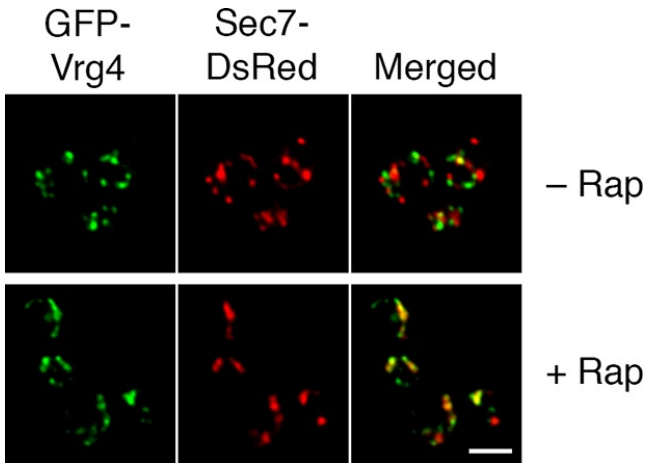

Figure 2.17: Formation of hybrid Golgi structures with a ribosomal anchor. The analysis was performed as in the lower half of Figure 2.16A, except that the strain carried the Rpl13A-FKBPx2 ribosomal anchor plus Sec21-FRB to anchor COPI. Scale bar, 2 μm.

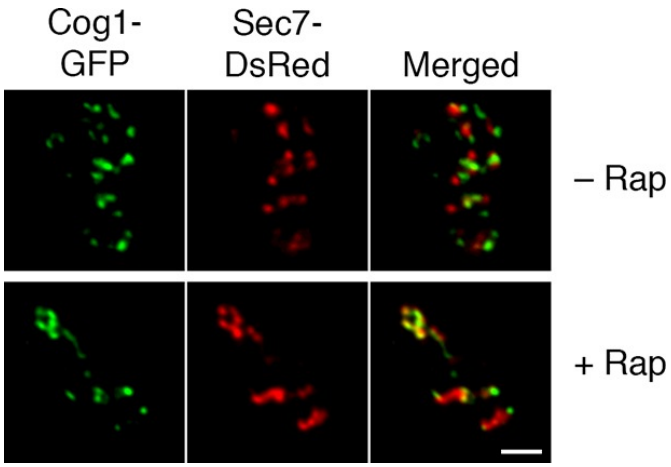

Figure 2.18: Visualization of hybrid Golgi structures with an alternative early Golgi marker. The analysis was performed as in the lower half of Figure 2.16A, except that the early Golgi was marked with Cog1-GFP. Scale bar, 2 μm.

strain carrying OM45-FKBPx4 plus Sec21-FRBx2, addition of rapamycin for 10 min to anchor COPI caused a dramatic change: the labeled structures were fewer in number and often larger, and many of them showed colocalization of the early and late Golgi markers (Figure 2.16A). The green and red fluorescence patterns were typically not identical, suggesting that the early and late Golgi markers were associated but partially segregated. This altered distribution of Golgi markers remained largely unchanged after prolonged treatment with rapamycin, except that after 30 min, some of the GFP-Vrg4 began to appear at the vacuolar

membrane and plasma membrane (data not shown). A similar conversion of separate to partially overlapping localizations of early and late Golgi markers was seen when a ribosomal anchor was used instead of a mitochondrial anchor (Figure 2.17), or when the early Golgi marker was the Cog1 subunit of the COG vesicle tethering complex (Figure 2.18) (Willett et al., 2013). We infer that COPI inactivation generates hybrid Golgi structures containing both early and late Golgi markers.

A concern was that formation of hybrid Golgi structures might be a nonspecific consequence of perturbing membrane traffic. To exclude this possibility, we visualized Golgi markers after inactivating COPII. When a strain carrying OM45-FKBPx4 plus Sec31-FRBx2 was treated with rapamycin to anchor COPII, most of the GFP-Vrg4 and Sec7-DsRed were dispersed in the cytoplasm, with the remaining punctate structures showing little colocalization of the two markers (Figure 2.16B). This result is consistent with an earlier report that inactivation of yeast COPII disrupts the Golgi (Morin-Ganet et al., 2000). Thus, the association of early and late Golgi markers after anchoring COPI is a specific effect.

To visualize the hybrid Golgi structures at higher resolution, we built on our previous experience with imaging GFP-tagged yeast compartments by correlative fluorescence microscopy and electron tomography (Bhave et al., 2014). This method was extended to dual-color imaging by visualizing both GFP-Vrg4 and Sec7-DsRed in plastic-embedded samples (Figure 2.19, insets), and was further enhanced by examining thicker sections with scanning transmission electron microscopy (STEM) tomography (Aoyama et al., 2008; Hohmann-Marriott et al., 2009; Sousa et al., 2011). Figure 2.19A shows Golgi cisternae in untreated cells. Individual early and late Golgi cisternae are identifiable in the tomograms by correlation with the fluorescence data. The tomographic reconstruction (Movie 2.1) indicates that the Golgi cisternae were relatively simple curved structures (Preuss et al., 1992; Bhave et al., 2014), and that the early and late cisternae were not visibly connected. Figure 2.19B shows Golgi structures after COPI inactivation. The tomographic reconstruction (Movie 2.2) indicates that the early and late Golgi markers were present in irregularly shaped membrane

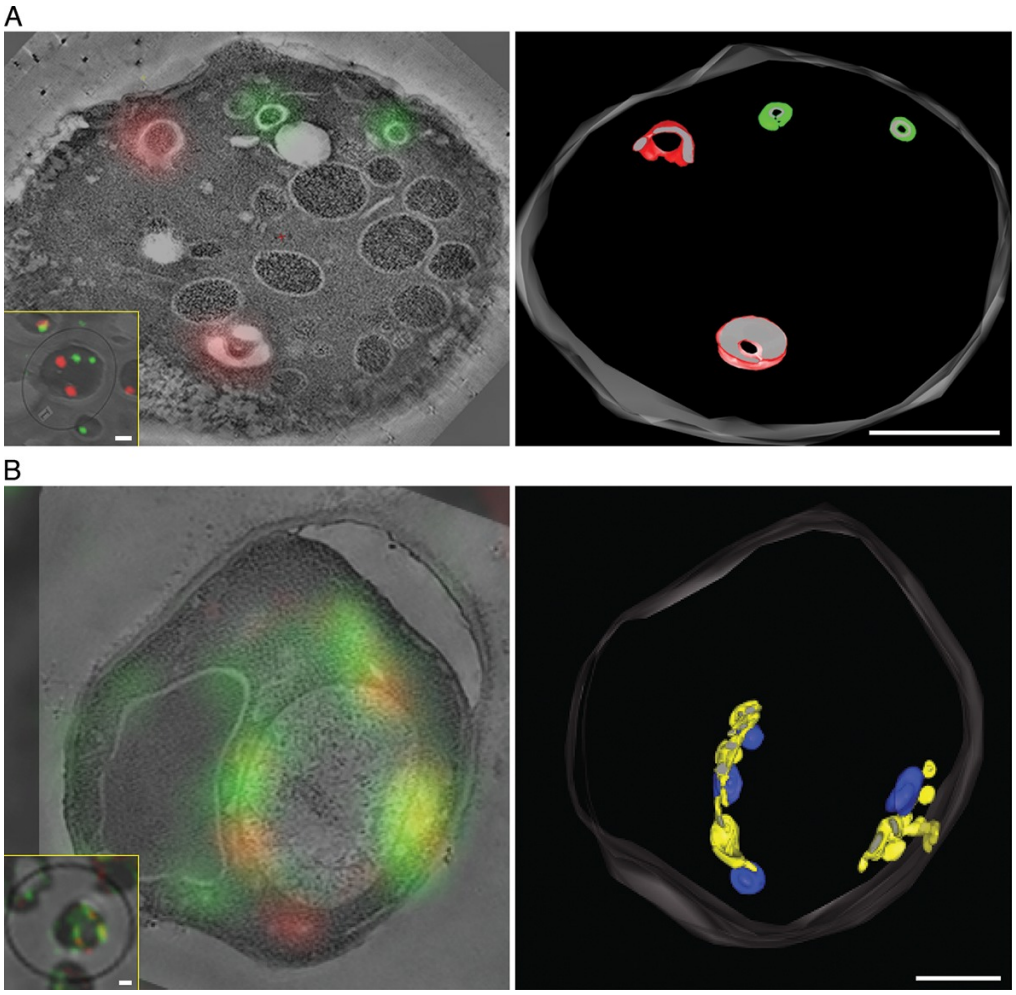

Figure 2.19: Correlative fluorescence microscopy and electron tomography of the yeast Golgi. The yeast strain expressed GFP-Vrg4 and Sec7-DsRed, as well as OM45-FKBPx4 as a mitochondrial anchor plus Sec21-FRBx2 to anchor COPI. Cells were frozen, freeze substituted, and embedded in plastic in a manner that preserved fluorescence. Plastic sections were then examined by fluorescence microscopy followed by STEM tomography. The figures show either (A) a section ∼0.5 μm thick from a representative untreated cell, or (B) a section ∼1.0 μm thick from a representative cell after treatment for 10 min with 1 μg/mL rapamycin. In each case, the left panel shows the fluorescence signals overlaid on a projection of five 3- to 4-nm tomographic slices, the inset shows fluorescence and differential interference contrast analysis of the same cell, and the right panel shows a tomographic model of the relevant labeled structures. Full tomographic reconstructions for the untreated and rapamycin-treated cells are animated in Movie 2.1 and Movie 2.2, respectively. Green indicates early Golgi cisternae, red indicates late Golgi cisternae, yellow indicates hybrid Golgi structures, and blue indicates mitochondria. Scale bars, 1 μm.

compartments of various sizes. As predicted from the fluorescence analysis (see above), some of the Golgi membranes were closely apposed to mitochondria. We conclude that COPI inactivation converts the yeast Golgi into complex membrane structures that can contain both early and late Golgi proteins.

Anchoring COPI selectively blocks recycling of an early Golgi marker

How does COPI inactivation generate hybrid Golgi structures? This question was addressed using 4D confocal microscopy. We previously showed that in unperturbed cells expressing GFP-Vrg4 and Sec7-DsRed, a cisterna labels for ∼1-3 min with the green early Golgi marker, then loses green fluorescence while acquiring red fluorescence, then labels for ∼1-3 min with the red late Golgi marker, then loses red fluorescence (Losev et al., 2006). The same maturation dynamics for GFP-Vrg4 and Sec7-DsRed were seen when a strain expressing the OM45-FKBPx4 anchor plus Sec21-FRBx2 was imaged in the absence of rapamycin (data not shown). By contrast, after the same strain had been incubated with rapamycin for 10 min to inactivate COPI, Golgi dynamics were markedly altered as described below. Rapamycin-driven tethering to mitochondria probably facilitated this analysis by making the Golgi structures less mobile and easier to track.

After COPI inactivation, two behaviors were evident from the 4D movies (Movie 2.3). First, when the early and late Golgi markers were both present in a hybrid structure, the two markers remained closely associated even though the shape of the structure fluctuated rapidly. Second, in many of the hybrid Golgi structures, the Sec7-DsRed marker disappeared and then subsequently returned while the GFP-Vrg4 marker persisted the entire time. An example from Movie 2.3 is the Golgi structure marked by an arrowhead in Figure 2.21. The dynamics of this structure are illustrated in Movie 2.4, which was generated by cropping the movie frames and then manually erasing the fluorescence of nearby structures at each time point. Figure 2.20A shows representative frames from Movie 2.4 together with a quantitation of the green and red fluorescence intensities for the entire 15-min movie. The red signal

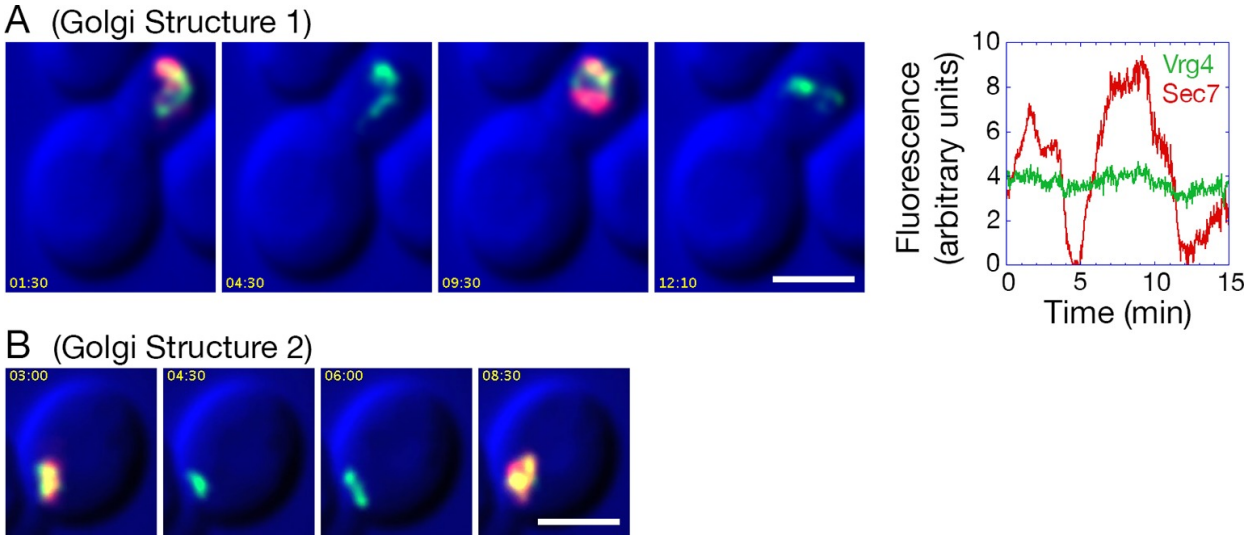

Figure 2.20: Effects of anchoring COPI on Golgi maturation dynamics. A strain expressing the OM45-FKBPx4 anchor as well as Sec21-FRBx2 was transformed to express the early Golgi marker GFP-Vrg4 and the late Golgi marker Sec7-DsRed. Logarithmically growing cells were attached to a coverglass-bottom dish, and were then treated with 1 μg/mL rapamycin for 10 min, followed by dual-color 4D confocal imaging to generate Movie 2.3. Edited data sets were generated to analyze the two hybrid Golgi structures marked in Figure 2.21, yielding Movie 2.4 for Golgi Structure 1 and Movie 2.5 for Golgi Structure 2. Times are indicated in min:sec format. Scale bars, 2 μm. (A) Representative frames are shown from Movie 2.4, and the green and red fluorescence intensities from Golgi Structure 1 are plotted versus time. (B) Representative frames are shown from Movie 2.5.

lasted for ∼4.5 min, then completely disappeared, then returned for ∼7 min, then briefly disappeared before beginning to increase once again. A similar pattern was seen with the structure marked by the arrow in Figure 2.21, although this structure could be tracked reliably for only ∼8.5 min, as illustrated in Movie 2.5. Representative frames from Movie 2.5 are shown in Figure 2.20B. In this case, the red signal disappeared for ∼2 min before returning even stronger than before. More generally, although the kinetics varied for different Golgi structures, many of them showed persistent GFP-Vrg4 labeling with alternating high and low levels of Sec7-DsRed labeling. Thus, Sec7-DsRed continued to recycle within the Golgi after COPI inactivation.

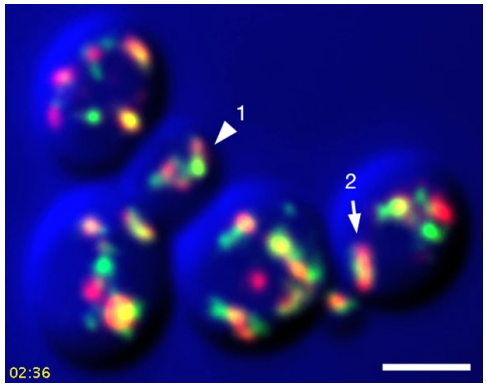

Figure 2.21: Sample frame from Movie 2.3. This frame from Movie 2.3 shows the two cisternae that were analyzed in Movie 2.4, Movie 2.5, and Figure 2.20. The arrowhead indicates Golgi Structure 1 and the arrow indicates Golgi Structure 2.

Anchoring COPI does not block recycling of a late Golgi transmembrane protein

Because Sec7 is a late Golgi peripheral membrane protein, we wondered whether late Golgi transmembrane proteins would also continue to recycle after COPI inactivation. A late Golgi transmembrane protein that may recycle within the Golgi is the processing protease Kex2 (Fuller et al., 1988). It has been proposed that Kex2 traffics between the Golgi and prevacuolar endosomes (Sipos et al., 2004; De et al., 2013), but Kex2 has no known role at prevacuolar endosomes, and the following two results suggest that the major recycling pathway for Kex2 is actually within the Golgi. First, we looked for colocalization of Kex2 with markers of the late Golgi or prevacuolar endosomes. The marker for the late Golgi was Sec7. The marker for prevacuolar endosomes was Vps8, a subunit of the CORVET tether (Arlt et al., 2015). Late Golgi compartments and prevacuolar endosomes are clearly distinct because in projected confocal images, Sec7-mCherry and Vps8-GFP showed no colocalization apart from a background level that likely represents chance overlap after projection (Figure 2.22) (Arlt et al., 2015). As a control, we examined Vps10, a vacuolar hydrolase receptor that cycles between the late Golgi and prevacuolar endosomes and localizes to both compartments (Marcusson et al., 1994; Cooper and Stevens, 1996; Chi et al., 2014). Vps10-GFP was present in a subset of the late Golgi structures labeled with Sec7-mCherry and in almost all of the prevacuolar

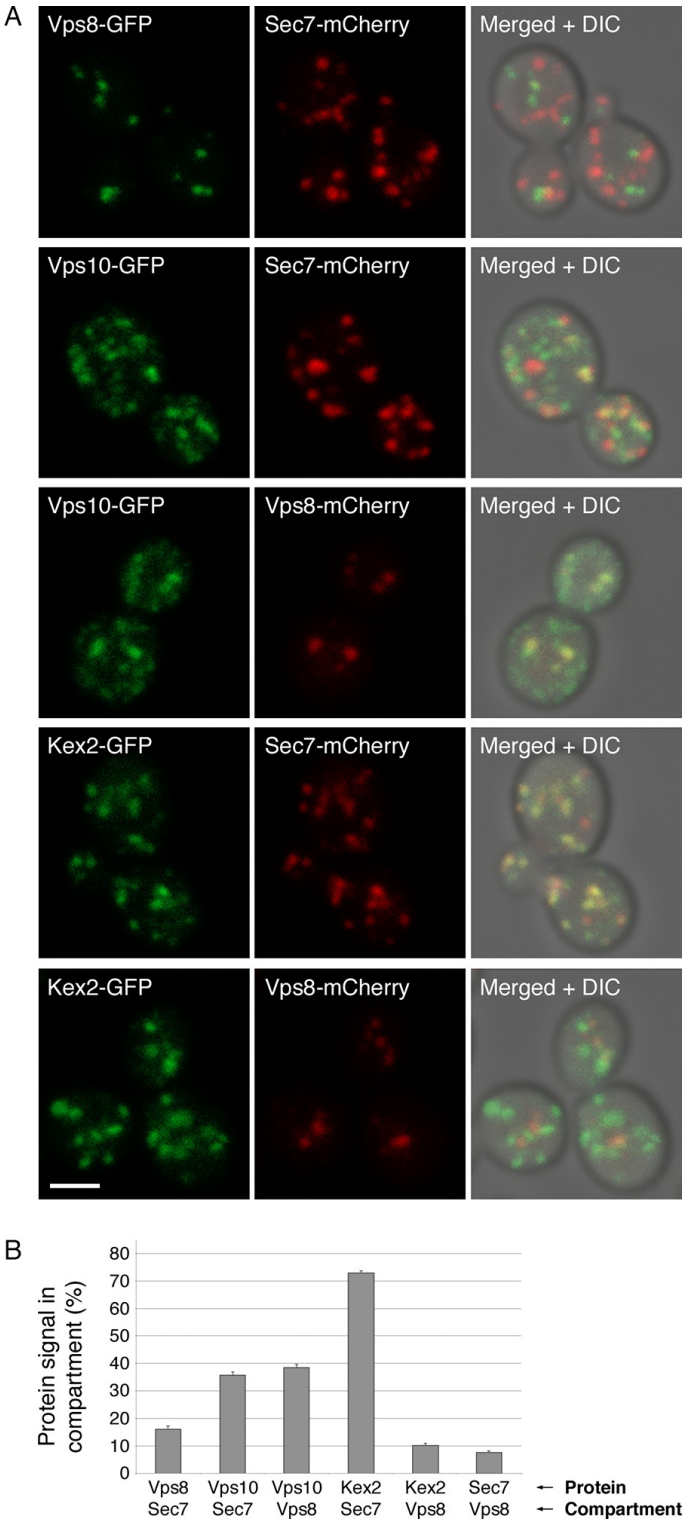

Figure 2.22: Distinct localization patterns of tagged Vps10 and Kex2 *(legend on next page)*

Figure 2.22: Distinct localization patterns of tagged Vps10 and Kex2. (A) Vps10-GFP localizes to both the Golgi and prevacuolar endosomes whereas Kex2-GFP is largely restricted to the Golgi. Late Golgi compartments were tagged with Sec7-mCherry, or else prevacuolar endosome compartments were tagged with Vps8-mCherry. The localizations of the Vps10-GFP and Kex2-GFP proteins were then examined with reference to these two compartments. As a control, Vps8-GFP was expressed together with Sec7-mCherry to confirm that the two compartments were separate. Representative projected confocal images are shown. Scale bar, 2 μm. (B) Quantitation of the data from (A). To analyze an image, a mask was created from the punctate compartment signal, and the percentage of the protein signal visible through the mask was then measured (Levi et al., 2010). For each strain, 40 images with $\sim$24 cells per image were quantified. Bars represent mean percentage values with s.e.m. Based on the analysis of Vps8 and Sec7, the background signal due to chance overlap in this assay was approximately 8-16%.

endosomes labeled with Vps8-mCherry (Figure 2.22). By contrast, Kex2-GFP colocalized strongly with Sec7-mCherry but showed very little colocalization with Vps8-mCherry (Figure 2.22). In some cells, prevacuolar endosomes did contain detectable Kex2-GFP, but this green signal was weak (Figure 2.23). These results suggest that Kex2 resides in the Golgi, and that cycling through prevacuolar endosomes represents at most a minor pathway for Kex2 trafficking.

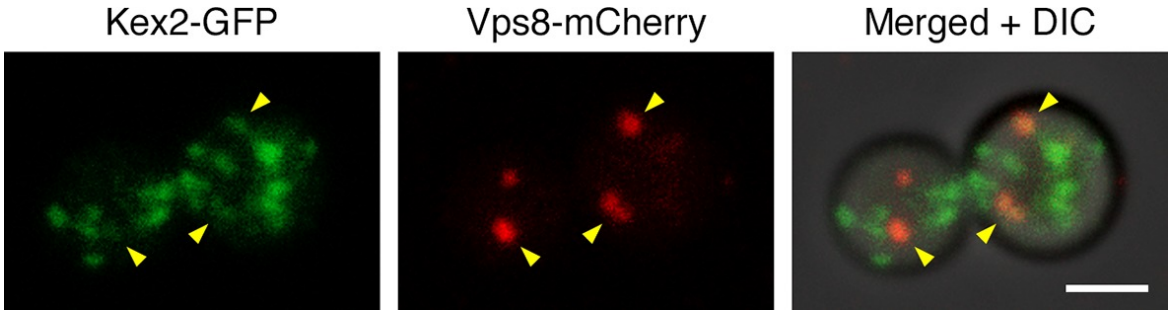

Figure 2.23: Example of an unusual cell with some Kex2-GFP visible in prevacuolar endosomes. In the experiment of Figure 2.22A, a fraction of the cells had weak but detectable Kex2-GFP signal overlapping with the Vps8-mCherry signal from prevacuolar endosomes, as indicated by the arrowheads in this example. Scale bar, 2 μm.

Second, we used 4D confocal microscopy to compare the dynamics of Kex2-GFP and Sec7-mCherry, and to determine why the colocalization of these two markers is substantial but incomplete (Franzusoff et al., 1991; Redding et al., 1991). It was recently reported that Kex2 departs from Golgi cisternae somewhat earlier than Sec7 (McDonold and Fromme, 2014). We

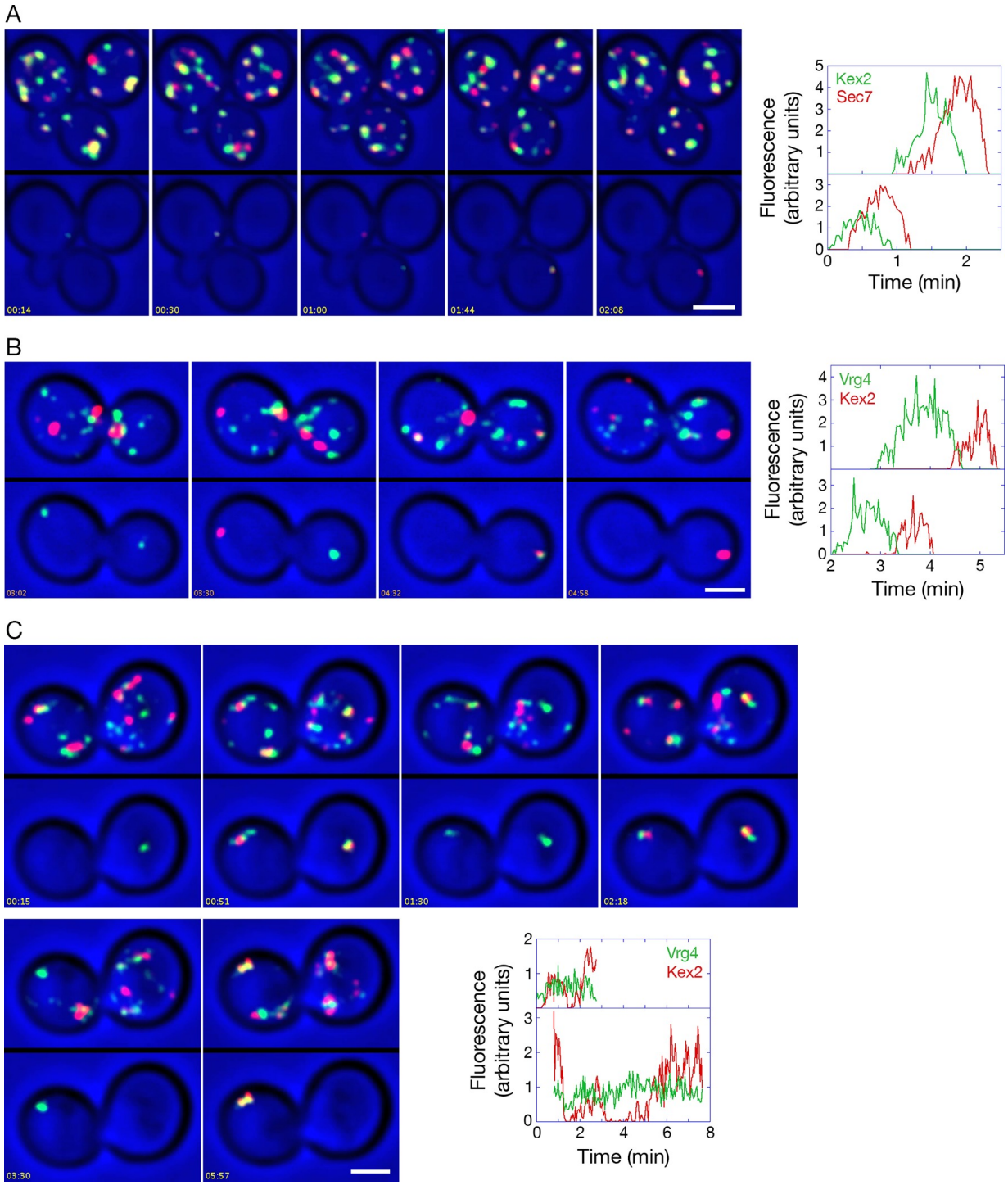

Figure 2.24: Analysis of Kex2 maturation dynamics with functional or inactivated COPI
(legend on next page)

Figure 2.24: Analysis of Kex2 maturation dynamics with functional or inactivated COPI. (A) Kex2 maturation dynamics are slightly offset from those of Sec7. Cells expressing Kex2-GFP and Sec7-mCherry were attached to a coverglass-bottom dish and imaged by dual-color 4D confocal microscopy to generate Movie 2.6, in which the top panel is the unedited movie and the bottom panel was generated from edited data sets used to quantify the fluorescence intensities from two cisternae. Representative frames from Movie 2.6 are shown together with the quantitation. Plotted in the bottom panel is fluorescence from the cisterna in the cell at the upper left, and plotted in the top panel is fluorescence from the cisterna in the cell at the lower right. Scale bar, 2 μm. (B) GFP-Vrg4 departs as Kex2-mCherry arrives during cisternal maturation. Imaging was performed as in (A), and representative frames from Movie 2.8 are shown together with the quantitation. Plotted in the bottom panel is fluorescence from the cisterna in the cell at the left, and plotted in the top panel is fluorescence from the cisterna in the cell at the right. Scale bar, 2 μm. (C) After COPI inactivation, GFP-Vrg4 persists in Golgi structures while Kex2-mCherry cycles. Imaging was performed as in (A), and representative frames from Movie 2.9 are shown together with the quantitation. Plotted in the bottom panel is fluorescence from the Golgi structure in the cell at the left, and plotted in the top panel is fluorescence from the Golgi structure in the cell at the right. These two Golgi structures were tracked for as long as they could be resolved from other fluorescent structures. Scale bar, 2 μm.

confirmed and extended that result by showing that Kex2-GFP both arrived and departed slightly before Sec7-mCherry, with the two kinetic traces typically offset by 5-20 s (Figure 2.24A and Movie 2.6). Thus, a green spot that lacks red fluorescence could represent a Golgi cisterna that has acquired Kex2-GFP and will soon acquire Sec7-mCherry. Alternatively, a green spot that lacks red fluorescence could represent a non-Golgi compartment that contains Kex2-GFP and will never contain Sec7-mCherry. To determine the relative abundance of these two classes of Kex2-GFP-labeled structures, we analyzed Movie 2.6 and identified the green spots that lacked red fluorescence and that could be reliably tracked for at least 30 s after their initial appearance. A total of 26 such structures were detected. As shown in Movie 2.7, all 26 structures subsequently acquired Sec7-mCherry. Additional Kex2-GFP-labeled structures that could not be tracked for the full 30 s also acquired Sec7-mCherry (Figure 2.25). Therefore, most or all of the structures that label strongly with Kex2-GFP are late Golgi cisternae. The straightforward interpretation of these data is that Kex2 recycles within the Golgi, with kinetics slightly offset from those of Sec7.

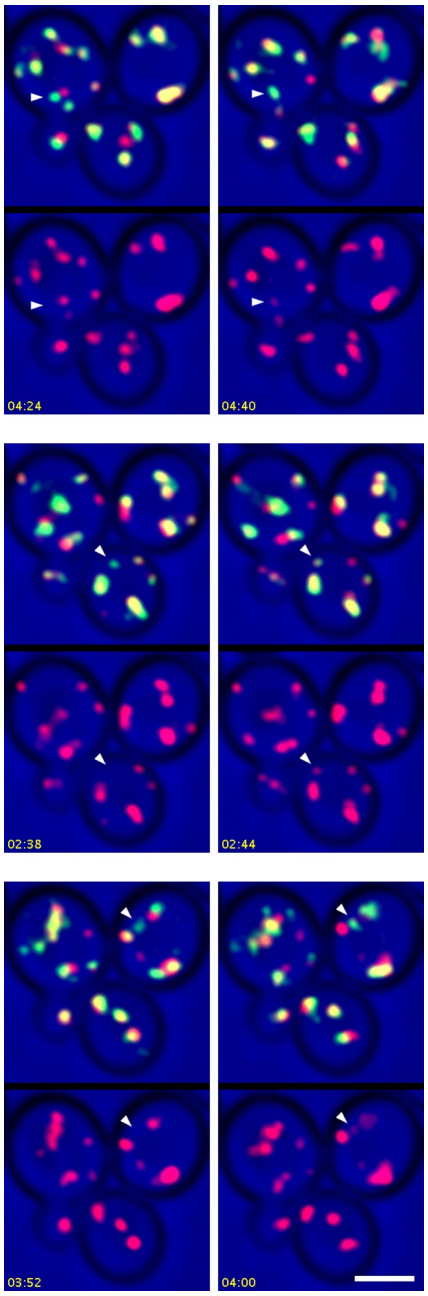

Figure 2.25: Additional examples showing the appearance of Sec7 in Kex2-containing structures. In Movie 2.7, Kex2-GFP-containing structures from Movie 2.6 were analyzed only if they could be tracked for at least 30 s after becoming visible, but additional structures that could not be tracked for the full 30 s showed initial labeling with Kex2-GFP and subsequent appearance of Sec7-mCherry. Three examples are illustrated here. See Movie 2.7 for further details.

Given that Sec7 arrives at a cisterna as Vrg4 is departing (Losev et al., 2006), we predicted that GFP-Vrg4 and Kex2-mCherry would show green-to-red maturation with a brief

period of overlap. Although Kex2-mCherry gave a comparatively weak signal that made the analysis challenging, maturation from GFP-Vrg4 to Kex2-mCherry was indeed observed (Figure 2.24B and Movie 2.8).

These control experiments set the stage for testing the effects of anchoring COPI. When COPI was inactivated, the dynamics of Kex2-mCherry were similar to those of Sec7-DsRed, with the levels of Kex2-mCherry alternately rising and falling in Golgi structures that were marked continuously by GFP-Vrg4 (Figure 2.24C and Movie 2.9). We conclude that not only peripheral membrane proteins, but also transmembrane proteins of the late Golgi can recycle independently of COPI.

The combined data suggest that COPI inactivation selectively blocks recycling of early Golgi proteins. Thus, instead of an early Golgi cisterna maturing into a late cisterna, an early cisterna matures into a hybrid structure, which eventually loses its late Golgi proteins and then begins the process anew.

Discussion

Thermosensitive yeast mutants are versatile tools for studying the secretory pathway (Duden and Schekman, 1997), but such a mutant has disadvantages. The molecular basis of the thermosensitivity is typically unknown, creating uncertainty about whether the mutant protein has been completely inactivated by the temperature shift. Moreover, a thermosensitive mutation may have detrimental effects even at the permissive temperature, in which case cellular functions will be compromised before the experiment begins. Both of these issues have been encountered with thermosensitive COPI mutants. For example, some of the commonly used COPI mutants show variable and relatively weak phenotypes (Gaynor and Emr, 1997). That issue was addressed by isolating the strong *sec21-3* mutation (Gaynor and Emr, 1997), but in our hands, Golgi morphology was perturbed in *sec21-3* cells even at the permissive temperature. Thus, thermosensitive mutants have not been ideal for examining the role of COPI in yeast.

We addressed this problem by using the anchor-away method. Growth tests indicated that wild-type FRB is suitable as a tag for gene replacement while the destabilized FRB(T2098L) mutant is not. With regard to anchors, our initial trials employed an FKBPx2-tagged version of the plasma membrane protein Pma1 (Haruki et al., 2008), but strains expressing Pma1-FKBPx2 had growth defects and were genetically unstable. Better results were obtained with the ribosomal Rpl13A-FKBPx2 anchor (Haruki et al., 2008). We also generated a mitochondrial OM45-FKBPx4 anchor, which is effective in combination with an FRBx2 tag. Control experiments indicated that these versions of the anchor-away system allow COPI to be inactivated quickly and reliably, and can therefore serve to complement thermosensitive mutants for studying COPI function. COPII can also be inactivated with the anchor-away system, although the response is slightly different than for COPI, indicating that this system needs to be tested for each component that is being inactivated.

It should be noted that "anchor-away" is something of a misnomer here because the anchored COPI remained associated with Golgi membranes. Thus, when OM45-FKBPx4 was used as the anchor, entire Golgi compartments apparently became tethered to mitochondria. Such an effect is not unexpected because Golgi cisternae are mobile in the yeast cytoplasm (Wooding and Pelham, 1998; Losev et al., 2006). Despite retaining its association with Golgi membranes, the anchored COPI was no longer functional as judged by inhibition of cell growth and of Golgi-to-ER recycling, implying that this method is suitable for studying the roles of COPI.

Our data confirm the earlier conclusion that general secretion is arrested by inactivating COPII but is only partially inhibited by inactivating COPI (Gaynor and Emr, 1997). However, instead of classifying secretory proteins in a binary fashion as being either COPI-dependent or -independent, we propose that COPI inactivation has a spectrum of effects that range from mild to severe depending on the protein. Among the proteins whose traffic was reported to be severely reduced in *sec21-3* cells at 37°C were the α-factor and carboxypeptidase Y precursors (Gaynor and Emr, 1997), both of which rely on the ER export receptor

Erv29, which recycles from the Golgi to the ER (Dancourt and Barlowe, 2010). A plausible interpretation is that for certain secretory proteins, preventing COPI-dependent recycling of the cognate ER export receptors strongly inhibits traffic (Gaynor and Emr, 1997).

This line of reasoning raises a question: how can the secretory pathway operate at all after a block in COPI-dependent recycling, given that ER-to-Golgi traffic relies on SNARE proteins that are retrieved to the ER by COPI (Barlowe and Miller, 2013)? We propose that when COPI is inactivated, the cell replenishes ER-to-Golgi SNAREs through new protein synthesis. Other components such as ER export receptors will also be replenished, but at varying rates depending on their synthesis kinetics. According to this model, COPI inactivation will have the following effects on ER export. (a) COPII vesicle production will be slowed but not halted. (b) For a given secretory protein, the rate of ER export will depend on how rapidly the cognate ER export receptor is replenished and/or how efficiently the protein is packaged into COPII vesicles in the absence of an ER export receptor.

After a secretory protein leaves the ER, COPI is thought to help drive traffic through the Golgi, yet when yeast COPI is inactivated, proteins can still be secreted. Insight into this puzzle came from fluorescence microscopy. Soon after COPI is inactivated, early and late Golgi proteins change from marking separate compartments to associating with one another in hybrid Golgi structures. These hybrid structures are very dynamic, and we suspect that the compartments containing early and late Golgi markers exchange material, although our analysis cannot determine whether this exchange involves transient fusion events or other types of transport intermediates. In any case, the hybrid Golgi structures have early Golgi character, so secretory proteins can presumably reach these structures in COPII vesicles, and the hybrid Golgi structures show relatively normal cycling of late Golgi components, so secretory proteins can presumably depart to the cell surface in transport carriers. Compared to the unperturbed Golgi, the hybrid Golgi structures may yield altered glycosylation (Gaynor and Emr, 1997) but they are functional for membrane traffic. This analysis plausibly explains how yeast cells can continue to secrete after COPI inactivation.

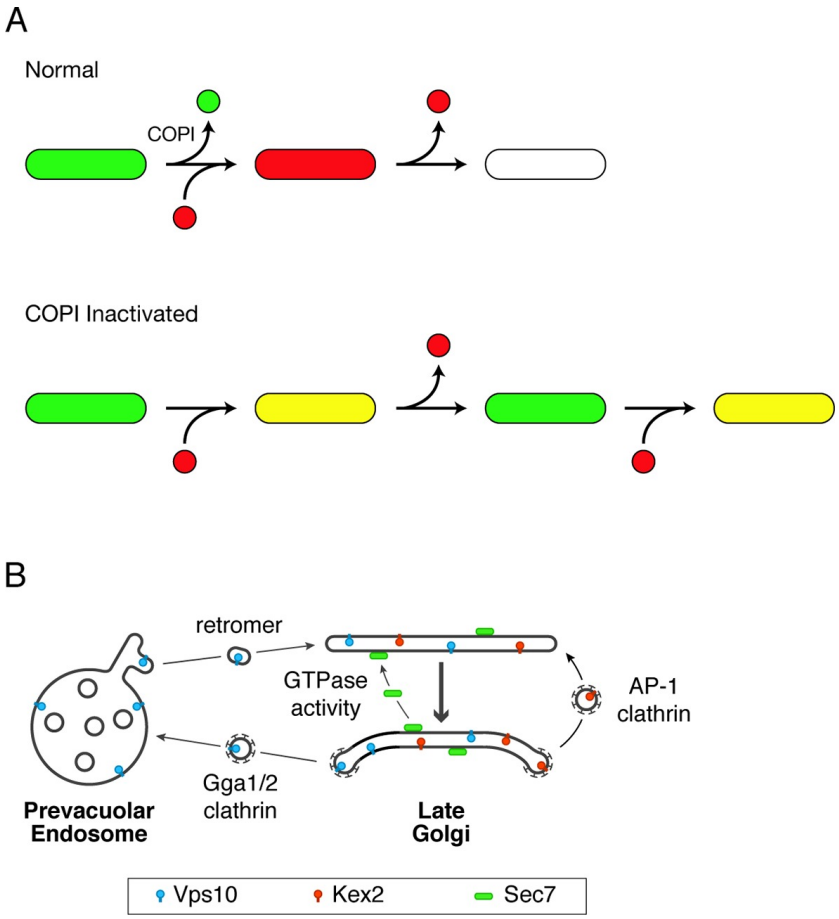

Figure 2.26: Working hypotheses for Golgi protein recycling by COPI-dependent and COPI-independent pathways. (A) The existence of multiple intra-Golgi recycling pathways can explain why inactivating COPI generates hybrid structures that repeatedly gain and lose late Golgi proteins. Green represents early Golgi proteins that recycle in COPI vesicles, and red represents late Golgi proteins that recycle by COPI-independent pathways. Under normal conditions, early Golgi proteins depart while late Golgi proteins arrive, and then late Golgi proteins depart in turn. When COPI is inactivated, the recycling of early Golgi proteins is inhibited, so when late Golgi proteins arrive, a hybrid structure is generated. This hybrid structure can subsequently lose late Golgi proteins by COPI-independent pathways, and then the process begins again. (B) During maturation of the late Golgi, proteins are likely to recycle by several pathways. The thick arrow represents cisternal maturation that occurs during and after conversion to a late Golgi compartment (Daboussi et al., 2012; Day et al., 2013). Peripheral membrane proteins such as Sec7 are recruited to late Golgi cisternae by activated GTPases, and are subsequently released from the membrane by GTP hydrolysis. Some transmembrane proteins such as Vps10 travel to the prevacuolar endosome in clathrin-coated vesicles with the aid of the Gga1 and Gga2 adaptors, and then recycle to newly formed late Golgi cisternae with the aid of cargo scaffolds such as retromer. Other transmembrane proteins such as Kex2 are postulated to recycle from older to younger late Golgi cisternae in clathrin-coated vesicles with the aid of the AP-1 adaptor.

While it is interesting to explore the effects of COPI inactivation, the larger goal is to understand the normal role of COPI in Golgi traffic. We have proposed that Golgi maturation occurs in discrete stages, and that the transition from the "carbohydrate synthesis" stage to the "carrier formation" stage involves the COPI-dependent recycling of resident Golgi proteins to younger cisternae (Day et al., 2013; Papanikou and Glick, 2014). In yeast, Vrg4 is a marker of the carbohydrate synthesis stage while Sec7 is a marker of the carrier formation stage. As a cisterna acquires Sec7, it loses Vrg4. Loss of Vrg4 probably occurs by COPI-mediated transport, based on genetic, biochemical, and electron microscopic evidence that Vrg4 is recycled in COPI vesicles (Abe et al., 2004; Mari et al., 2014). The implication is that if COPI is inactivated, a cisterna could acquire Sec7 while failing to lose Vrg4, thereby generating a hybrid compartment (Figure 2.26A).

We tested this idea by capturing 4D movies after COPI had been inactivated. As predicted, after COPI inactivation, Golgi structures acquired Sec7-DsRed while failing to lose GFP-Vrg4. This result provides the first direct evidence that COPI plays a role in cisternal maturation. Specifically, we conclude that COPI helps to drive cisternal maturation by recycling early Golgi proteins such as Vrg4 from maturing cisternae. Vrg4 could recycle to younger cisternae either by intra-Golgi traffic, or by Golgi-to-ER traffic followed by delivery to newly forming cisternae. To evaluate these possibilities, we note that when COPII was inactivated by anchoring to mitochondria, GFP-Vrg4 showed no ER accumulation of the type that would be expected if this protein frequently returned to the ER. The data therefore suggest that COPI recycles Vrg4 within the Golgi.

After a hybrid Golgi structure was generated by COPI inactivation, Sec7-DsRed frequently disappeared from the structure and subsequently reappeared. Thus, the recycling pathway for Sec7 remained functional after COPI inactivation. A likely mechanism for COPI-independent recycling of Sec7 is dissociation from the membrane of one cisterna followed by reassociation with the membrane of a younger cisterna (Figure 2.26B). Consistent with this model, Sec7 recruitment to the membrane is known to require activated GTPases, imply-

ing that GTP hydrolysis releases Sec7 into the cytosol for another round of recruitment (McDonold and Fromme, 2014).

Can late Golgi transmembrane proteins also recycle independently of COPI? Some late Golgi transmembrane proteins traffic to prevacuolar endosomes and back. An example is Vps10, which is delivered to prevacuolar endosomes in clathrin-coated vesicles with the aid of Gga adaptors (Costaguta et al., 2001; Deloche et al., 2001; Abazeed and Fuller, 2008). Recycling of Vps10 from prevacuolar endosomes to the Golgi is mediated by the retromer complex (Seaman et al., 1997; Seaman, 2005). This loop through the prevacuolar endosome is presumably independent of COPI (Figure 2.26B). Other late Golgi transmembrane proteins may recycle within the Golgi itself (Wong and Munro, 2014). Candidates for such an intra-Golgi recycling pathway include trafficking machinery proteins such as Tlg1 (Valdivia et al., 2002), phospholipid translocases such as Drs2 (Liu et al., 2008), proteins such as Chs3 and Pin2 that reside in the late Golgi before undergoing regulated export to the plasma membrane (Valdivia et al., 2002; Ritz et al., 2014; Spang, 2015), and processing proteases such as Kex2 that act on secretory cargoes (Fuller et al., 1988). These proteins are often assumed to recycle from early endosomes to the late Golgi, but we found that at least some of the yeast compartments described as early endosomes are identical to the late Golgi (Bhave et al., 2014), suggesting that the proposed early endosome-to-Golgi recycling pathway could actually be an intra-Golgi recycling pathway. This intra-Golgi recycling pathway might or might not involve COPI.

To explore this issue, we focused on Kex2, which was described together with Sec7 as one of the first known markers of the yeast Golgi (Franzusoff et al., 1991; Redding et al., 1991). By fluorescence microscopy, Kex2 and Sec7 show substantial but incomplete overlap. The existence of structures that label with either Kex2 alone or Sec7 alone can now be explained, by our work plus a recent study (McDonold and Fromme, 2014), as being due to an offset in the kinetic behaviors of these two proteins during cisternal maturation. Kex2 arrives at a Golgi cisterna ∼5-20 s before Sec7 and then departs ∼5-20 s before Sec7. Thus, Kex2

apparently recycles within the Golgi somewhat ahead of Sec7. Our interpretation argues against the view that Kex2 resembles Vps10 in cycling between the Golgi and prevacuolar endosomes (Abazeed et al., 2005; De et al., 2013). Although we occasionally see Kex2-GFP in prevacuolar endosomes, this pool is very small, probably because Kex2 trafficking to prevacuolar endosomes reflects either a secondary recycling pathway or a degradation pathway. The proposed recycling of Kex2 within the Golgi merits further exploration. Meanwhile, we found that COPI inactivation did not prevent recycling of Kex2. This result, together with the finding that COPI is concentrated at the early Golgi, suggests that intra-Golgi recycling of late Golgi transmembrane proteins is independent of COPI.

A candidate for the carriers that recycle late Golgi transmembrane proteins is clathrin-coated vesicles containing the AP-1 adaptor (Figure 2.26B). Yeast AP-1 has been implicated in the late Golgi localization of multiple proteins including Tlg1, Drs2, Chs3, and Pin2 (Valdivia et al., 2002; Foote and Nothwehr, 2006; Liu et al., 2008; Barfield et al., 2009; Myers and Payne, 2013; Ritz et al., 2014). One study provided evidence that AP-1 also plays a role in Kex2 localization (Abazeed and Fuller, 2008). Those data have been thought to reflect a recycling pathway from early endosomes, but yeast AP-1 localizes to the late Golgi (Daboussi et al., 2012), supporting the alternative view that AP-1 mediates recycling from older to younger cisternae at a late stage in Golgi maturation (Valdivia et al., 2002; Liu et al., 2008). We speculate that Kex2 recycling involves AP-1, which might act in conjunction with the co-adaptor Ent5 (Costaguta et al., 2006; Copic et al., 2007; Daboussi et al., 2012). In mammalian cells, the functions attributed to AP-1 include retrograde transport from recycling endosomes and TGN-derived transport carriers (Hirst et al., 2012; Bonifacino, 2014; Matsudaira et al., 2015), and those pathways are potentially analogous to recycling within the late Golgi of yeast.

AP-1-containing retrograde vesicles may be captured at the yeast Golgi by effectors of Ypt6, a Rab GTPase that is recruited prior to Sec7 (Suda et al., 2013). One Ypt6 effector is the GARP complex, which has been implicated in endosome-to-Golgi recycling (Bonifacino

and Hierro, 2011) but could also play a similar role in intra-Golgi recycling. Another Ypt6 effector is the Sgm1 tether (Siniossoglou and Pelham, 2001), and intriguingly, the homologous TMF tether in mammalian cells captures intra-Golgi transport carriers carrying late Golgi proteins (Wong and Munro, 2014). The roles of Ypt6 effectors and AP-1 in late Golgi recycling can be tested in yeast using approaches like the ones described here.

Our working hypothesis is that yeast Golgi maturation involves distinct pathways that act in sequence. At the early Golgi, transmembrane proteins are recycled by intra-Golgi COPI vesicles. At the late Golgi, proteins are recycled by multiple mechanisms that involve either transit through the cytosol, or traffic to prevacuolar endosomes and back, or retrograde transport from older to younger cisternae (Figure 2.26B). An open question is how these various pathways are coordinated to maintain organellar homeostasis.

When COPI is inactivated, Golgi compartmentation is lost, and when Golgi compartmentation is lost, COPI is no longer needed for secretion. We interpret these findings to mean that Golgi compartmentation and COPI-driven cisternal maturation are aspects of the same phenomenon. Although Golgi compartmentation is broadly conserved, and is thought to provide fine control of glycan assembly while keeping secretory cargoes in the organelle long enough for complete processing (Stanley, 2011; Ruiz-May et al., 2012; Day et al., 2013), some organisms such as microsporidia forgo Golgi compartmentation and rely instead on a fused Golgi network (Beznoussenko et al., 2007; Takvorian et al., 2013). Yet COPI components are present in microsporidia (Beznoussenko et al., 2007; Mowbrey and Dacks, 2009), perhaps because an efficient secretory pathway always requires Golgi-to-ER recycling, even with a non-compartmentalized Golgi. In this view, Golgi-to-ER recycling is the core function of COPI, and many eukaryotes have adapted COPI for the additional purpose of maintaining separate Golgi compartments through cisternal maturation.

Materials and Methods

Strains and plasmids

Experiments were done with derivatives of the haploid *S. cerevisiae* strain JK9-3da, which carries the mutations *leu2-3,112 ura3-52 rme1 trp1 his4* (Kunz et al., 1993). Yeast cells were grown in rich glucose medium (YPD), or in minimal glucose dropout medium (SD) (Sherman, 1991) or nonfluorescent minimal glucose dropout medium (NSD) (Bevis et al., 2002), with shaking at 200 rpm in baffled flasks. Growth media were obtained from Difco Laboratories (Detroit, MI, USA).

The *TOR1-1* mutation was introduced using the pop-in/pop-out method for gene replacement (Rothstein, 1991; Rossanese et al., 1999). To delete the FPR1 gene, the kanMX cassette was amplified with the following primers to append sequences flanking the FPR1 open reading frame: AACTCGAGTATAAGCAAAAAATCAATCAAAACAAGTAATACGTACGCTGCAGGTCGAC and TAAAAAGCAGAAAGGCGGCTCAATTGATAGTACTTTGCTTATCGATGAATTCGAGCTCG. The resulting fragment was transformed into cells, which were plated on YPD containing 250 μg/mL G418 (Sigma-Aldrich, St. Louis, MO, USA) to select for double-crossover replacement of FPR1. A similar method was used to delete the *RER1* gene by replacing it with a hygromycin resistance cassette from pAG32 (Goldstein and McCusker, 1999).

The mitochondrial matrix was labeled by transforming cells with a centromeric plasmid that drove expression from the constitutive *ADH1* promoter of a mitochondrially targeted fluorescent protein, either mCherry in the case of pHS12-mCherry (Sesaki and Jensen, 1999; Bevis and Glick, 2002), or TagBFP in the case of p416-ADH::mito-TagBFP (Murley et al., 2013), which was obtained from Laura Lackner. To create a mitochondrial anchor, the gene encoding OM45 (Yaffe et al., 1989) was inserted between the strong constitutive *TPI1* promoter and the *CYC1* terminator in a vector that was integrated at the TRP1 locus. The Sec71TMD-EGFP construct was subcloned from a plasmid provided by Ken Sato into the

integrating vector YIplac128 (Gietz and Sugino, 1988). For video microscopy, an integrating vector was used to overexpress Sec7-DsRed.M1x6 (Losev et al., 2006). All other tags were introduced by using pop-in/pop-out gene replacement to express proteins at endogenous levels, except that to boost the signal for Kex2-mCherry, a second copy of this construct was expressed from a centromeric plasmid. For GFP tagging, the variants used for gene replacement were either the monomeric mEGFP (Zacharias et al., 2002) or the monomeric superfolder msGFP (Fitzgerald and Glick, 2014). The FKBP and FRB genes were obtained from Ariad Pharmaceuticals (Cambridge, MA), and the *MBP* gene was obtained from New England Biolabs (Ipswich, MA). The mCherry gene (Shaner et al., 2004) was obtained from Roger Tsien (University of California at San Diego), and was modified at the N- and C-termini to create the mCherry2B variant used here.

DNA manipulations were simulated and recorded using SnapGene software (GSL Biotech, Chicago, IL). Annotated sequence files for 34 of the plasmids used in this study are included as a zip archive (Supplementary file 1), and can be opened with the free SnapGene Viewer (http://www.snapgene.com/products/snapgene_viewer/).

Fluorescence microscopy

To minimize the background signal for fluorescence microscopy, yeast cultures were grown in SD or NSD medium. Static images were captured with living cells that were compressed beneath a coverslip without fixation and then immediately viewed, and 4D data sets were acquired with cells attached to a concanavalin A-coated coverglass-bottom dish containing NSD medium (Losev et al., 2006). To capture static images by widefield microscopy, we used an Axioplan2 epifluorescence microscope (Zeiss, Thornwood, NY) equipped with a 1.4-NA 100x Plan Apo objective and a digital camera (Hamamatsu, Skokie, IL). To capture static images by confocal microscopy, we used either an SP5 (Leica, Buffalo Grove, IL) or an LSM 710 (Zeiss) scanning confocal microscope to collect Z-stacks, with pixel sizes of 50-60 nm and Z-step intervals of $\sim$0.3 μm. To capture 4D confocal movies with two fluorescence

channels (red and green) and a scattered light channel (blue), cells were imaged at room temperature essentially as previously described (Losev et al., 2006), except that we used an SP5 microscope with pixel sizes of 50-60 nm and Z-step intervals of 0.29 μm to collect ~20-24 optical sections every 2 s. For the strain expressing GFP-Vrg4 and Kex2-mCherry, the pixel size was increased to 80 nm, the Z-step interval was increased to 0.34 μm, and the interval between Z-stacks for rapamycin-treated cells was increased to 3 s.

Some of the static confocal images and all of the 4D confocal data were deconvolved using Huygens software (Scientific Volume Imaging, Hilversum, The Netherlands). For the strain expressing GFP-Vrg4 and Kex2-mCherry, a single pass with a 2D hybrid median filter (Hammond and Glick, 2000) was performed to smooth the data before deconvolution. Adobe Photoshop and ImageJ (http://rsbweb.nih.gov/ij/) were used to colorize and merge the images, adjust brightness, and create average projections. Correction for exponential photobleaching was performed with an ImageJ plugin (http://cmci.embl.de/downloads/bleach_corrector). Editing and quantitation of 4D data sets was performed using custom plugins for ImageJ. These plugins allowed a hyperstack to be hybrid median filtered, converted to a montage time series, edited to remove extraneous fluorescence signals, converted back to a hyperstack, and quantified to measure red and green fluorescence intensities. A zip archive Supplementary file 2 provides detailed instructions for capturing and processing 4D movies, together with our custom ImageJ plugins.

Pulse-chase analysis

Cells were grown to log phase (OD_600 = 0.5-0.8) in SD medium. Prior to labeling, the cells were collected on a bottle-top filter, washed with SD lacking methionine (SD - Met), then resuspended in SD - Met at a concentration of 5 OD_600 units/mL. The concentrated cells were incubated for 30 min. For pulse labeling, 25 μCi of TRAN^{35}S-LABEL (MP Biomedicals, Santa Ana, CA) was added per OD_600 unit of cells, and the cells were incubated for 10 min. A 30-min chase was initiated by adding a 10x solution to give a final concentration of 5 mM

unlabeled methionine plus 2 mM unlabeled cysteine. All of these manipulations were carried out with constant aeration at 30°C, except in the case of Figure 2.13, for which cells were grown at room temperature and then shifted to 37°C for the SD - Met preincubation, pulse, and chase. After the chase, cells were separated from medium by centrifugation at 5000 rpm (2300xg) in a microcentrifuge.

To analyze secreted proteins, the medium was adjusted to a final concentration of 10% trichloroacetic acid (TCA). This mixture was incubated for 5 min at 60°C. TCA-precipitated material was collected by centrifugation for 5 min at full speed (16,000xg) in a microcentrifuge, then solubilized by vigorous vortexing in 50 μL of SDS-PAGE sample buffer supplemented with 0.1 M dithiothreitol and 50 mM Na^+ PIPES, pH 7.5. The sample was incubated for 30 min at 37°C, followed by a 3-min spin at full speed in a microcentrifuge to remove insoluble material.

To analyze cellular proteins, the cell pellet was resuspended in the original volume of medium, and then TCA was added to a final concentration of 10%. This mixture was incubated for 5 min at 50°C followed by 5 min on ice. TCA-precipated material was collected by centrifugation for 5 min at 3000 rpm (1000xg) in a microcentrifuge, then resuspended in SDS-PAGE sample buffer supplemented with 0.1 M dithiothreitol and 50 mM Na^+ PIPES, pH 7.5. The sample was incubated for 30 min at 60°C, followed by a 3-min spin at full speed in a microcentrifuge to remove insoluble material.

Each gel lane was loaded with a sample of secreted or cellular proteins corresponding to 0.25 OD_600 units of cells. SDS-PAGE was performed with Mini-PROTEAN TGX Tris/glycine 4-20% gradient gels using the Precision Plus Protein Dual Color Standards molecular weight markers (Bio-Rad, Hercules, CA). Gels were dried, and radioactive signals were detected using a Storm 860 molcular Imager (Molecular Dynamics, Sunnyvale, CA).

Correlative fluorescence microscopy and electron tomography

A 100-mL culture of untreated or rapamycin-treated yeast cells was grown in SD to mid-log phase at 30°C with shaking. Cells were then concentrated by vacuum filtration using a 0.22-μm bottle-top filter (EMD Millipore, Billerica, MA). The cell paste was transferred to planchettes (Ted Pella, Redding, CA), cryo-fixed using a Bal-Tec HPM 010 high-pressure freezing machine (RMC, Tucson, AZ), and placed immediately into cryo-tubes containing a frozen cocktail of 0.1% uranyl acetate in anhydrous acetone. Samples were freeze substituted at -80°C for 48-60 hr in an EM AFS2 freeze substitution device (Leica). The temperature was then raised to -50°C and the samples were washed three times with acetone, followed by successive increasing overnight infiltrations with Lowicryl K4M resin (25, 50, 75, and 100%), followed by three incubations of 1 hr each with 100% resin. Infiltrated samples were placed in molds and polymerized with ultraviolet light at -50°C for 13 hr. To preserve fluorescence, the plastic blocks were stored at -20°C prior to sectioning. Sections of 300-1500 nm were cut with an EM UC6 ultramicrotome (Leica) and placed on 200 mesh carbon-formvar coated London-Finder copper grids (Electron Microscopy Sciences, Hatfield, PA).

For fluorescence microscopy, a grid was placed on a glass slide with the resin side up, and a 22x22 mm No. 1.5 glass coverslip with a 10-μl droplet of 500 mM Na^+-HEPES, pH 7.5 was inverted onto the grid. The coverslip was immediately sealed with wax. Imaging was performed with an LSM 710 confocal microscope. Dual-color Z-stacks were captured with a 1.4-NA 100x Plan-Apo oil objective using a pinhole of 1.2 Airy units and with voxels ranging in each dimension from 0.30 to 0.43 μm. The grid was then retrieved for analysis by electron microscopy.

For transmission electron microscopy (TEM) as well as TEM tomography and scanning transmission electron microscopy (STEM) tomography, images were collected on a Tecnai G2 F30 electron microscope (FEI, Hillsboro, OR) with a Schottky field-emission gun operating at 300 kV. Grids were prepared for either TEM or STEM tomography by floating each side of the grid for 10 min on a 10-μl drop of 15 nm colloidal gold bead solution (British BioCell

International, obtained from Ted Pella). The samples were then stained for 8-15 min with 2% uranyl acetate, and placed into a Model 2040 dual-axis tomography holder (Fischione Instruments, Export, PA). For TEM tomography, 300-400 nm sections were analyzed using Serial EM (Mastronarde, 2005) to collect digital images at 15,000x magnification with a 4K UltraScan camera (Gatan, Pleasanton, CA) as a dual-axis tilt series over a range of -60° to +60° at tilt angle increments of 1°. For STEM tomography, the imaging conditions were as follows: extraction voltage = 4250 V, gun lens = 3, condenser aperture = 50 mm, and camera length range = 200-500 mm. Images were collected using a Model 3000 annular dark field detector (Fischione) placed above the viewing screen, and a Model 805 bright- and dark-field detector (Gatan) below the viewing screen. Images were collected as a dual-axis tilt series over a range of -60° to +60° at tilt angle increments of 1° using the FEI STEM tomography software. All tomograms were reconstructed and analyzed using IMOD software (Kremer et al., 1996). The estimated resolution of the STEM tomograms is 8-12 nm (Radermacher, 1992).

Movies Associated with Chapter 2

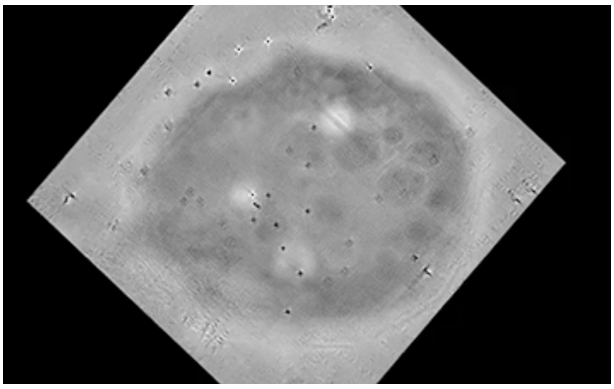

Movie 2.1: Tomographic reconstruction of Golgi cisternae in an untreated cell. Yeast cells were analyzed by STEM tomography as described in Figure 2.19. The first third of the movie shows every tenth tomographic slice. The second third of the movie shows the same tomographic slices after contours were traced to label early Golgi membranes green and late Golgi membranes red. The final third of the movie shows a rotation of the tomographic model. See also Figure 2.19A.

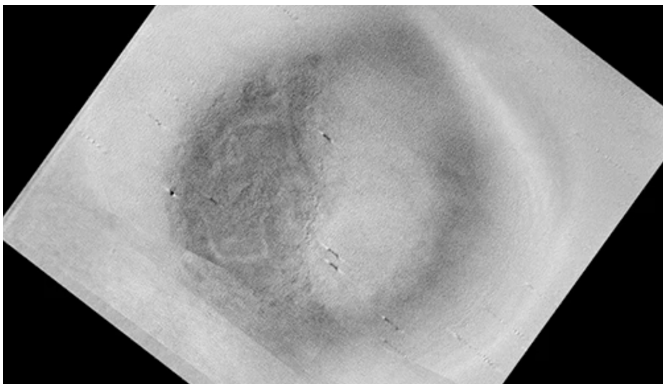

Movie 2.2: Tomographic reconstruction of hybrid Golgi structures in a cell that was treated with rapamycin to inactivate COPI. The procedure was the same as for Movie 2.1, except that COPI was inactivated prior to freezing the cells. Putative Golgi membranes are labeled yellow and mitochondrial outer membranes are labeled blue. See also Figure 2.19B.

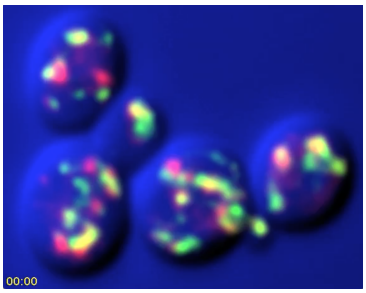

Movie 2.3: Dynamics of Vrg4 and Sec7 after anchoring COPI. Cells in which Sec21 had been anchored to mitochondria were imaged by dual-color 4D confocal microscopy to visualize the dynamics of the early Golgi marker GFP-Vrg4 and the late Golgi marker Sec7- DsRed. Scattered light images were recorded in the blue channel. Complete Z-stacks were collected every 2 s for 15 min, and the data were deconvolved, bleach corrected, and average projected. See also Figure 2.20.

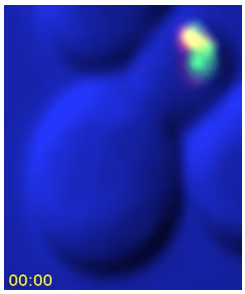

Movie 2.4: Edited movie showing Golgi Structure 1 from Movie 2.3. Movie 2.3 was cropped to include only a single budded cell. At each time point, a montage of the Z-stack was generated, and fluorescence signals were erased for all structures except the one marked with the arrowhead in Figure 2.21. This structure was designated Golgi Structure 1. An edited version of the cropped movie was then generated. See also Figure 2.20A.

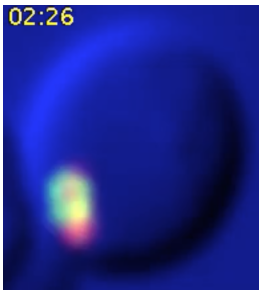

Movie 2.5: Edited movie showing Golgi Structure 2 from Movie 2.3. Movie 2.3 was cropped to include only a single cell. The procedure was the same as for Movie 2.4, except that this edited movie displays Golgi Structure 2, which is marked with an arrow in Figure 2.21. See also Figure 2.20B.

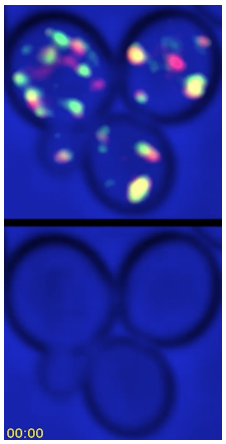

Movie 2.6: Combined original and edited movie comparing the dynamics of Kex2 and Sec7. Cells expressing Kex2-GFP and Sec7-mCherry were imaged by dual-color 4D confocal microscopy. Scattered light images were recorded in the blue channel. Complete Z-stacks were collected every 2 s for 5 min, and the data were deconvolved, bleach corrected, and average projected. Edited movies tracking two representative cisternae were generated, merged, and appended below the original movie. See also Figure 2.24A.

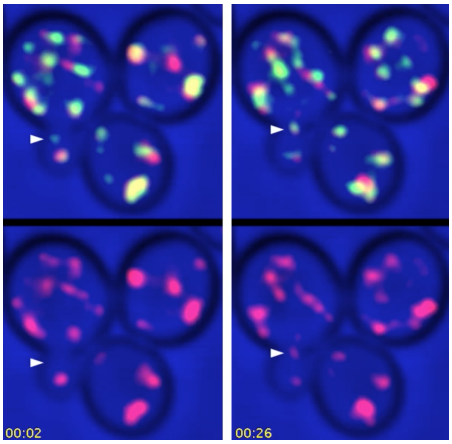

Movie 2.7: Frame pairs from Movie 2.6 showing the consistent appearance of Sec7 in Kex2-containing structures. Movie 2.6 was analyzed to identify structures that labeled for Kex2-GFP but not Sec7-mCherry, and that could be followed for at least 30 s after becoming visible. Each frame pair highlights a single Kex2-GFP- containing structure at two closely spaced time points. In the left or right half of the frame pair, the merged green and red fluorescence signals are at the top and the red fluorescence signal is at the bottom. The arrowheads in the left half of the frame pair indicate the structure prior to the appearance of Sec7-mCherry, and the arrowheads in the right half of the frame pair indicate the same structure after the appearance of Sec7-mCherry. For convenience, the 26 frame pairs corresponding to distinct Kex2-GFP-containing structures are displayed as frames in a single movie. See also Figure 2.24A and Figure 2.25.

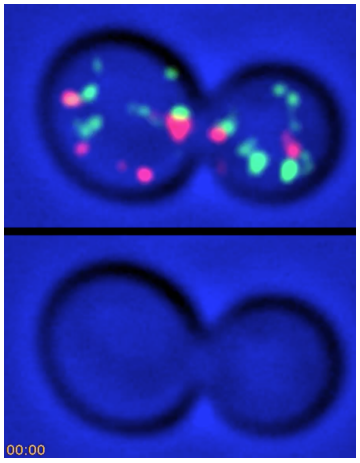

Movie 2.8: Combined original and edited movie showing the dynamics of GFP-Vrg4 and Kex2-mCherry. Cells expressing GFP-Vrg4 and Kex2-mCherry were analyzed as in Movie 2.6, except that the duration of the movie was 7 min. See also Figure 2.24B.

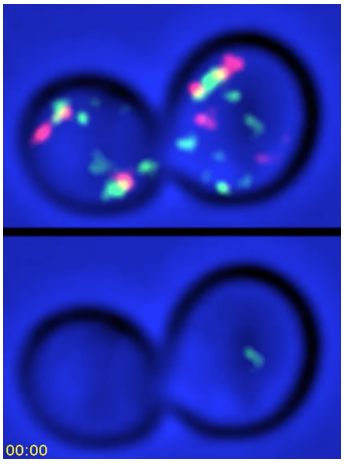

Movie 2.9: Combined original and edited movie showing the dynamics of GFP-Vrg4 and Kex2-mCherry after anchoring COPI. Cells in which Sec21 had been anchored to mitochondria were imaged as in Movie 2.7 to visualize the dynamics of GFP-Vrg4 and Kex2- mCherry, except that the duration of the movie was 10.5 min and the interval between Z-stacks was 3 s. See also Figure 2.24C.

CHAPTER 3

BUDDING YEAST HAS A MINIMAL ENDOMEMBRANE SYSTEM

Abstract

The endomembrane system consists of the secretory and endocytic pathways, which communicate by transport to and from the *trans*-Golgi network (TGN). In mammalian cells, the endocytic pathway includes early, late, and recycling endosomes. In budding yeast, different types of endosomes have been described, but the organization of the endocytic pathway has been unclear. We performed a spatial and temporal analysis of yeast endosomal markers and endocytic cargoes. Our results indicate that the yeast TGN also serves as an early and recycling endosome. In addition, as previously described, yeast contains a late or prevacuolar endosome (PVE). Endocytic cargoes localize to the TGN shortly after internalization, and manipulations that perturb export from the TGN can slow the passage of endocytic cargoes to the PVE. Yeast apparently lacks a distinct early endosome. Thus, yeast has a simple endocytic pathway that may reflect the ancestral organization of the endomembrane system.

Introduction

Organelles of the endomembrane system are linked by branched and often bidirectional trafficking routes. One major set of trafficking routes is the endocytic pathway. Endocytic compartments carry out sorting, recycling, and degradative functions (Maxfield and McGraw, 2004; Scott et al., 2014). The second major set of trafficking routes is the secretory pathway. Proteins exported from the ER transit the Golgi apparatus to the TGN, where they are sorted for delivery to the plasma membrane, to endosomes, or directly to lyso-

This chapter is a manuscript under review with the same title and the following author list: Kasey J. Day, Jason C. Casler, Benjamin S. Glick. I contributed experimental design and all data acquisition and analysis. J.C.C. contributed at an early stage of the project by developing some methods and strains. B.S.G. supervised the project and edited the manuscript.

somes/vacuoles (Gadila and Kim, 2016; Guo et al., 2014). Cargo molecules travel either by being incorporated into transport vesicles or by remaining within a compartment as it matures. Each endomembrane compartment is distinguished by a unique group of molecular markers that include Rab GTPases, cargo adaptors, vesicle coats, vesicle tethers, fusogenic SNARE proteins, and specific lipids (Cai et al., 2007; Zerial and McBride, 2001).

In mammalian cells, endocytosed material appears first in an early endosome, also known as a sorting endosome (Maxfield and McGraw, 2004). Some components are then recycled to the plasma membrane via recycling endosomes, also known as the endosomal recycling compartment. The remainder of an early endosome matures into a late endosome, also known as a multivesicular body (MVB), which delivers its contents to a lysosome for degradation (Huotari and Helenius, 2011; Rink et al., 2005). Maturation of mammalian endosomes is driven by Rab conversion, in which the early endosome marker Rab5 is replaced by the late endosome marker Rab7 (Scott et al., 2014).

Mammalian endosomes exchange material with the TGN, which is the main site of communication between the secretory and endocytic pathways (De Matteis and Luini, 2008). The TGN is often in close proximity to recycling endosomes (Misaki et al., 2007), and exchange between these compartments is bidirectional: some toxins and receptors reach the TGN via recycling endosomes (Lin et al., 2004; Matsudaira et al., 2015), while some secretory proteins travel from the TGN to recycling endosomes en route to the cell surface (Ang et al., 2004; Lock and Stow, 2005; Thuenauer et al., 2014). Similarly, exchange between the TGN and late endosomes is bidirectional: receptors carrying lysosomal hydrolases move from the TGN to late endosomes, and the empty receptors return to the TGN (Braulke and Bonifacino, 2009; Kornfeld and Mellman, 1989).

The budding yeast *Saccharomyces cerevisiae* is useful for studying endocytic vesicle formation (Goode et al., 2015), but yeast endosomes are incompletely characterized. Researchers have assumed that yeast contains early endosomes like those in mammalian cells, as well as late endosomes that deliver material to the lysosome-like vacuole (Pelham, 2002; Piper et

al., 1995). Support for this view came from biochemical and imaging data indicating that endocytosed material destined for the vacuole passes through two distinct types of endosomes (Hicke et al., 1997; Prescianotto-Baschong and Riezman, 1998; Singer-Krüger et al., 1993). Moreover, some endocytosed components can be recycled, suggesting that yeast has a compartment analogous to a recycling endosome (Lewis et al., 2000; Wiederkehr et al., 2000). The best characterized type of yeast endosome is the prevacuolar compartment, which resembles a late endosome and is often next to the vacuole (Hicke et al., 1997; Prescianotto-Baschong and Riezman, 1998). We will refer to this compartment as the prevacuolar endosome (PVE). The putative early and recycling endosomes in yeast are less well described.

A yeast early endosome could be defined functionally as the compartment in which material appears shortly after endocytosis. Yeast endocytosis is often tracked by labeling the plasma membrane with the dye FM 4-64, which is internalized to punctate structures that have been designated early endosomes (Huckaba et al., 2004; Vida and Emr, 1995). However, those results must be interpreted with caution because FM 4-64 is seen in the TGN following internalization (Lewis et al., 2000). We have shown that FM 4-64-labeled structures previously assumed to be early endosomes were actually identical to the TGN (Bhave et al., 2014).

A yeast early endosome could be defined molecularly by the presence of specific marker proteins. For example, the SNARE Tlg1 localizes to structures that were described as early endosomes based on the presence of internalized tracers (Lewis et al., 2000; Prescianotto-Baschong and Riezman, 2002). Yet Tlg1 colocalizes at least partially with TGN markers (Lewis et al., 2000; McDonold and Fromme, 2014; Valdivia et al., 2002). Similarly, the processing protease Kex2 had been assumed to cycle between endosomes and the TGN, but our recent work revealed that Kex2 actually cycles from older to younger versions of the maturing TGN (Papanikou et al., 2015). Thus, an early endosome marker that does not also label the TGN has been elusive. Many yeast researchers acknowledge this ambiguity by referring to the "TGN/early endosome." Despite this nomenclature, the prevailing notion has been

that yeast contains a distinct early endosome, which presumably matures into a PVE while exchanging material with the TGN (Arlt et al., 2015; Becuwe and Léon, 2014; Spang, 2015).

An additional question is whether yeast has recycling endosomes. A fraction of the internalized FM 4-64 recycles to the plasma membrane (Wiederkehr et al., 2000), and the SNARE Snc1 cycles through an intracellular compartment (Lewis et al., 2000). The Ypt31/32 GTPase pair and its effector Rcy1 have been implicated in recycling of Snc1 (Chen et al., 2005), but again, these proteins colocalize to a significant degree with TGN/early endosome markers (Chen et al., 2005; Jedd et al., 1997). Thus, there has been no compelling evidence for a distinct recycling endosome in yeast.

We propose that the yeast TGN also serves as an early and recycling endosome. This simple model explains many observations from the prior literature, and it is supported by the results described below. The implication is that budding yeast has a remarkably streamlined endomembrane system.

Results

Budding yeast has two types of endosomes

The starting assumption was that *S. cerevisiae* might contain early endosomes or recycling endosomes or both. To identify molecules that would label such compartments, we examined multiple protein and lipid species. Because candidate early and recycling endosome markers might localize at least partially to the TGN and/or PVE, we compared the localization of each candidate marker to two reference markers. The reference marker for the TGN was Sec7, a guanine nucleotide exchange factor (GEF) for Arf1 (Casanova, 2007; Losev et al., 2006). The reference marker for the PVE was Vps8, a subunit of the CORVET tethering complex (Arlt et al., 2015). Each candidate endosome marker was tagged with GFP and visualized together with either Sec7-mCherry or Vps8-mCherry. Tagging was done by gene replacement except in the case of Rcy1, Snc1, and Ypt52, which were expressed as GFP-tagged second copies.

We captured two-color images by confocal microscopy and measured the percent of the punctate candidate marker signal that overlapped with each reference marker. Initial controls were proteins that should localize to the TGN. Arf1 is recruited to the TGN by Sec7, and the two proteins showed strong colocalization (Figure 3.2). (Some Arf1 is also expected to be present at the early Golgi (Peyroche et al., 2001), but that pool of tagged Arf1 was relatively small.) Pik1 is a phosphatidylinositol 4-kinase that generates PI(4)P at the TGN (Hama et al., 1999; Walch-Solimena and Novick, 1999), and Pik1 as well as a GFP-tagged PH domain that binds PI(4)P colocalized strongly with the TGN reference marker (Figure 3.2) (Daboussi et al., 2012; Levine and Munro, 2001). Similarly, clathrin as well as the AP-1 and Gga clathrin adaptors are present at the TGN (Daboussi et al., 2012; Dell'Angelica et al., 2000; Myers and Payne, 2013), and the clathrin heavy chain Chc1 and the AP-1 subunit Apl2 and Gga2 all colocalized with the TGN reference marker (Figure 3.2). With our assay, typical colocalization values for proteins presumed to be at the same compartment were in the range of 60-85%.

Candidates for markers of yeast early endosomes include the SNAREs Tlg1 and Tlg2. Tlg1 was reported to colocalize with labeled endocytic tracers (Prescianotto-Baschong and Riezman, 2002), and functional and microscopy studies implicated Tlg2 in endocytosis (Abeliovich et al., 1998; Séron et al., 1998). Yet both Tlg1 and Tlg2 showed substantial colocalization with the TGN reference marker (Figures 3.1 and 3.2A).

Other markers could potentially label either early endosomes or the PVE or both. Mammalian early endosomes are defined by the presence of Rab5 (Zerial and McBride, 2001), and growing yeast cells express the Rab5 homologs Vps21 and Ypt52 (Nickerson et al., 2012; Singer-Krüger et al., 1994). However, we found that Vps21 and Ypt52 colocalized almost perfectly with the PVE reference marker (Figures 3.1 and 3.2). We also examined (a) Hse1, a subunit of the ESCRT-0 complex that initiates the formation of intraluminal vesicles in an MVB (Bilodeau et al., 2002; Henne et al., 2011); (b) Vps17, a subunit of the retromer complex that mediates retrograde traffic from endosomes to the TGN (Burd and Cullen, 2014;

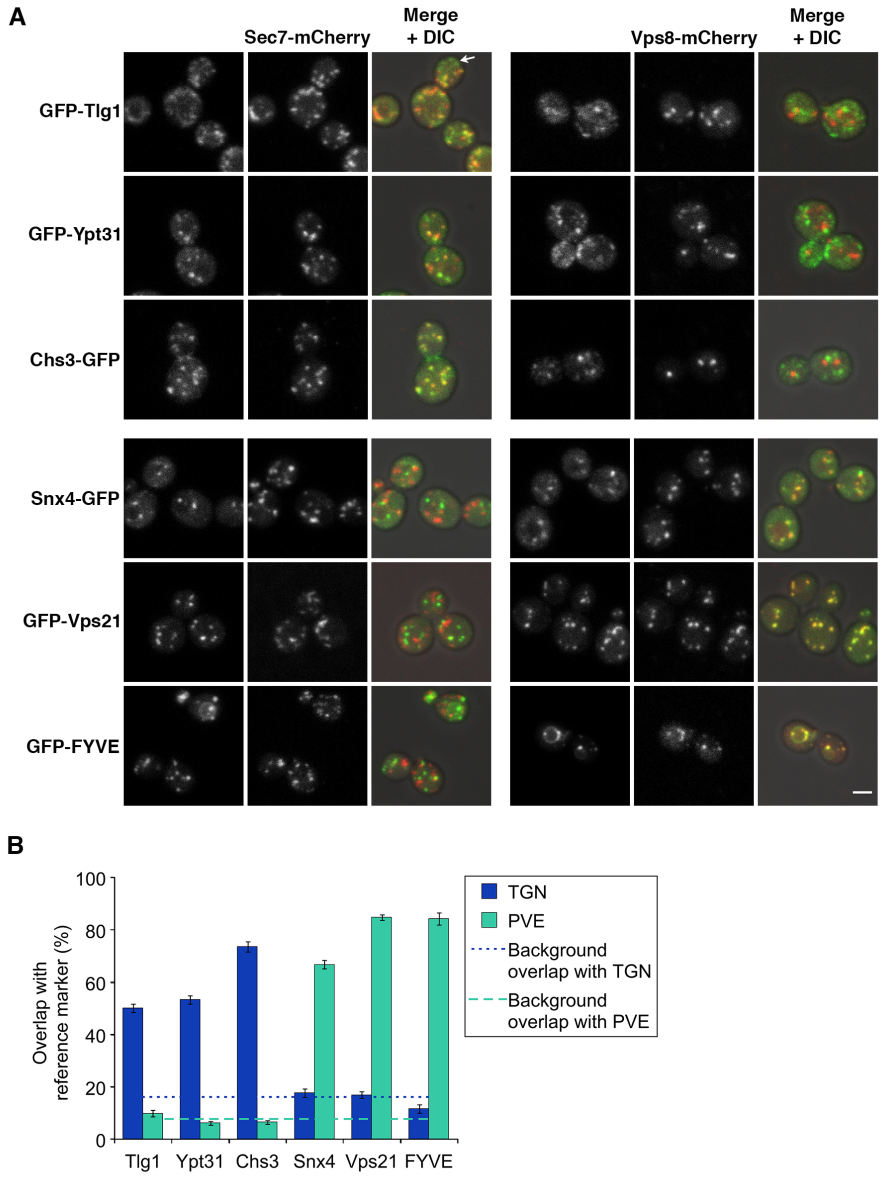

Figure 3.1: Candidate yeast endosomal markers localize to the TGN or PVE. (A) Colocalization analysis of candidate markers. Proteins were tagged with GFP and compared to mCherry-tagged reference markers by projection of confocal image stacks. Sec7-mCherry and Vps8-mCherry marked the TGN and PVE, respectively. Representative images are shown. The arrow indicates an example of Tlg1-labeled structures that did not label with the TGN reference marker. Scale bar is 2 μm. (B) Quantification of the colocalization data. Colocalization for each pair in (A) was measured as the percentage of the GFP signal that overlapped with a mask created from the mCherry signal (Levi et al., 2010; Papanikou et al., 2015). Average colocalization was calculated using at least 48 cells per strain. Error bars indicate SEM. Background colocalization values for the TGN and PVE, taken from Papanikou et al. (2015), were calculated as the percentage of each reference marker signal that overlapped by chance with the other reference marker.

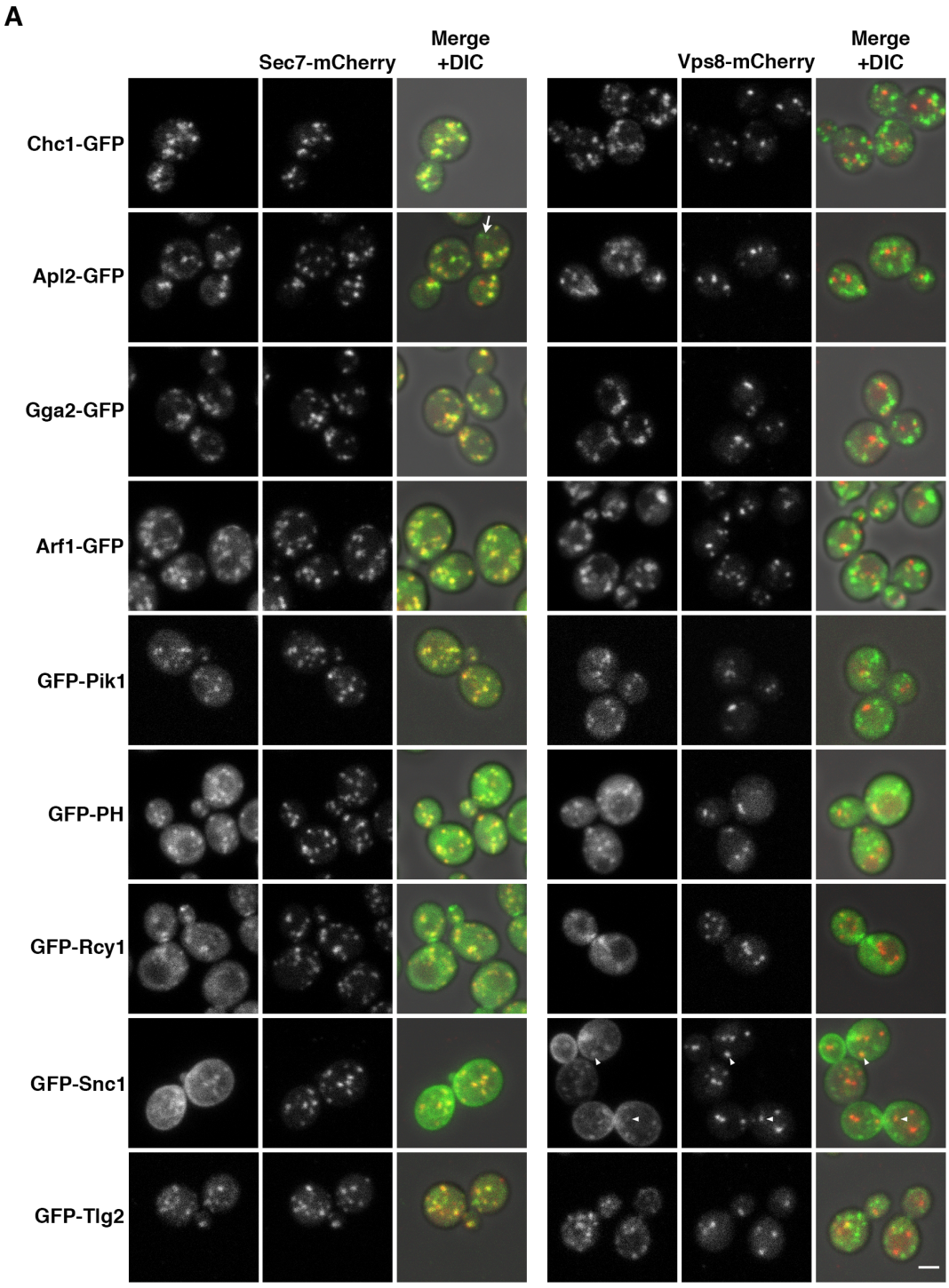

Figure 3.2: Additional markers localize to the TGN or PVE *(continued on next page)*

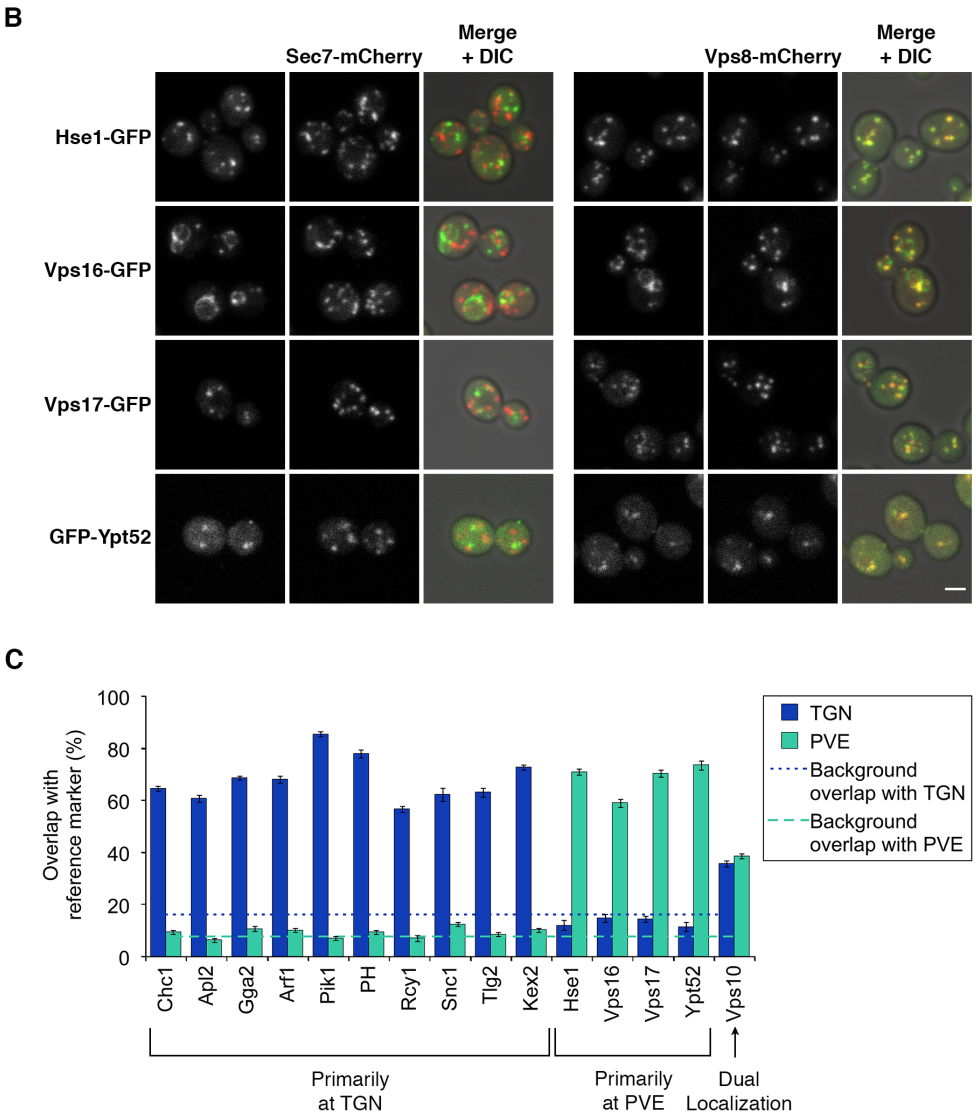

Figure 3.2: Additional markers localize to the TGN or PVE. Additional proteins were tagged and imaged as in Figure 3.1. (A) Representative images of proteins that localize primarily to the TGN as marked with Sec7-mCherry. The arrow indicates an example of Apl2-labeled structures that did not label with the TGN reference marker, and the arrowheads indicate examples of PVE-localized Snc1 signal. Scale bar is 2 μm. (B) Representative images of proteins that localize primarily to the PVE as marked with Vps8-mCherry. Scale bar is 2 μm. (C) Quantification of the colocalization data. Colocalization for each pair in (A) and (B) was measured as in Figure 3.1 using at least 40 cells per strain. Data for Kex2 and Vps10 are from Papanikou et al. (2015).

Seaman et al., 1998); (c) Snx4, a sorting nexin involved in a second endosome-to-TGN trafficking pathway (Hettema et al., 2003; Shi et al., 2011); and (d) the phosphoinositide PI(3)P, which was labeled using the FYVE domain of the mammalian early endosome marker EEA1

(Burd and Emr, 1998). Although mammalian versions of these markers are found at varying stages of the endosomal maturation pathway, Hse1, Vps17, and PI(3)P showed greater than 70% colocalization with the PVE reference marker (Figures 1 and S1). The overlap between Snx4 and the PVE reference marker Vps8 was somewhat lower because of a slight difference in shape between the two fluorescence patterns, perhaps due to the presence of Snx4 on endosomal tubules (Ma et al., 2017). Vps16, which is present in the CORVET complex with Vps8 and also in the HOPS tethering complex that acts at the vacuole (Angers and Merz, 2009; Peplowska et al., 2007), was found on the vacuolar membrane and in puncta that colocalized entirely with the PVE reference marker (Figure 3.2). An earlier paper presented evidence for slight differences in the timing of appearance of various markers at the PVE (Arlt et al., 2015), but our data do not support this interpretation. Instead, markers that would label either an early or a late endosome in mammalian cells all label the PVE in yeast.

Next, we examined markers that could potentially label a recycling endosome. The Rab GTPase Ypt31 is a yeast homolog of mammalian Rab11, which localizes to recycling endosomes (Benli et al., 1996). But Ypt31 and its close relative Ypt32 have been identified as key regulators of exit from the TGN (Jedd et al., 1997), and in agreement with previous work, we observed Ypt31 primarily at the TGN (Figure 3.1) (Kim et al., 2016; McDonold and Fromme, 2014). An effector of Ypt31/32 is the F-box protein Rcy1, which functions in endocytic recycling (Chen et al., 2005; Wiederkehr et al., 2000), and we found that overexpressed Rcy1 colocalizes with the TGN reference marker (Figure 3.2). Other potential recycling endosome markers are proteins that cycle between the plasma membrane and endocytic compartments. One such protein is the chitin synthase Chs3, which localizes to the plasma membrane or to intracellular compartments in a cell cycle-dependent manner (Santos and Snyder, 1997; Ziman et al., 1996). We found that intracellular Chs3 colocalized with the TGN reference marker (Figure 3.1), in agreement with previous reports (Zanolari et al., 2011). Another recycling protein is the SNARE protein Snc1, which is found at both the plasma membrane and endocytic compartments (Gurunathan et al., 2000; Lewis et al., 2000). With overex-

pressed Snc1, weak Snc1 signals could sometimes be detected at the PVE (arrowheads in Figure 3.2A), presumably because Snc1 cycles between the TGN and the PVE (Ma et al., 2017), but the brighter intracellular puncta corresponded to the TGN (Figure 3.2). We infer that endocytic recycling in yeast likely takes place at the TGN.

In sum, for every candidate early or recycling endosome marker that we examined, the majority of the signal colocalized with the reference marker for either the TGN or the PVE. The only exceptions were AP-3 adaptor subunits, which were found near the TGN (see below), and Vps10, a vacuolar hydrolase receptor that cycles between the TGN and PVE and localizes about equally to both compartments (Figure 3.2) (Cooper and Stevens, 1996; Papanikou et al., 2015). For yeast, neither we nor others have identified markers that might uniquely label early or recycling endosomes.

Proteins vary in their spatiotemporal patterns of association with the TGN

In many cases, a candidate endosome marker did not completely colocalize with the TGN or PVE reference marker, raising the possibility that some components have a second localization to distinct early or recycling endosomes. But alternative explanations can be envisioned. For example, with the TGN, incomplete colocalization could reflect the dynamics of maturing Golgi compartments–if the arrival and departure of a candidate marker are not synchronized with the arrival and departure of the TGN reference marker, the maturing TGN will sometimes label with only one or the other marker instead of both (Figure 3.3A). We have documented this effect for Kex2, which arrives and departs slightly before Sec7 during Golgi maturation (Papanikou et al., 2015). Thus, a full analysis of the relationship between two TGN markers requires live cell imaging.

This issue is illustrated by Tlg1. In static images, only ∼50% of the Tlg1 signal overlaps with the Sec7 signal (Figure 3.1), and some structures label with Tlg1 but not with Sec7 (arrow in Figure 3.1A). Such structures were proposed to represent early endosomes (Lewis et al., 2000). We revisited this question by comparing the dynamics of Tlg1 and Sec7 in

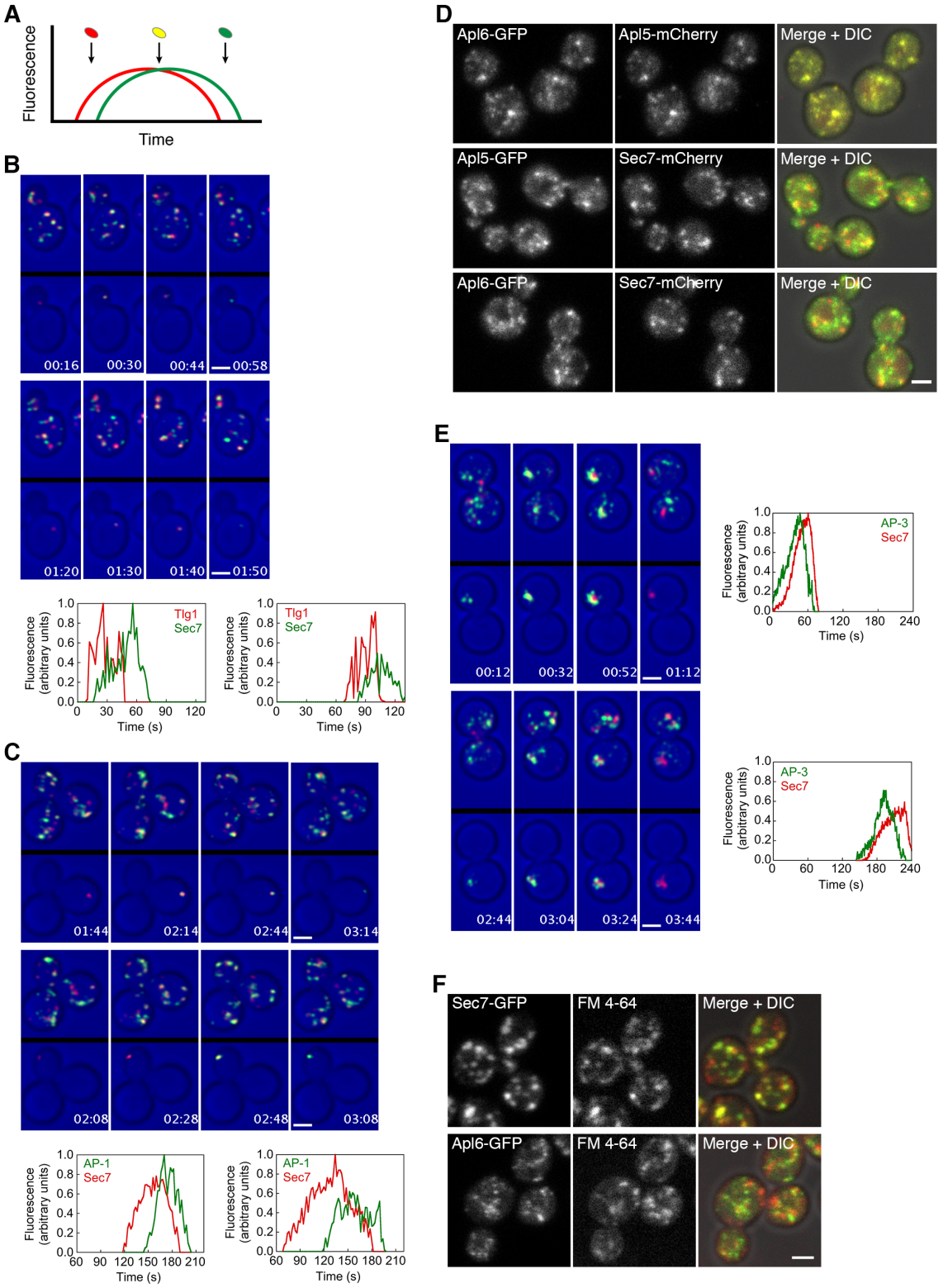

Figure 3.3: TGN markers label maturing TGN compartments *(legend on next page)*

Figure 3.3: TGN markers label maturing TGN compartments. (A) Simulated fluorescence traces for two temporally offset markers of a maturing Golgi compartment. The red marker arrives and departs before the green marker. Depending on the time when a static image is captured, the compartment may appear red, or yellow (red plus green), or only green. (B) Kinetic tracking of the SNARE Tlg1, which marks the TGN but arrives and departs before Sec7. Cells expressing Sec7-GFP and HaloTag-Tlg1 labeled with JF_{646} ligand were imaged by 4D confocal microscopy for 5 min, and the image stacks were average projected. Representative frames from Movie 3.1 are shown. In the top half of each frame, the entire projection is visible. In the bottom half, the images were edited to show only a single TGN compartment. Two representative TGN compartments were analyzed. The plots show the time-dependent fluorescence intensities for those two TGN compartments. Scale bars are 2 μm. (C) Kinetic tracking of the AP-1 adaptor, which marks the TGN but arrives and departs after Sec7. Cells expressing Sec7-mCherry and the GFP-tagged Apl2 subunit of AP-1 were imaged and analyzed as in (B). Representative frames from Movie 3.3 are shown. Scale bars are 2 μm. (D) The Apl5 and Apl6 subunits of AP-3 colocalize perfectly with each other, but colocalize only partially with the TGN reference marker Sec7. Confocal image stacks were average projected. Scale bar is 2 μm. (E) Kinetic tracking of the AP-3 adaptor. AP-3 is associated with the TGN but has a spatiotemporal pattern distinct from that of Sec7. *arf1*Δ mutant cells expressing Sec7-mCherry and Apl5-GFP were imaged and analyzed as in (B). Representative frames from Movie 3.5 are shown. Scale bars are 2 m. (F) Poor labeling of AP3 structures with internalized FM 4-64. Cells expressing Sec7-GFP or Apl6-GFP were incubated with FM 4-64 at 22°C for 30 s, and then external FM 4-64 was quenched with SCAS and the dye was chased for 4 min to label the TGN. Confocal image stacks were average projected. Scale bar is 2 μm.

4D confocal movies. Tlg1 is not abundant, so we tagged it with HaloTag and labeled the fusion protein with the bright and photostable far-red ligand JF_{646} (Grimm et al., 2015) in cells expressing Sec7-GFP. Tlg1 consistently arrived at the TGN ∼10-20 s before Sec7 and departed ∼20-30 s before Sec7 (Figure 3.3B and Movie 3.1). In a 5-min movie, a total of 32 structures that labeled with Tlg1 but not Sec7 could be followed unambiguously for at least 10 s, and each structure could be traced forward to a time point when it also contained Sec7 (first half of Movie 3.2).

The same type of analysis was performed with AP-1. Video microscopy showed previously that AP-1 is found at the TGN, where its levels peak after those of Sec7 (Daboussi et al., 2012). A somewhat different picture came from functional studies, which implicated AP-1 in the retrograde traffic of TGN proteins, leading to the idea that AP-1 acts at an endosome

to recycle proteins to the TGN (Liu et al., 2008; Spang, 2015; Valdivia et al., 2002). In our static images, the AP-1 subunit Apl2 colocalized with Sec7 ∼60% of the time (Figure 3.2), and some Apl2-labeled structures lacked Sec7 (arrow in Figure 3.2A). In movies of cells labeled with Apl2-GFP and Sec7-mCherry, Apl2 consistently arrived at the TGN ∼20-40 s after Sec7 and departed ∼10-15 s after Sec7 (Figure 3.3C and Movie 3.3). In a 5-min movie, a total of 27 structures that labeled with Apl2 but not Sec7 could be followed unambiguously for at least 10 s, and each structure could be traced back to a time point when it also contained Sec7 (second half of Movie 3.2). The implication is that both Tlg1 and AP-1 are found exclusively at the TGN, where Tlg1 arrives earlier than the TGN reference marker Sec7 while AP-1 persists somewhat longer than Sec7.

A different and unique result was seen with the AP-3 adaptor, which helps to transport certain proteins directly from the TGN to the vacuole (Cowles et al., 1997; Llinares et al., 2015) and may also play a role in yeast endocytic trafficking (Toshima et al., 2014). We examined AP-3 localization using the Apl5 and Apl6 subunits. As a control, those two subunits colocalized completely with each other (Figure 3.3D). The AP-3 subunits were often in close proximity to Sec7-labeled TGN compartments (Figure 3.3D) (Angers and Merz, 2009). However, true colocalization with Sec7 was much lower for the AP-3 subunits than for most TGN markers. To clarify the relationship between AP-3 and the TGN, we made 4D confocal movies. AP-3 proved to be highly dynamic, with the movies showing many labeled structures that changed rapidly (Movie 3.4). We simplified the analysis by deleting *ARF1* to generate fewer, larger TGN cisternae that exhibited nearly normal maturation dynamics (Bhave et al., 2014). In *arf1*Δ cells, most of the AP-3 remained close to TGN compartments, and preceded Sec7 in its arrival and departure times (Figure 3.3E and Movie 3.5). In *ARF1* wild-type cells, even though AP-3 could not be easily tracked for the lifetime of a TGN compartment, the same physical and temporal relationships between AP-3 and Sec7 were apparent (Movie 3.4). These results indicate that AP-3 associates with the maturing TGN.

The AP-3-containing structures are unusual because they are distinct from the nearby Sec7-labeled compartments in both location and shape (Figure 3.3D,E and Movie 3.5). One possibility is that AP-3 defines a TGN domain that lacks Sec7. To test this idea, we internalized FM 4-64 under conditions that label the TGN (Bhave et al., 2014), with the assumption that this bulk membrane dye should partition into all connected membrane domains. Internalized FM 4-64 colocalized very well with Sec7, but poorly with AP-3 (Figure 3.3F). These results suggest that AP-3 marks either a non-membranous structure that is attached to the TGN, or a membranous compartment that is near the TGN but not always connected to it by a phospholipid bilayer. In either case, AP-3 can be placed in the category of TGN-associated markers.

The PVE is a long-lived compartment

If yeast cells lack early endosomes, where does the PVE come from? Our results argue against the existence of a mammalian-type endosomal maturation pathway in yeast. To gain insight into the origin and fate of PVE compartments, we performed 4D confocal microscopy of cells expressing Vps8-GFP. Most of the PVE compartments could be followed for the entire duration of a 15-min movie (Figure 3.4B and Movie 3.6). PVE compartments did not disappear, as might have been expected if they fused with vacuoles. For comparison, the same cells expressed Sec7-mCherry to label the TGN. The TGN structures showed the behavior previously described for this maturing compartment (Losev et al., 2006; Matsuura-Tokita et al., 2006), with the Sec7-mCherry signal persisting for ∼70-90 s (Figure 3.4A and Movie 3.6). We also examined cells in which the PVE was labeled with both Vps8-mCherry and a second PVE marker, either GFP-FYVE or GFP-Vps21 (Movie 3.7). Those markers colocalized extensively with Vps8 and remained on Vps8-labeled PVE structures continuously. The implication is that PVE compartments are long-lived.

PVE compartments occasionally undergo fusion and fission (Arlt et al., 2015; Chi et al., 2014). These phenomena cause stepwise increases and decreases in the intensity of the

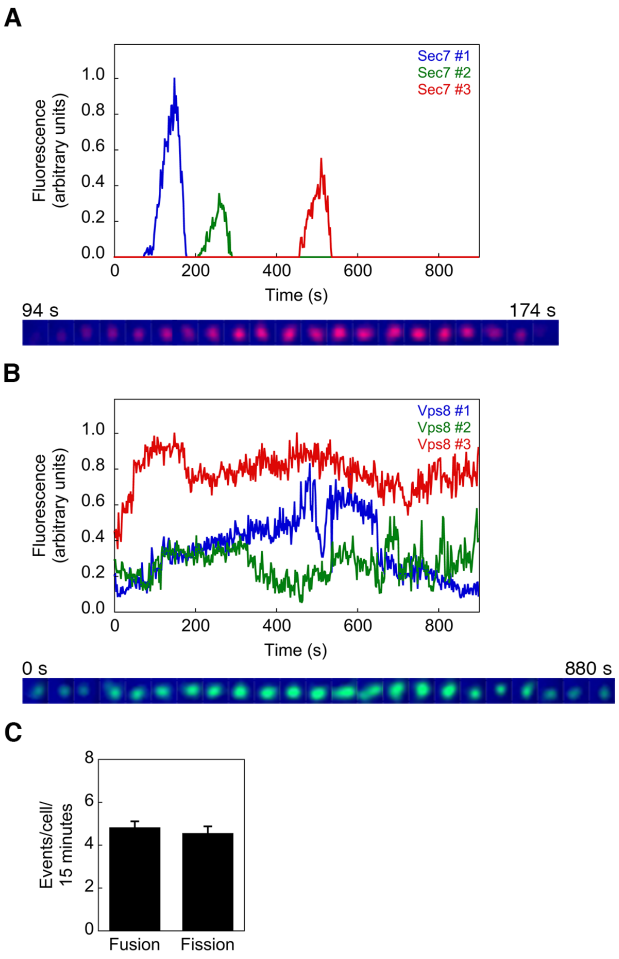

Figure 3.4: The PVE is a persistent compartment. (A) Fluorescence traces for three representative TGN compartments labeled with Sec7-mCherry. In Movie 3.6, cells expressing Sec7-mCherry and Vps8-GFP were imaged by 4D confocal microscopy for 15 min. Three TGN compartments labeled with Sec7-mCherry were tracked for as long as the fluorescence signals were visible. Shown are average projected images of Sec7 structure #1 at 4 s intervals. (B) Fluorescence traces for three representative PVE compartments labeled with Vps8-GFP. Those compartments were tracked for the duration of Movie 3.6. Shown are average-projected images of Vps8 structure #1 at 40 s intervals. (C) Fission and fusion of PVE structures. For cells expressing Vps8-GFP, five 15-min 4D confocal movies were analyzed to count the number of PVE fission and homotypic fusion events. Bars indicate the average number of events per cell with SEM.

Vps8-GFP signal, as illustrated by the blue trace in Figure 3.4B. The rates of fusion and fission were similar, with an average of 4.8 fusion events and 4.6 fission events per cell over the course of a 15-min movie (Figure 3.4C). Thus, a plausible mechanism for maintaining the number of PVE compartments per cell is a balance between fusion and fission.

The TGN is an early destination for bulk endocytosis

Because FM 4-64 is seen in the yeast TGN soon after endocytosis (Figure 3.3F) (Bhave et al., 2014), our working hypothesis was that the yeast TGN serves as an early endosome. This hypothesis predicted that internalized FM 4-64 should appear first in the TGN and then in the PVE. As a test, we generated a wave of labeled endocytic traffic by applying a 30 s pulse of FM 4-64, followed by a chase with SCAS, which quenched dye that had not been internalized (Bhave et al., 2014). The cells expressed Sec7-CFP and Vps8-YFP so that FM 4-64 could be visualized simultaneously with TGN and PVE compartments. FM 4-64 labels both the recycling and degradative branches of the endocytic pathway, with a portion of the dye molecules returning to the cell surface while the remainder ultimately reach the vacuole (Vida and Emr, 1995; Wiederkehr et al., 2000). To visualize the compartments involved, we captured static images at periodic intervals during the chase period, and then counted the number of TGN and PVE structures that contained detectable levels of FM 4-64 at each time point. FM 4-64 labeling of the TGN peaked at around 3 min after internalization (Figure 3.5A,B). Loss of FM 4-64 from the TGN was gradual despite the rapid turnover of this compartment, presumably because dye-containing membrane recycled from older to younger TGN cisternae. FM 4-64 labeling of the PVE peaked at around 10 min after internalization, then gradually decreased as the dye began to appear in the vacuolar membrane (Figure 3.5A,B). These kinetics fit with the idea that after endocytosis, the TGN is the first destination of bulk membrane, followed by the PVE and vacuole.

To test whether endocytic traffic necessarily passes through the TGN before reaching the PVE, we used a *pik1-83* mutant strain, which expresses a thermosensitive version of the Pik1 kinase that generates PI(4)P at the TGN (Audhya et al., 2000; Hendricks et al., 1999). Reduction of PI(4)P levels compromises export from the TGN (Walch-Solimena and Novick, 1999). In *pik1-83* cells at the permissive temperature of 22°C, traffic of internalized FM 4-64 to the TGN, PVE, and vacuole were essentially normal (Figure 3.5C,D). By contrast, in *pik1-83* cells at the nonpermissive temperature of 37°C, FM 4-64 rapidly reached the

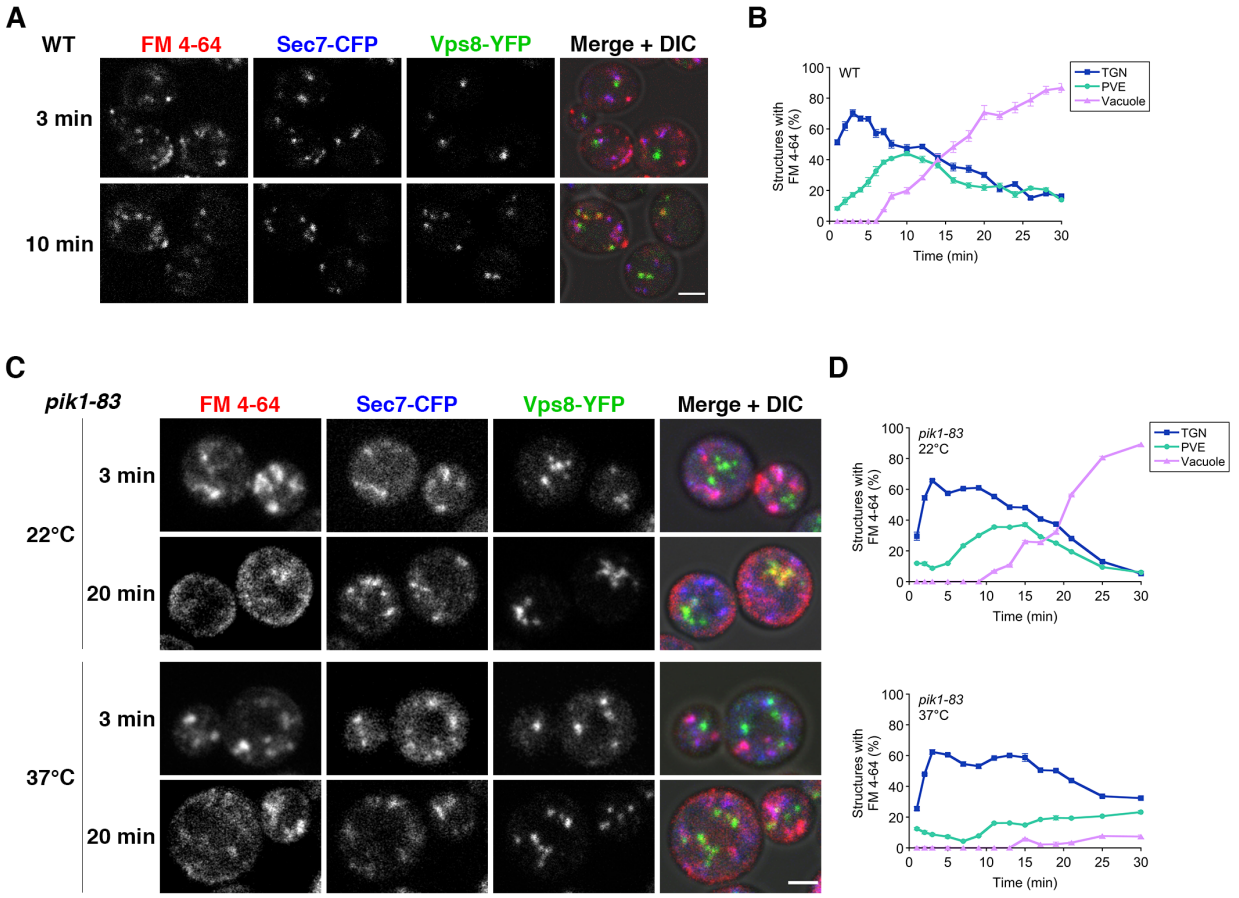

Figure 3.5: The TGN is an early destination for internalized FM 4-64. (A) Labeling of endocytic compartments with internalized FM-4-64. Wild-type ("WT") cells expressing Sec7-CFP and Vps8-YFP were incubated at 22°C with FM 4-64 for 30 s followed by SCAS. Confocal image stacks were collected at intervals up to 30 min after FM 4-64 addition. Representative average projections are shown for the 3 min and 10 min time points. Scale bar is 2 μm. (B) Quantification of the data from (A). Localization of FM 4-64 in wild-type cells was quantified as the percentage of Sec7-labeled TGN structures, Vps8-labeled PVE structures, and vacuolar structures that showed detectable FM 4-64 signal. Mean ± SEM is shown for at least 32 cells for each time point. (C) Labeling of endocytic compartments with internalized FM 4-64 in a *pik1* mutant strain. *pik1-83* cells expressing Sec7-CFP and Vps8-YFP were grown at 22°C, then half of the culture was shifted to 37°C for 15 min. Both halves of the culture were incubated with FM 4-64 for 30 s followed by SCAS. Confocal image stacks were collected at intervals up to 30 min after FM 4-64 addition. Representative average projections are shown for the 3 min and 20 min time points. Scale bar is 2 μm. (D) Quantification of the data from (C). The analysis was performed as in (B) except that widefield images were examined. Mean ± SEM is shown for at least 35 cells for each time point.

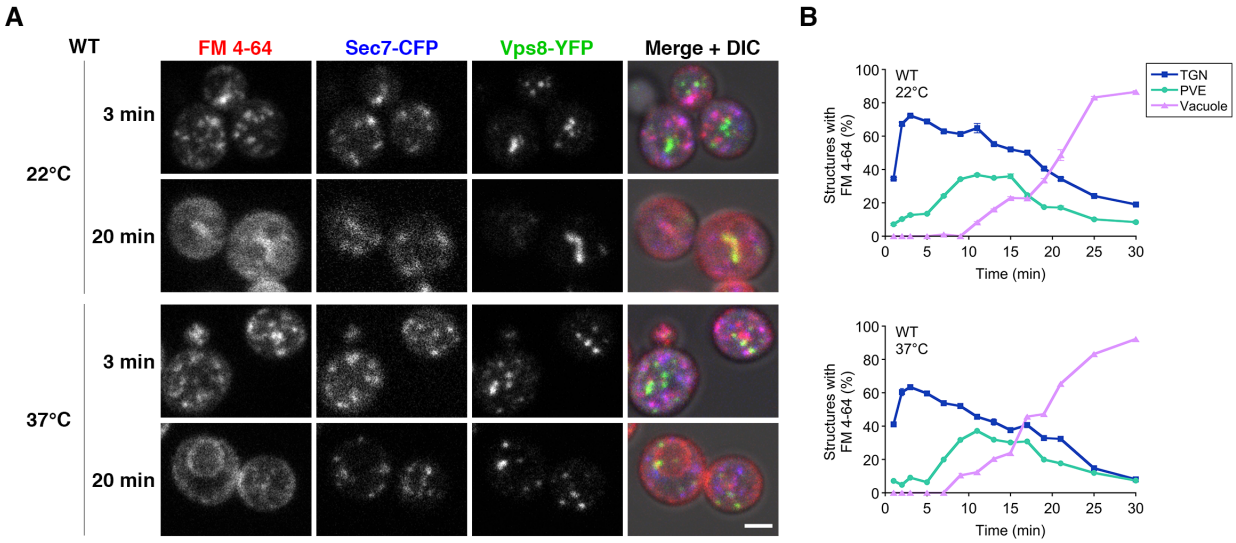

Figure 3.6: FM 4-64 travels to the PVE and vacuole normally in an isogenic *PIK1* strain. (A) Labeling of endocytic compartments with internalized FM 4-64 at different temperatures. Wild-type ("WT") cells isogenic to the *pik1-83* mutant cells were incubated at 22°C or 37°C and analyzed as in Figure 3.5. Scale bar is 2 μm. (B) Quantification of the data from (A). Mean ± SEM is shown for at least 35 cells for each time point.

TGN, but then exhibited severe delays in reaching the PVE and vacuole (Figure 3.5C,D). An isogenic wild-type *PIK1* strain showed no defect in FM 4-64 traffic at 37°C (Figure 3.6). These results match earlier reports (Audhya et al., 2000; Walch-Solimena and Novick, 1999), except that the TGN is now identified as the site of FM 4-64 accumulation in *pik1* mutant cells. Thus, most or all of the internalized membrane labeled by FM 4-64 evidently passes through the TGN en route to the PVE and vacuole.

The TGN is an early destination for signal-dependent endocytosis

Although FM 4-64 is useful for tracking initial steps of endocytosis, the internalized dye travels to multiple destinations. A simpler route is followed by the mating pheromone α-factor, which binds to the Ste2 receptor at the cell surface and then travels unidirectionally to the vacuole for degradation (Arlt et al., 2015; Toshima et al., 2006). The signal for endocytosis and vacuolar degradation is ubiquitination of Ste2 (Hicke and Riezman, 1996). To visualize this signal-dependent endocytic traffic, we accumulated Cy5-labeled α-factor at

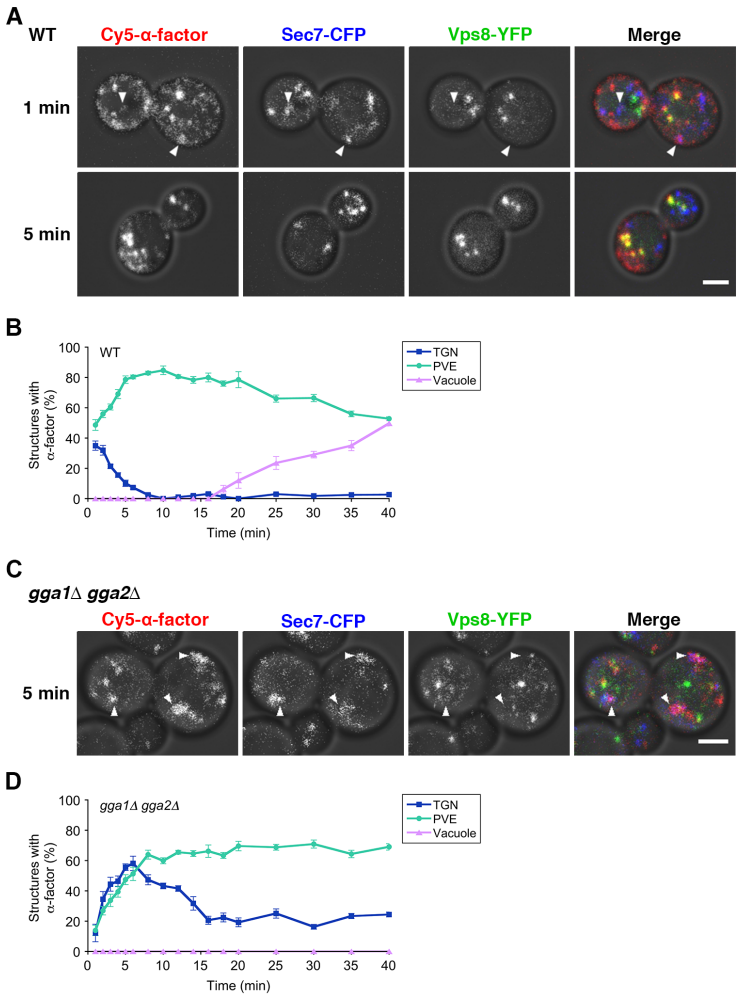

Figure 3.7: The TGN is an early destination for internalized α-factor. (A) Labeling of endocytic compartments with internalized α-factor. Cells expressing Sec7-CFP and Vps8-YFP were incubated with Cy5-conjugated α-factor for 2 h on ice, then transferred to room temperature media and fixed at intervals from 1 to 40 min after the temperature shift. Confocal image stacks were captured. Representative average projections are shown for the 1 min and 5 min time points. Arrowheads denote colocalization between Sec7-CFP and fluorescent α-factor. Scale bar is 2 μm. (B) Quantification of the data from (A). Localization of α-factor was quantified as the percentage of Sec7-labeled TGN structures, Vps8-labeled PVE structures, and vacuolar structures that showed detectable fluorescent α-factor signal. Mean $\pm$ SEM is shown for at least 20 cells for each time point. (C) Labeling of endocytic compartments with internalized α-factor in a *gga1*Δ *gga2*Δ mutant strain. *gga1*Δ *gga2*Δ cells expressing Sec7-CFP and Vps8-YFP were incubated with fluorescent α-factor and imaged as in (A). A representative average projection is shown for the 5 min time point. Arrowheads denote colocalization between Sec7-CFP and fluorescent α-factor. Scale bar is 2 μm. (D) Quantification of the data from (C). The analysis was performed as in (B). Mean $\pm$ SEM is shown for at least 20 cells for each time point.

the cell surface at low temperature, then shifted the cells to room temperature to trigger a wave of internalization (Arlt et al., 2015; Toshima et al., 2006). Internalized α-factor accumulated in the PVE (Figure 3.7A,B) as previously reported (Arlt et al., 2015). However, at the earliest time points, dim but clearly visible α-factor signals were also detected in TGN compartments (Figure 3.7A,B). Within 5 min after the temperature shift, the internalized α-factor had chased entirely to the PVE, where it remained until gradually appearing in the vacuole beginning at $\sim$18 min (Figure 3.7A,B). The early appearance of α-factor in the TGN is consistent with the possibility that Ste2-bound α-factor travels first to the TGN after endocytosis.

According to this hypothesis, after reaching the TGN, Ste2-bound α-factor is rapidly sorted into carriers and transported to the PVE. A candidate for such a sorting system at the TGN is the Gga adaptors, which recognize proteins destined for the PVE (Costaguta et al., 2001; Scott et al., 2004). We tested whether deletion of the *GGA1* and *GGA2* genes would slow export of internalized α-factor from the TGN. Indeed, in a *gga1*Δ *gga2*Δ strain, internalized α-factor remained visible in a subset of the TGN compartments for tens of minutes (Figure 3.7C,D). Turnover of TGN compartments labeled by Sec7-GFP occurred with similar kinetics in *gga1*Δ *gga2*Δ cells as in wild-type cells (data not shown) (Daboussi et al., 2012), suggesting that α-factor was retained by recycling within the maturing TGN. Compared to wild-type cells, the *gga1*Δ *gga2*Δ cells showed somewhat reduced accumulation of α-factor in the PVE and negligible appearance of α-factor in the vacuole (Figure 3.7C,D). Loss of the Gga adaptors likely has multiple effects–e.g., intraluminal vesicle formation at the PVE may be compromised, thereby blocking delivery to the vacuole (Deng et al., 2009; Lauwers et al., 2009). With this caveat, the results support the interpretation that Ste2-bound α-factor travels first to the TGN and then exits to the PVE in a process that involves the Gga adaptors. Another yeast plasma membrane protein that undergoes signal-dependent endocytosis is the methionine permease Mup1 (Menant et al., 2006). Upon addition of methionine to the media, Mup1 is ubiquitinated and internalized, then delivered

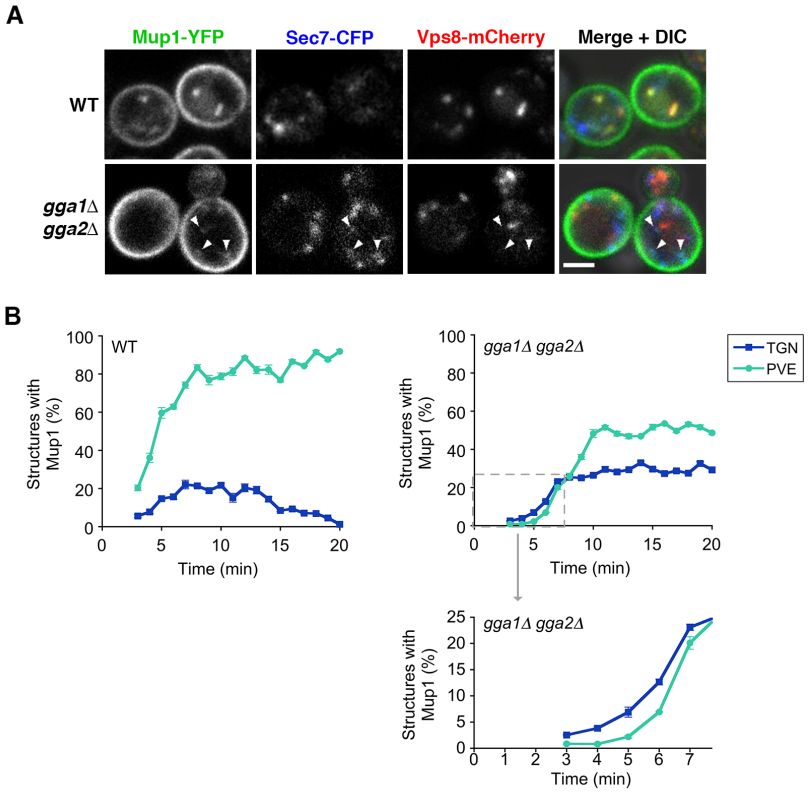

Figure 3.8: Levels of internalized Mup1 in the TGN are elevated by deletion of the Gga proteins. (A) Labeling of endocytic compartments with internalized Mup1. Strains with either *GGA1 GGA2* ("WT") or *gga1*Δ *gga2*Δ alleles and expressing Sec7-CFP, Vps8-mCherry, and Mup1-YFP were grown in media lacking methionine. After addition of methionine, cells were fixed at intervals from 3 to 20 min. Confocal image stacks were captured, avoiding the strongly labeled plasma membrane signals at the tops and bottoms of the cells. Representative average projections are shown for the 5 min time point. Arrowheads denote colocalization between Sec7-CFP and Mup1-YFP. Scale bar is 2 μm. (B) Quantification of the data from (A). Localization of Mup1 was quantified from widefield images as the percentage of Sec7-labeled TGN structures and Vps8-labeled PVE structures that showed detectable fluorescent Mup1 signal. For the *gga1*Δ *gga2*Δ data, an expanded version is provided for the early time points. Mean ± SEM is shown for at least 20 cells for each time point.

to the vacuole for degradation (Lin et al., 2008). At 5 min after methionine addition to wild-type cells, internalized Mup1 was seen in the PVE (Figure 3.8A, upper panels), where it remained visible for at least 20 min (Figure 3.8B) (Prosser et al., 2010). Very little Mup1 was detected in the TGN, with only an occasional TGN compartment having a detectable signal after methionine addition (Figure 3.8B). In a *gga1*Δ *gga2*Δ strain, at 3-5 min after methionine addition, internalized Mup1 was almost never visible in the PVE, but was some-

times visible in TGN compartments (Figure 3.8A, lower panels). Although the percentage of *gga1*Δ *gga2*Δ cells displaying internalized Mup1 was low at those early time points, the kinetic data were consistent with initial appearance in the TGN followed by delivery to the PVE (Figure 3.8B). Mup1 remained visible in the TGN of *gga1*Δ *gga2*Δ cells for at least 20 min while also progressively appearing in the PVE (Figure 3.8B). We postulate that like Ste2-bound α-factor, Mup1 passed rapidly through the TGN in a Gga-dependent manner. However, sequential appearance in the TGN and PVE was harder to detect for Mup1 than for α-factor because internalization of Mup1 was less well synchronized. The combined results with α-factor and Mup1 provide evidence that signal-dependent endocytic traffic in yeast involves passage through the TGN en route to the PVE.

Yeast endocytic vesicles fuse with the TGN

The simplest interpretation of our data is that endocytic vesicles are targeted directly to the TGN and not to the PVE. To test this hypothesis directly, we imaged endocytic vesicles containing FM 4-64 (Huckaba et al., 2004) in cells that also expressed a GFP-tagged marker for the PVE or TGN. For the PVE, the marker was Vps8-GFP. For the TGN, the choice of marker was trickier because we found that internalized FM 4-64 appeared in TGN structures ∼10 s earlier than Sec7 (Figure 3.10A and Movie 3.8). Thus, if Sec7-GFP were used to label the TGN, an endocytic vesicle might fuse with a TGN compartment that was not yet labeled. We therefore used Kex2-GFP, which arrives at the TGN 5-20 s earlier than Sec7 (Papanikou et al., 2015). Another challenge was to limit the number of endocytic vesicles containing FM 4-64 so that individual vesicles could be tracked. A typical yeast cell has ∼30 endocytic structures that persist for ∼30 s (Carlsson et al., 2002; Lu and Drubin, 2017), so approximately one endocytic vesicle forms per second. Using a custom flow chamber (Barrero et al., 2016), we exposed yeast cells to a 5 s pulse of FM 4-64 followed by a chase with SCAS to quench external dye, thereby generating about five labeled endocytic vesicles per cell. The fate of those vesicles was then followed by 4D confocal microscopy.

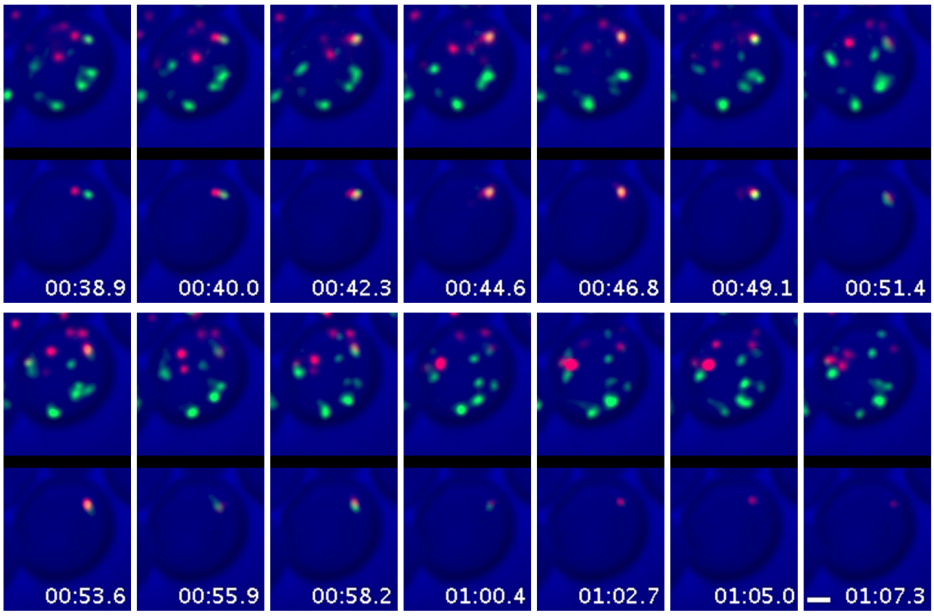

Figure 3.9: Yeast endocytic vesicles fuse with the TGN but not the PVE. A 5 s pulse of FM 4-64 followed by SCAS were applied in a flow chamber to cells expressing Kex2-GFP. The cells were then imaged by 4D confocal microscopy, and the image stacks were average projected. Selected frames show a cell from Movie 3.8, either unedited in the upper panels, or edited in the lower panels to focus on a single endocytic vesicle merging with a TGN compartment. Time is calculated from the start of the FM 4-64 pulse. Scale bar is 1 μm.

Endocytic vesicles containing FM 4-64 were frequently seen to approach and merge with TGN compartments marked with Kex2-GFP. The FM 4-64 and GFP signals could then be tracked together for multiple movie frames (Movie 3.9). Figures 3.9 and 3.10B show representative fusions of endocytic vesicles with TGN compartments. We observed 145 such merge events in movies of 33 cells. Although structures containing FM 4-64 occasionally approached PVE compartments (Movie 3.10 and Figure 3.10C), we observed no merge events in movies of 37 cells. These results confirm that the first destination in the yeast endocytic pathway is the TGN.

Discussion

Early endosomes are well characterized in mammalian cells (Figure 3.11A) and have long been thought to exist in yeast (Hicke et al., 1997; Pelham, 2002; Singer-Krüger et al., 1993;

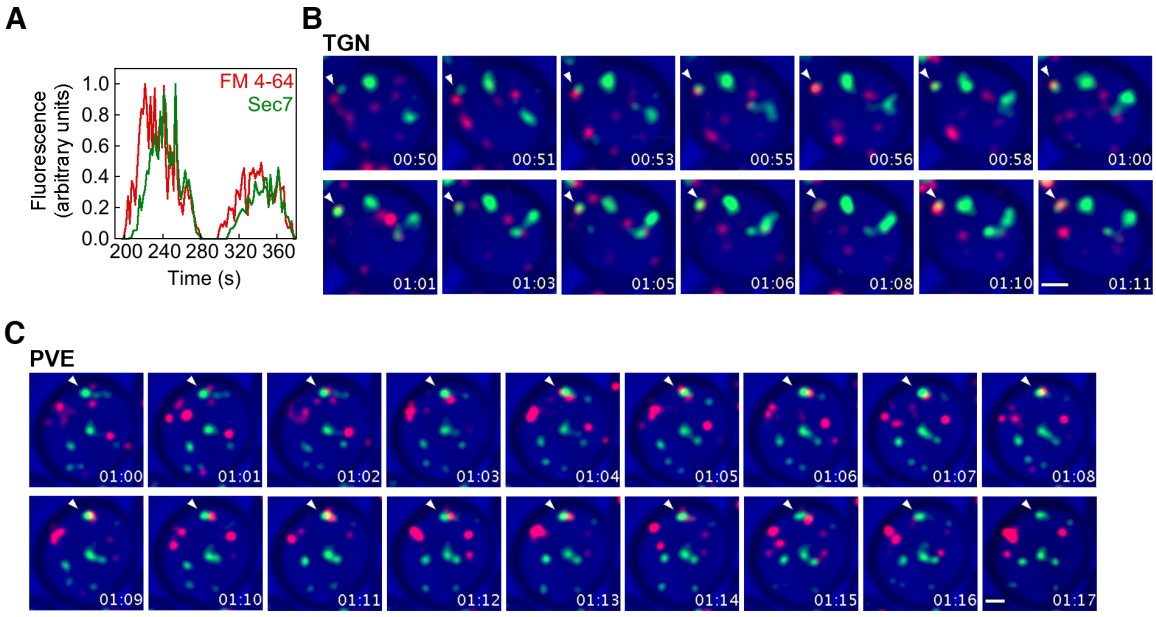

Figure 3.10: Yeast endocytic vesicles fuse with the TGN but not the PVE. (A) Arrival of FM 4-64 at an early stage of TGN maturation. Fluorescence traces from Movie 3.8 show FM 4-64 arriving at two representative TGN compartments approximately 8-10 sec before Sec7. (B) Representative example of an FM 4-64-labeled structure that merged with a TGN compartment. Cells expressing Kex2-GFP were treated and analyzed as in Figure 3.9. Arrowheads mark an FM 4-64-labeled structure that approached and then merged with a TGN compartment. The merge event suggests that the FM 4-64-labeled structure was an endocytic vesicle. Scale bar is 1 μm. (C) Representative example of an FM 4-64-labeled structure that failed to merge with a PVE structure. Cells expressing Vps8-GFP were treated and analyzed as in Figure 3.9. Arrowheads mark an FM 4-64-labeled structure that closely approached a PVE compartment, but never merged with the PVE compartment and eventually lost fluorescence. Due to the lack of a merge event, we cannot determine whether the FM 4-64-labeled structure was an endocytic vesicle or a TGN compartment. Scale bar is 1 μm.

Séron et al., 1998), yet we present evidence that *S. cerevisiae* lacks distinct early endosomes. This point is illustrated most compellingly by 4D movies of endocytic vesicles fusing with the TGN. The yeast TGN evidently functions as the first destination for both bulk endocytosis and signal-dependent endocytosis, in a pathway that has no parallel in mammalian cells. Why has the role of the TGN in yeast endocytic traffic previously been obscure? Three factors have contributed. First, yeast researchers studying the secretory and endocytic pathways have assumed that they were looking at different organelles. For example, an elegant study visualized the fusion of endocytic vesicles with "endosomal sorting compartments", which

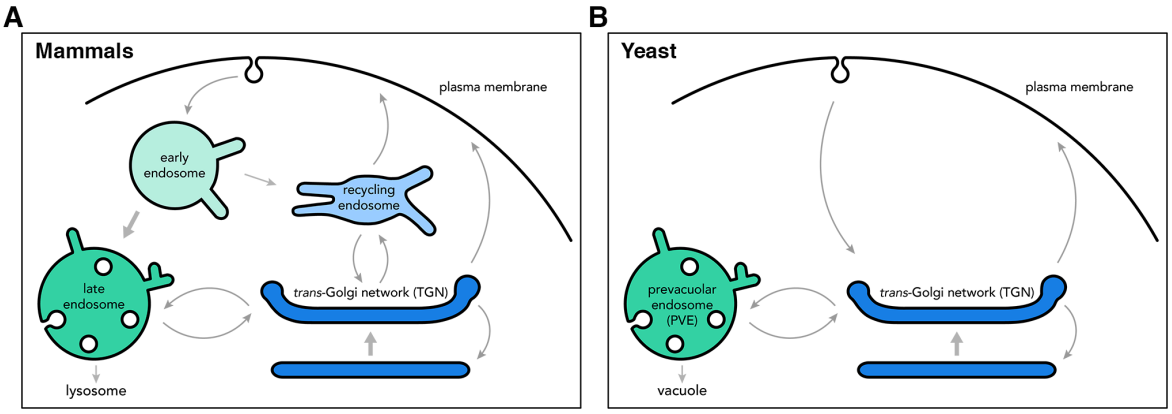

Figure 3.11: Comparison of the mammalian and yeast endocytic pathways. (A) In mammalian cells, endocytic material is delivered to early endosomes, which mature into late endosomes that subsequently fuse with lysosomes. Early endosomes also send material to recycling endosomes for return to the cell surface. Recycling endosomes are related to the TGN with regard to localization and membrane traffic machinery. Late and recycling endosomes communicate with the TGN through bidirectional traffic. (B) In yeast, endocytic material is delivered to the TGN. Internalized material is then either recycled to the cell surface, or delivered to stable PVE compartments that are postulated to undergo "kiss-and-run" events with the vacuole. Some components recycle from the PVE to the TGN. The yeast TGN can be viewed as combining properties of the mammalian TGN and recycling endosomes, and the yeast PVE can be viewed as combining properties of the mammalian early and late endosomes.

had been labeled by incubating cells with FM 4-64 and then imaging 7 min later (Huckaba et al., 2004). We find that at 7 min after FM 4-64 internalization, most of the labeled puncta are TGN compartments, suggesting that the authors were seeing fusion of endocytic vesicles with the TGN. Another example came from our analysis of effects of the *arf1*Δ mutation, which reportedly caused enlargement of Golgi cisternae and also of endocytic compartments labeled with FM 4-64 (Gaynor et al., 1998). It turned out that those endocytic compartments were identical to the TGN (Bhave et al., 2014). Thus, when endocytic markers were examined but TGN markers were not, the yeast TGN was described as an endosome.

A second factor that has obscured the role of the TGN in yeast endocytic traffic is that unlike FM 4-64, proteins with endocytic signals can pass quickly through the TGN. We obtained evidence for this phenomenon with Ste2-bound α-factor. That cargo follows a ubiquitination-dependent route through endosomes to the vacuole, but it had not previously

been detected at the TGN (Arlt et al., 2015; Toshima et al., 2014). However, a transient pool of Ste2-bound α-factor can be seen at the TGN. When we delete the Gga adaptors, which assist in transporting proteins from the TGN to the PVE (Costaguta et al., 2001; Scott et al., 2004), a substantial and persistent pool of Ste2-bound α-factor is seen at the TGN, presumably because passage to the PVE is slowed. Another yeast protein that undergoes signal-dependent endocytosis is the methionine permease Mup1 (Menant et al., 2006), and although the analysis is more challenging than for Ste2-bound α-factor, we find that deletion of the Gga adaptors increases the levels of internalized Mup1 at the TGN. Similarly, the monocarboxylate transporter Jen1 reportedly passed through the TGN on its way to the vacuole, and Jen1 accumulated in the TGN in a strain lacking the Gga adaptors (Becuwe and Léon, 2014). That study concluded that Jen1 is internalized to a maturing early endosome and then travels to the TGN and back to the PVE, but a simpler interpretation is that Jen1 is internalized directly to the TGN before reaching the PVE. The available data suggest that the initial destination for all types of yeast endocytic cargo is the TGN.

A third factor that has obscured the role of the TGN in yeast endocytic traffic is subtler. In static images, TGN proteins often colocalize only partially with one another, leading to the idea that some proteins have a dual localization to the TGN and early endosomes. But the TGN is a maturing compartment (Losev et al., 2006; Matsuura-Tokita et al., 2006), so a given TGN structure will possess different markers over time (Papanikou et al., 2015). Here we document this phenomenon with the SNARE Tlg1 and the AP-1 clathrin adaptor, which had both been implicated in recycling from endosomes but actually seem to reside exclusively at the TGN, where Tlg1 arrives and departs before Sec7 while AP-1 arrives and departs after Sec7. We conclude that when characterizing a component of the TGN, a full localization analysis requires kinetic data from live cell microscopy.

In addition to early endosomes, mammalian cells contain recycling endosomes (Figure 3.11A), so we asked whether yeast cells contain distinct recycling endosomes. Possible markers for recycling endosomes in yeast include (a) the Ypt31/32 GTPases, which are homologs

of the mammalian recycling endosome marker Rab11 (Chen et al., 2005), (b) the SNARE Snc1, which cycles between the plasma membrane and intracellular compartments (Lewis et al., 2000), and (c) Rcy1, a Ypt31/32 effector implicated in Snc1 recycling (Chen et al., 2005; Wiederkehr et al., 2000). We find that Ypt31, Snc1, and Rcy1 all localize to the TGN. Another possible marker is the chitin synthase Chs3, which cycles between the plasma membrane and intracellular "chitosomes" (Bartnicki-Garcia, 2006; Flores Martinez and Schwencke, 1988; Ziman et al., 1996). However, we see Chs3 at the TGN, and others have also concluded that chitosomes are identical to the TGN (Spang, 2015; Zanolari et al., 2011). Finally, bulk membrane recycling in the yeast endocytic pathway was previously observed using FM 4-64 (Wiederkehr et al., 2000), and our localization data suggest that this recycling step occurs at the TGN. The combined results imply that the yeast TGN is an endocytic recycling compartment. Thus, we can depict yeast as having a minimal endomembrane system, with the TGN playing a central role as a sorting station for both secretory and endocytic cargoes (Figure 3.11B).

This model raises a question about the biogenesis of PVE compartments. In mammalian cells, early endosomes mature into late endosomes, which fuse with lysosomes to deliver their contents (Bright et al., 2005; Luzio et al., 2007). By contrast, we find that PVE compartments persist for a long time and perhaps indefinitely. The only dynamic behaviors that we have observed for PVE compartments are fission and homotypic fusion. It therefore seems likely that the PVE proliferates by fission, which is presumably slightly more frequent than homotypic fusion over the course of an average cell cycle.

Our perspective on the yeast endocytic pathway sheds light on earlier observations. For example, inactivation of the TGN-localized PI 4-kinase Pik1 was reported to inhibit transport of internalized FM 4-64 to the vacuole (Audhya et al., 2000; Walch-Solimena and Novick, 1999), and deletion of the TGN-localized Gga adaptors was reported to inhibit transport of internalized plasma membrane proteins to the vacuole (Becuwe and Léon, 2014; Scott et al., 2004). Those effects could be indirect, but now that we have identified the TGN as

the first station in the yeast endocytic pathway, a more likely interpretation is that PI(4)P and the Gga adaptors have direct roles in the traffic of internalized material from the TGN. Additionally, yeast endocytic vesicles have been reported to move along actin tracks (Huckaba et al., 2004; Toshima et al., 2006), and yeast TGN compartments are associated with the actin cytoskeleton (Arai et al., 2008; Rossanese et al., 2001), providing a mechanism for efficient delivery of endocytic vesicles to the TGN. Finally, even though yeast has homologs of proteins implicated in the maturation of mammalian endosomes (Huotari and Helenius, 2011; Nordmann et al., 2010), yeast endosomes have not been seen to mature (Arlt et al., 2015), a result that can now be understood by viewing the PVE as a stable compartment.

The absence of a distinct early endosome in yeast has implications for understanding the role of AP-1. When AP-1 was first identified in mammalian cells, it was assumed to act in the forward traffic of proteins from the TGN to endosomes (Hinners and Tooze, 2003), but then the Gga adaptors were shown to mediate TGN-to-endosome traffic (Black and Pelham, 2000; Dell'Angelica et al., 2000). Meanwhile, yeast AP-1 was implicated in retrograde traffic (Liu et al., 2008; Spang, 2015; Valdivia et al., 2002), a function that is probably conserved in mammalian cells (Bonifacino, 2014; Hinners and Tooze, 2003; Matsudaira et al., 2015). Yeast AP-1 is important for maintaining the TGN localization of proteins such as Chs3 and Tlg1 (Spang, 2015; Valdivia et al., 2002). The favored hypothesis has been that AP-1 mediates recycling of TGN proteins from early endosomes to the TGN. Alternatively, it has been noted that AP-1 could mediate recycling from maturing TGN compartments (Liu et al., 2008; Valdivia et al., 2002), and our recent work favors this interpretation (Papanikou et al., 2015). Now we present evidence that yeast AP-1 resides exclusively at the TGN, strongly suggesting that AP-1 mediates intra-Golgi recycling. This idea can explain why the TGN has different types of clathrin adaptors: Gga adaptors for transport to the late endosome/PVE, and AP-1 for retrieval from older to younger TGN cisternae (Papanikou et al., 2015).

The AP-3 adaptor is more mysterious. AP-3 functions, perhaps independently of clathrin, to deliver certain proteins from the yeast TGN directly to the vacuole (Cowles et al., 1997;

Llinares et al., 2015) or from the mammalian early or recycling endosome directly to the lysosome (Peden et al., 2004; Zlatic et al., 2013). Yeast AP-3 has also been implicated in endocytosis (Toshima et al., 2014), an observation possibly related to our finding that endocytic traffic passes through the TGN. Surprisingly, we find that the physical association of yeast AP-3 with the TGN is less tight than for most TGN markers. The majority of yeast AP-3 apparently resides not on the TGN surface, but rather in unidentified structures that are somehow tethered to the TGN. The nature of this structure merits further investigation. However, we suspect that the results will not alter our view of the TGN as the nexus of the yeast secretory and endocytic pathways.

The discussion so far has emphasized differences between the endomembrane systems of yeast and mammals, but there are also fundamental similarities. It is useful to highlight the relationships of the yeast TGN and PVE compartments to the different types of mammalian endosomes (Figure 3.11).

We propose that the yeast TGN combines properties of the mammalian TGN and recycling endosomes. Interestingly, in mammalian cells, the TGN and recycling endosome are closely relatedthe recycling endosome is often near the TGN, and the two compartments share molecular markers such as Sec7 family proteins, PI(4)P, and AP-1 (Grant and Donaldson, 2009; Matsudaira et al., 2015). Moreover, some secretory cargoes pass through the mammalian recycling endosome, which can therefore be considered a post-TGN compartment of the secretory pathway (Ang et al., 2004; Lock and Stow, 2005; Thuenauer et al., 2014). It seems that yeast assigns secretion and endocytic recycling functions to the TGN, whereas mammalian cells partially segregate those functions between the TGN and recycling endosomes.

We further propose that the yeast PVE combines properties of the mammalian early and late endosomes. In agreement with earlier reports (Arlt et al., 2015; Ma et al., 2017), yeast components that might have been expected to mark separate endosome populations actually colocalize extensively at the PVE. For example, even though Rab5 is a marker for

mammalian early endosomes, we see the yeast Rab5 homologs Vps21 and Ypt52 at the PVE. The mammalian late endosome is marked by Rab7, but in yeast, the homologous Ypt7 protein is found on the vacuole (Cabrera et al., 2009). Those results are hard to reconcile with an endosomal maturation pathway of the type that operates in mammalian cells (Huotari and Helenius, 2011; Rink et al., 2005). According to that paradigm, the PVE should be a transient structure that forms by maturation and ultimately merges with the vacuole. Instead, our 4D microscopy data indicate that PVE compartments are long-lived and maintain a stable composition. We speculate that PVE compartments periodically undergo transient "kiss-and-run" events with the vacuole, thereby delivering intraluminal vesicles to the vacuole for degradation. This idea seems reasonable given that mammalian late endosomes can undergo "kiss-and-run" events with lysosomes (Bright et al., 2005). In this scenario, compared to yeast, mammalian cells do two things differently: they deliver endocytic vesicles to dedicated early endosomes instead of the TGN, and they continually regenerate endosomes through maturation and turnover.

The yeast endocytic pathway shows a striking similarity to that of plant cells, in which the TGN is also the first destination of endocytic traffic (Dettmer et al., 2006; Viotti et al., 2010). Based on this comparison, we suggest that the ancestral endomembrane system probably resembled that of yeast. The membrane traffic circuit shown in Figure 3.11B is sufficient to carry out the basic functions of the secretory and endocytic pathways, namely, sorting of biosynthetic and endocytic cargoes to either the plasma membrane or the endosome/lysosome/vacuole. According to this hypothesis, mammalian cell evolution increased the complexity of the endocytic pathway through two innovations. First, the endocytic recycling functions of the TGN were transferred to the recycling endosome, which is a derivative of the TGN. Second, endocytic vesicles were redirected from the TGN to endosomes, and the ancestral functions of a stable endosome were divided between early and late endosomes that turn over through maturation. Theoretical studies suggested that such maturation pathways evolve readily (Mani and Thattai, 2016). This analysis illustrates how comparisons of differ-

ent eukaryotes can help to distinguish between conserved and organism-specific aspects of a cell biological process.

Materials and Methods

Strains and plasmids

Yeast strains were derived from the haploid *S. cerevisiae* strain JK9-3da, which carries the mutations *leu2-3,112 ura3-52 rme1 trp1 his4* (Heitman et al., 1991). Yeast cells were grown in rich glucose medium (YPD), or in nonfluorescent minimal glucose dropout medium (NSD) (Bevis et al., 2002) in baffled flasks at room temperature.

The *ARF1* and *GGA2* genes were deleted by amplifying a kanMX cassette with primers with flanking regions corresponding to 40-42 bp upstream and downstream of the *ARF1* or *GGA2* ORF, respectively. Yeast were transformed with the amplified fragment and selected for resistance to G418 (U.S. Biological, Salem, MA). The *GGA1* gene was deleted by amplifying a hygromycin resistance cassette from pFA6-hphMX4 with primers with flanking regions corresponding to the 40 bp upstream and downstream of the *GGA2* ORF(Goldstein and McCusker, 1999). Yeast were transformed with the amplified fragment and selected for resistance to hygromycin B (Corning Life Sciences, Corning, NY).

Isogenic strains containing either the temperature-sensitive *pik1-83* or wild-type *PIK1* allele were provided by Jeremy Thorner, and the *ade2-101* allele was reverted to wild-type by transformation with a fragment corresponding to *ADE2*. GFP tags used were 1x, 3x, or 6x msGFP (Fitzgerald and Glick, 2014) and iGFP, a variant of sGFP (Losev et al., 2006) with the L221K mutation and the msGFP termini. Six tandem copies of an mCherry variant called mCherry2B, which has modified N- and C-termini, was used as a C-terminal tag for Sec7, Vps8, and Apl5. Sec7 was tagged with six tandem copies of msCFP, which was generated by Ivy Fitzgerald from SCFP3A (Kremers et al., 2006) by introducing S30R, Y39N, N105T, Y145F, I171V, L231H, and the msGFP N- and C- termini. Vps8 was tagged with six tandem copies of iYFP, which is iGFP with T65G, V68L, S72A, T203Y. Tlg1 was

N-terminally tagged with HaloTag (Promega, Madison, WI) using a yeast codon-optimized gene (GenScript, Piscataway, NJ). The iGFP-Ypt52 construct was expressed from its own promoter as an integrating second copy at the *TRP1* locus. Rcy1 and the PH domain of Osh1 were N-terminally tagged with iGFP, and the fusion genes subcloned between the *TPI1* promoter and *CYC1* terminator were integrated at the TRP1 locus. pRS406-GFP-SNC1 was provided by Nava Segev (Chen et al., 2011; Lewis et al., 2000). pRS424-GFP-FYVE(EEA1) was provided by Chris Burd (Burd and Emr, 1998). All proteins other than Ypt52, Rcy1, Snc1, Osh1(PH), and FYVE(EEA1) were tagged by gene replacement using the pop-in/pop-out method to obtain expression at endogenous levels.

Fluorescence microscopy

For fluorescence imaging, yeast cultures were grown in NSD, with amino acid dropouts when necessary, and imaged at room temperature. Static images were collected of live cells attached to a concanavalin A-coated coverglass-bottom dish containing NSD medium (Losev et al., 2006) on an SP5 or SP8 microscope (Leica, Buffalo Grove, IL) or an LSM 880 microscope (Zeiss, Thornwood, NY) equipped with a 1.4 NA/63x oil objective, using a 40-60 nm pixel size and a 0.25-0.30 μm Z-step interval and 20-30 optical sections. For quantifying the localization of FM 4-64FX (Life Technologies, Carlsbad, CA) in fixed *pik1-83* and isogenic *PIK1* cells, as well as for quantifying Mup1 localization in live cells, the cells were compressed under a coverslip and center slices were collected by widefield microscopy on an Axioplan 2 epifluorescence microscope (Zeiss) equipped with a 1.4 NA/100x oil objective and a digital camera (Hamamatsu, Skokie, IL). For quantifying α-factor localization, fixed cells were compressed under a coverslip and imaged on an LSM 880 microscope using a 50 nm pixel size and 0.30 μm Z-step interval and $\sim$10 optical sections. 4D confocal movies were collected on a Leica SP5 or SP8 microscope using an 80 nm pixel size and a 0.25-0.30 μm Z-step interval and 20-30 optical sections, with a Z-stack collected every 0.5-2.0 s.

Static images were converted to 16-bit and average projected, then range-adjusted to the minimum and maximum pixel values in ImageJ (http://rsbweb.nih.gov/ij/). To process movies, a Gaussian blur with radius 0.75 pixels was applied in ImageJ to fluorescence channels (Day et al., 2016), which were then deconvolved with Huygens Essential (Scientific Volume Imaging, Hilversum, The Netherlands) using the CMLE (Classical Maximum Likelihood Estimation) algorithm, and then corrected for bleaching using an ImageJ plugin (cmci.embl.de/downloads/bleach_corrector). Movies were converted to hyperstacks and average projected, then range-adjusted to maximize contrast in ImageJ. Custom ImageJ plugins (Papanikou et al., 2015) were used to generate montages of time series, select individual structures and remove background structures, convert edited montages to hyperstacks, and measure fluorescence intensities.

HaloTag labeling

To visualize HaloTag-Tlg1, 5 μM JF_{646} ligand, provided by Luke Lavis (Grimm et al., 2015), was added to cells from a 5 mM stock in DMSO. Cells were incubated with shaking at room temperature for 30 min, washed twice and resuspended in NSD, then adhered to a concanavalin A-coated coverglass-bottom dish. Movies were captured immediately on a Leica SP5.

FM 4-64 labeling

For the FM 4-64 time course analysis, and for comparing the localization of internalized FM 4-64 with that of AP-3, live cells were adhered to a concanavalin A-coated coverglass-bottom dish containing NSD, then 0.8 μM FM 4-64 (Life Technologies) was added from a 1 mM stock in DMSO. After 30 s, 2.4 μM SCAS (4-sulfonato calix[8]arene, sodium salt; Biotium, Hayward, CA) was added from a 1 mM aqueous stock solution to quench extracellular dye. The cells were then imaged at the times indicated. For *pik1-83* and isogenic *PIK1* cells, cultures were grown at 22°C, then split and either kept at 22°C or shifted to 37°C for 15 min

before treatment with 0.8 μM FM 4-64FX for 30 s, followed by 2.4 μM SCAS. Cultures were kept at 22°C or 37°C and samples were fixed at intervals between 1 and 30 min after addition of FM 4-64FX by combining equal volumes of yeast culture with ice-cold fixative (100 mM potassium phosphate at pH 6.5, 2 mM $MgCl_2$, 8% formaldehyde, 0.5% glutaraldehyde) while vortexing. Cells were fixed on ice for 1 hour, then washed twice with ice-cold PBS at pH 7.5 and imaged. For tracking endocytic vesicles, cells were adhered to a concanavalin A-coated coverslip and placed in a flow chamber filled with NSD (Barrero et al., 2016). Fresh NSD containing 5 μM FM 4-64 was flowed in for a 5 s pulse, followed directly by a chase with NSD containing 15 μM SCAS. Movies were then captured immediately on a Leica SP8.

α-factor labeling

Cultures were placed on ice for 15 min, then mixed with 2 μM Cy5-α-factor (ordered from Sigma-Aldrich as a custom peptide with Cy5 conjugated to the lysine side chain) from a 1 mM stock in 0.1 M sodium acetate, pH 5.2. After 2 h on ice, cells were washed in ice-cold NSD, then resuspended in room temperature NSD to initiate α-factor internalization. Samples were fixed on ice as described above at intervals up to 40 min, then washed with PBS and imaged.

Mup1 endocytosis assay

Cells grown in NSD lacking methionine (NSD-Met) were adhered to a concanavalin A-coated coverglass-bottom dish containing NSD-Met, then 20 μg/ml of methionine was added. Cells were imaged at intervals between 3 and 20 min (Prosser et al., 2010) either on a confocal microscope, or on a widefield microscope for quantitation.

Quantifying colocalization

For colocalization analysis, the fraction of the green candidate marker punctate signal that overlapped with the red reference marker punctate signal was quantified in ImageJ as follows

(Levi et al., 2010; Papanikou et al., 2015). Fluorescence channels from average projected images were converted to grayscale, noise was removed using the Smooth function, and images were inverted to generate black signal on a white background. Binary masks were created using the DynamicThreshold 1d plugin (www.gcsca.net/IJ/Dynamic.html) by taking the mean thresholded image with a mask size of 15-25 and a constant C value of 10-20 in order to detect punctate signal over varying background levels. The mask for the green channel was then subtracted from an inversion of its original grayscale image to result in an image of only the punctate green signal. The mask of the red signal was then subtracted from the image of the punctate green signal to create an image of the punctate green signal that overlapped with red signal. The mean values of the resulting image and the punctate green signal image were calculated using the Measure function, then the first was divided by the second to calculate the percentage overlap out of total punctate green signal. A modified version of this procedure was used to quantify the number of Sec7 or Vps8 structures that had detectable FM 4-64, α-factor, or Mup1 signal. Masks were created as described above for each of the three fluorescence channels. As an example, the FM 4-64 mask image was subtracted from the inverted Sec7 mask image to generate a binary image of the overlapping puncta. The number of FM 4-64 and Sec7 overlapping puncta that lacked Vps8 signal and were at least 40 nm^2 was counted using the Analyze Particles function in ImageJ, then divided by the total number of Sec7 puncta that lacked Vps8 signal, yielding the percentage of unambiguous Sec7 structures positive for FM 4-64. A similar method was used to count unambiguous Sec7 structures positive for α-factor or Mup1 as well as unambiguous Vps8 structures positive for FM 4-64, α-factor, and Mup1. Vacuole signal was calculated as the percentage of cells with FM 4-64 or α-factor visible in vacuolar structures. Each colocalization value reported is the mean ± SEM for at least the number of cells listed in the figure legend.

DNA sequences

DNA constructs were designed using SnapGene software (GSL Biotech, Chicago, IL).

Movies Associated with Chapter 3

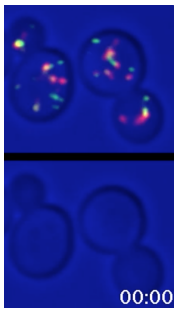

Movie 3.1: Sec7 and Tlg1 dynamics. For cells expressing Sec7-GFP and HaloTag-Tlg1 labeled with JF_{646}, confocal image stacks were collected every 2 s for 5 min. The upper panel shows average projections. The lower panel shows the same movie edited to display two representative TGN compartments.

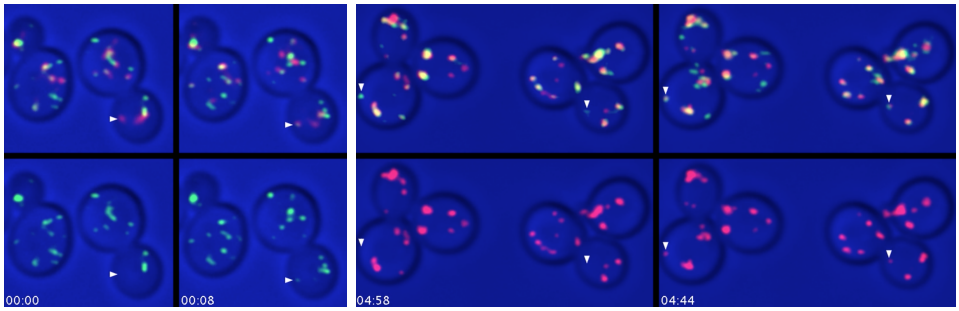

Movie 3.2: Tlg1 and AP-1 localization to maturing TGN structures. In the first set of frames, cells expressing Sec7-GFP and HaloTag-Tlg1 were analyzed in a 4D confocal movie to identify each structure that was labeled with HaloTag-Tlg1 but not with Sec7-GFP. For each such structure, later time points were then examined to determine whether the structure was subsequently labeled with Sec7-GFP. Average projections from selected time points are shown. In the lower panels, the red channel was removed for clarity. Arrowheads in the panels on the left indicate structures labeled with HaloTag-Tlg1 but not with Sec7-GFP. Arrowheads in the panels on the right indicate the same structures at later time points. In this 5-min movie, all 32 structures that were labeled exclusively with HaloTag-Tlg1 and that could be reliably tracked in time were also eventually labeled with Sec7-GFP. In the second set of frames, cells expressing Sec7-mCherry and Apl2-GFP were analyzed as in (A) to identify each structure that was labeled with Apl2-GFP but not with Sec7-mCherry. For each such structure, earlier time points were then examined to determine whether the structure was previously labeled with Sec7-mCherry. Average projections from selected time points are shown. In the lower panels, the green channel was removed for clarity. Arrowheads in the panels on the left indicate structures labeled with Apl2-GFP but not with Sec7-mCherry. Arrowheads in the panels on the right indicate the same structures at earlier time points. In this 5-min movie, all 27 structures that were labeled exclusively with Apl2-GFP and that could be reliably tracked back in time were also previously labeled with Sec7-mCherry.

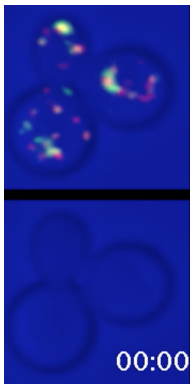

Movie 3.3: Sec7 and AP-1 dynamics. For cells expressing Sec7-mCherry and Apl2-GFP, confocal image stacks were collected every 2 s for 5 min. The upper panel shows average projections. The lower panel shows the same movie edited to display two representative TGN compartments.

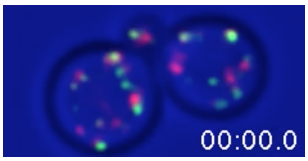

Movie 3.4: Sec7 and AP-3 dynamics in wild-type cells. For wild-type cells expressing Sec7-mCherry and Apl5-GFP, confocal image stacks were collected every 0.7 s for 5 min. Average projections are shown.

Movie 3.5: Sec7 and AP-3 dynamics in *arf1*Δ cells. For *arf1*Δ cells expressing Sec7-mCherry and Apl5-GFP, confocal image stacks were collected every 0.7 s for 5 min. The upper panel shows average projections. The lower panel shows the same movie edited to display two representative TGN compartments with associated AP-3 structures.

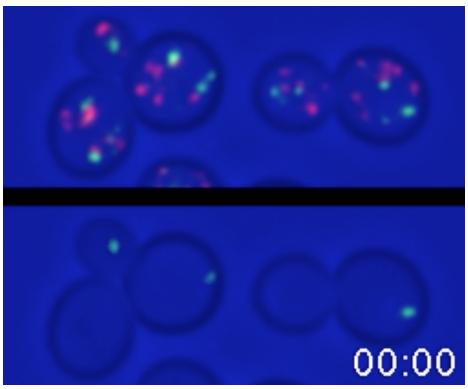

Movie 3.6: Sec7 and Vps8 dynamics. Cells expressing Sec7-mCherry and Vps8-GFP were imaged by 4D confocal microscopy for 15 min, with image stacks collected every 2 s and average projected. The upper panel shows the unedited movie. The lower panel shows the same movie edited to track three representative compartments containing Sec7 and three representative compartments containing Vps8. After fission of a Vps8-labeled compartment, the larger of the resulting structures was tracked.

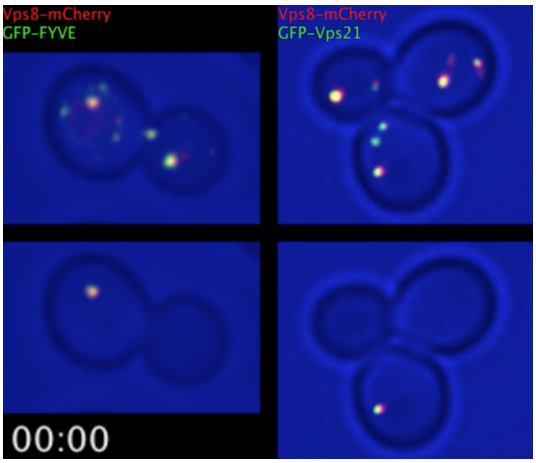

Movie 3.7: PVE marker dynamics. Cells expressing Vps8-mCherry and the PI(3)P reporter GFP-FYVE(EEA1) (left panels) or expressing Vps8-mCherry and GFP-Vps21 (right panels) were imaged as in Movie 3.6 for 12 min. The upper panels show the unedited movies. The lower panels show the same movies edited to track a representative PVE structure containing both Vps8 and PI(3)P (left) or Vps21 (right). Because the laser power for these confocal movies was very low, small PVE structures were sometimes too dim to visualize for a frame or two, resulting in occasional flickering of the red or green signal.

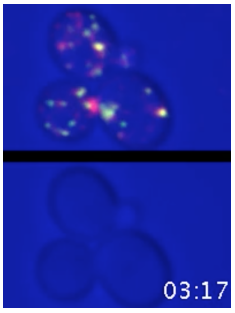

Movie 3.8: Kinetics of arrival of FM 4-64 and Sec7 at the TGN. Cells expressing Sec7-GFP were placed in a flow chamber and treated with a 30 s pulse of FM 4-64 followed by SCAS. Confocal image stacks were collected every 2 s starting about 3 min after FM 4-64 addition, and then average projected. The upper panel shows the unedited movie. The lower panel shows the same movie edited to display two representative TGN compartments, which acquired FM 4-64 and then Sec7.

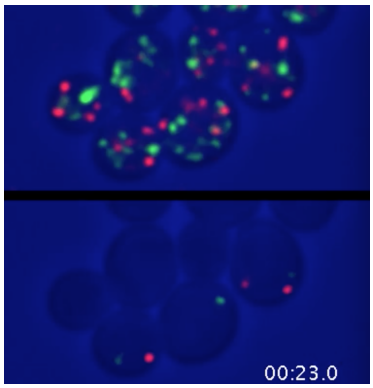

Movie 3.9: Fusion of FM 4-64-labeled structures with the TGN. Cells expressing the TGN marker Kex2-GFP were placed in a flow chamber and treated with a 5 s pulse of FM 4-64 followed by SCAS. Confocal image stacks were collected every 1.1 sec, and then average projected. The upper panel shows the unedited movie. The lower panel shows the same movie edited to display three representative examples of FM 4-64-labeled structures that merged with TGN compartments. Time is calculated from the start of the FM 4-64 pulse.

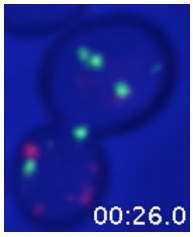

Movie 3.10: Lack of fusion of FM 4-64-labeled structures with the PVE. Cells expressing the PVE marker Vps8-GFP were treated and analyzed as in Movie 3.9. The lower panel shows a representative example of an FM 4-64-labeled structure that approached but did not merge with a PVE compartment.

CHAPTER 4

4D CONFOCAL IMAGING OF YEAST ORGANELLES

Abstract

Yeast cells are well suited to visualizing organelles by 4D confocal microscopy. Typically, one or more cellular compartments are labeled with a fluorescent protein or dye, and a stack of confocal sections spanning the entire cell volume is captured every few seconds. Under appropriate conditions, organelle dynamics can be observed for many minutes with only limited photobleaching. Images are captured at a relatively low signal-to-noise ratio and are subsequently processed to generate movies that can be analyzed and quantified. Here, we describe methods for acquiring and processing 4D data using conventional scanning confocal microscopy.

Introduction

Live-cell fluorescence microscopy provides crucial information about organelle dynamics. Ideally, an entire 3D cell volume (Z-stack) is captured at each time point, yielding a 4D data set that allows intracellular structures to be tracked for many minutes. In the case of yeast cells, 4D imaging is facilitated by the small size of the cells and the relatively low copy numbers of some compartments. A variety of methods have been described for yeast 4D imaging, including widefield microscopy with a specialized deconvolution algorithm (Arigovindan et al., 2013) and spinning-disk confocal microscopy with a custom high-sensitivity system (Kurokawa et al., 2013). Here, we describe our preferred method using conventional laser-scanning confocal microscopy. This approach uses readily available instruments and software.

The major challenge in 4D imaging is to minimize photobleaching and the accompanying photodamage to the cells. Yeast organelles are frequently tagged with fluorescent proteins

This chapter is a version of a manuscript published in a book called *The Golgi Complex: Methods and Protocols* with the same title and the following author list: Kasey J. Day, Effrosyni Papanikou, and Benjamin S. Glick. I collected and processed the movies and established reagents, methods, and parameters. E.P. helped develop imaging and processing parameters; B.S.G. supervised and edited the manuscript.

such as GFP and mCherry. These fluorophores, as well as endocytic tracers such as the dye FM 4-64 (Vida and Emr, 1995), are prone to bleaching by confocal lasers. A single Z-stack of a yeast cell typically comprises at least 20 optical slices, and a 4D movie typically involves capturing a Z-stack every few seconds for 5-15 minutes, so the total acquisition can run to thousands of individual confocal sections. Preservation of fluorescence signals under these conditions requires careful attention to multiple parameters.

To minimize photobleaching, the laser power should be as low as possible. We find that photobleaching rates are nonlinear with respect to laser intensity. During multicolor imaging, a laser used to excite one fluorophore can also bleach a second fluorophore–e.g., a 488-nm laser used to excite GFP can also bleach mCherry–so reducing the laser power can have dramatic benefits. In addition, the dwell time of the laser should be low. To meet these criteria, we use the fastest available scan rates and then perform line averaging to obtain usable signals.

Pixel size as determined by the Zoom setting is a crucial parameter. To image a fluorescent structure in a manner that avoids information loss, the sampling interval should be no higher than the Nyquist limit, which is $\sim$2.3 times smaller than the resolution of the optical system (Pawley, 2006). Yeast imaging generally employs a 1.4-NA oil immersion objective, giving a resolution on the order of 200 nm, so the pixel size should be $<$90 nm. In practice, oversampling down to a pixel size about half of the Nyquist limit tends to improve image quality, but this luxury is usually unavailable for 4D imaging. As a compromise, we use a pixel size of 65-70 nm, or $\sim$85 nm for weak fluorescence signals.

Similarly, the Z-step interval between confocal sections must be small enough to avoid information loss, but large enough to keep photobleaching low and to enable rapid acquisition of a Z-stack. We use a Z-step interval of $\sim$0.25 μm, or $\sim$0.35 μm for weak fluorescence signals. Enough confocal sections should be used to ensure that fluorescent structures throughout the cell volume will be fully captured, even if the sample shows drift along the Z-axis during movie acquisition. We usually collect 20-30 optical slices per Z-stack.

The signal-to-noise ratio for fluorescent organelles can be enhanced in several ways. A simple tactic is to overexpress the tagged protein of interest. This approach is sometimes unavoidable, in which case control experiments can be performed to confirm that overexpression has not substantially changed the biological system (Losev et al., 2006). Whenever possible, a protein should be expressed at endogenous levels by adding a tag through gene replacement at the chromosomal locus. For both overexpression and endogenous gene tagging, we routinely use cassettes encoding 3x or 6x tandem copies of a fluorescent protein (Genové et al., 2005). The fluorescence signal scales with the copy number of the fluorescent protein (Connerly et al., 2005). In addition, we minimize the background noise from the cell by using completely nonfluorescent minimal media devoid of riboflavin and folic acid (Bevis and Glick, 2002).

Even when the fluorescence signal is strong and clean as viewed by widefield microscopy, the confocal sections captured under conditions suitable for 4D imaging can look alarmingly noisy. The number of photons per pixel is usually very low, so labeled structures may not look smooth and may be embedded in a background that includes shot noise. It is important to accept relatively noisy images at the collection stage with the expectation that the noise can be reduced through image processing. A simple way to reduce shot noise and smooth the true signal is with a 3x3 hybrid median filter, which can be applied once or iteratively (Hammond and Glick, 2000). A more sophisticated approach is deconvolution with commercial software. Standard deconvolution methods are not ideal for noisy fluorescence images and may erase weak signals (Arigovindan et al., 2013). Until better deconvolution methods become available, we recommend that if the signal-to-noise ratio is low, the data should be pre-processed with a hybrid median filter before deconvolution. In general, empirical testing is needed to devise an image processing routine that adequately preserves the desired signal while removing most of the noise.

After filtering and/or deconvolution, it may be useful to correct for photobleaching. For most fluorophores, the bleaching rate approximates an exponential decay, and a 4D data

set can be corrected for exponential photobleaching using an ImageJ plugin. This correction makes it easier to view and quantify the final movies. However, the information content of the Z-stacks diminishes with photobleaching, so if the photobleaching is severe at later time points, little or no signal will be recovered. Reducing the laser power may be beneficial because even though the early images will be of somewhat lower quality, the usable signal will persist for significantly longer.

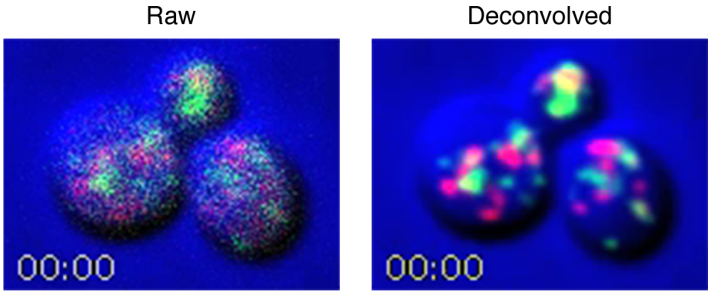

Figure 4.1: Illustration of the effect of image processing on 4D movies. Shown are the first frames from Movies 4.1 and 4.2, which are 4D movies from the same data set before and after deconvolution, respectively. Yeast cells expressing GFP-Vrg4 as an early Golgi marker and Sec7-DsRed as a late Golgi marker were imaged by con- focal microscopy, with cell images in the blue channel. Z-stacks of 24 optical sections each were collected every 2 s. Where indicated, the red and green channels were deconvolved. The movie frames are average projections of the Z-stacks. In the deconvolved movie, maturation events can be observed when green Golgi cisternae turn red (Losev et al., 2006).

A 4D movie can be viewed using a volume renderer such as the commercial Imaris or Volocity software, but a simpler and often sufficient alternative is to project each Z-stack to create a 2D image. The projections can then be assembled into a movie. Although maximum intensity projections are often used for convenience, they exaggerate weakly labeled structures, so average projections are preferable for quantitation (Hammond and Glick, 2000). A disadvantage of projections is that structures located at different depths in the cell volume may appear to be close together or merged. To address this issue, a labeled structure of interest can be tracked in the original 4D data set, and an edited movie can be generated by manually erasing the other fluorescence signals and projecting only the signal from the

labeled structure (Losev et al., 2006; Papanikou et al., 2015). Such edited movies are ideal for quantifying the dynamics of individual labeled organelles.

As an example, Fig. 4.1 shows the first frames from Movie 4.1 and Movie 4.2, which are 4D confocal movies of a yeast strain expressing a GFP-tagged early Golgi protein and a DsRed-tagged late Golgi protein (Losev et al., 2006). These markers gave relatively strong signals. In the left panel of Fig. 4.1 and in Movie 4.1, the raw data were average projected to illustrate the noise level in the images. In the right panel of Fig. 4.1 and in Movie 4.2, the deconvolved data were average projected to illustrate how noisy images can be processed to obtain usable movies.

Instrumentation and Software

1. Microscope: Leica SP5 or comparable laser scanning confocal microscope with inverted optics, a fast scanner, and high sensitivity detectors.

2. Objective lens: Plan-Apo 100x or 63x lens with an NA of 1.4 or greater. The magnification is less important than the NA and lens quality.

3. Lasers: Multiple laser lines, minimally including a 488-nm laser for exciting green fluorophores and a 561-nm laser for exciting red fluorophores.

4. Stage adaptor: Standard adaptor for holding dishes with coverglass bottoms.

5. Z-step motor: Piezoelectric stepper motor for rapid and accurate collection of Z-stacks.

6. Image manipulation and analysis software: ImageJ freeware obtained from http://imagej.nih.gov/ij/. Custom ImageJ plugins for 4D data analysis can be found in the supplemental material for a recent paper (Papanikou et al., 2015), and an ImageJ plugin that corrects for photobleaching can be obtained from http://cmci.embl.de/downloads/bleach_corrector.

7. Deconvolution software: Huygens Essential (Scientific Volume Imaging).

8. Movie processing software: QuickTime Player 7 (Apple).

Materials

1. Confocal imaging is performed with yeast strains that have been either engineered to express one or more fluorescently tagged marker proteins, or incubated with a fluorescent tracer dye. For expressing tagged proteins, we typically modify the endogenous chromosomal copy of a gene by clean gene replacement using the pop-in/pop-out method (Rossanese et al., 1999; Rothstein, 1991). If desired, a tagged gene can be overexpressed by integrating a vector containing a strong promoter (Losev et al., 2006). These approaches have the advantage that the cells do not carry free plasmids, so the expression level within the culture is uniform and the strain is stable even when grown in nonselective medium. However, in some cases it is useful to express a tagged gene on a centromeric plasmid, because cell-to-cell variability in expression enables the choice of cells with an appropriate level of fluorescence.

2. Yeast cells are grown with shaking in baffled flasks either in SD dropout medium consisting of 0.67% yeast nitrogen base with ammonium sulfate, 2% glucose, and CSM complete supplement mixture or dropout mixture (Sunrise Science Products), or in a nonfluorescent SD medium (NSD) in which the yeast nitrogen base is replaced with a mixture of salts and vitamins lacking riboflavin and folic acid (see Note 1). For a strain that does not require selection to maintain a plasmid, a preculture is grown in rich YPD medium (1% yeast extract, 2% peptone, 2% glucose) and stored at 4°C, and this preculture is used to inoculate a culture in SD or NSD medium at a dilution of 1:1000 to 1:5000 for overnight growth to logarithmic phase (optical density at 600 nm of about 0.4 to 0.8).

3. Coverglass-bottom dishes with No. 1.5 thickness are obtained from Bioptechs or MatTek, optimally with high tolerance glass of 170 $\pm$ 5 μm.

4. Concanavalin A (Sigma-Aldrich) is dissolved in water to 2 mg/mL, and stored in 0.5-mL aliquots at -80°C.

Methods

I. Preparing the Cells

1. Grow one or more yeast strains overnight to logarithmic phase in 5 mL NSD medium in a 50-mL baffled flask.

2. Prepare a coverglass bottom dish: pipet 250 μL concanavalin A onto the dish, wait 15 min, wash thoroughly with ddH_2O, and let dry.

3. Just before imaging, adhere cells to the dish: pipet 250 μL from the culture onto the dish, wait 10 min, and rinse gently several times with NSD by pipetting. Leave 2-3 mL of fresh NSD in the dish.

4. If treatment with a drug or dye is required, replace the NSD with fresh medium containing the drug or dye. If appropriate, remove the medium and replace it with fresh medium before imaging.

II. Confocal Imaging

1. Configure the microscope to use a 100x or 63x high-NA oil immersion lens. Ensure that the DIC prism is not in the light path, or the fluorescence images will be sheared and distorted. In the case of a 100x objective with a Leica STED system, the quarter wave plate should be in place or the red and green signals will be offset along the Z-axis.

2. Set the frame size to approximately 256x128 (see Note 2).

3. Set the Zoom to a level that will give a pixel size of 65-70 nm, or up to ~85 nm if the signal is weak.

4. Set the scanner to operate at maximum speed. Use bidirectional mode, as long as the brightfield image confirms that the images from the two directions can be accurately aligned.

5. Set the pinhole to 1.2 Airy units (see Note 3).

6. Set the line averaging at 4 to 8 (see Note 4).

7. Choose a Z-step size of $\sim$0.25 μm, or up to $\sim$0.35 μm if the signal is weak. Note the directionality of Z-stack acquisition (toward or away from the coverslip). To avoid confusion, be consistent with this setting between movies.

8. Set an appropriate time interval between Z-stacks. An interval of 2 s is typically suitable, but shorter intervals may be needed to track very dynamic compartments, and somewhat longer intervals may be preferable if the signal is weak.

9. Set the lasers to the lowest levels that will generate workable signals (3-10% on the SP5) (see Note 5). For fluorescence data, use the highest sensitivity detectors (HyD on the SP5). For brightfield data, a less sensitive detector is adequate (PMT on the SP5). Set the detector gains to appropriate levels (400-500 for the HyD and 300-350 for the PMT on the SP5).

10. Choose emission windows that will maximize the information collected while minimizing bleedthrough between channels. For visualization of GFP that is excited with a 488-nm laser, the emission window is 495-550 nm, and for visualization of mCherry that is excited with a 561-nm laser, the emission window is 575-750 nm (see Note 6).

11. Store each confocal section as an 8-bit RGB image, with the brightfield view of the cells stored in the blue channel.

III. Filtering

For weak signals, deconvolution often erases the structures of interest, leading to flickering movies that are impossible to analyze. In this case, it may help considerably to pre-process the data with a hybrid median filter followed by a Gaussian blur.

1. In ImageJ, open the 4D data file as a TIFF hyperstack. Then use Image → Color → Split Channels to separate the channels. With the custom plugin called "Filter Hybrid Median", filter the individual optical slices in the fluorescence channels using a single iteration of the 3D hybrid median filter. If this filter removes too much information, try a single iteration of the standard 2D hybrid median filter (see Note 7).

2. After hybrid median filtering, use Process → Filters → Gaussian Blur to do a 2D Gaussian blur with a 1-pixel radius for the optical slices in the fluorescence channels. Then use Image → Color → Merge Channels to merge the channels once again into a hyperstack.

IV. Deconvolution and Bleach Correction

Although the relatively large pixels and Z-steps used for 4D imaging are not optimal for deconvolution, this processing method is useful for cleaning up noisy images and generating smooth objects that are suitable for downstream analysis. We use the Huygens algorithm, but other deconvolution algorithms should give similar results. As described above, when the signal is weak, the Huygens software may erase a structure unless the data are pre-processed by filtering. This effect can reportedly be attributed to the mathematical form of the deconvolution algorithm, which is not ideal for noisy fluorescence data (Arigovindan et al., 2013).

1. If the 4D data file was produced directly by the confocal microscope software, the Huygens interface should provide an option for reading the imaging parameters directly.

Alternatively, if the 4D data set was pre-processed in ImageJ to generate a TIFF file, these parameters will need to be entered manually.

2. Deconvolve the fluorescence channels but not the brightfield channel, ensuring that the deconvolution software has the correct setting for the directionality of Z-stack acquisition. The refractive index of the embedding medium, which is a yeast cell, can be estimated as 1.35-1.40. A signal-to-noise ratio of 10 is usually appropriate. Other parameters such as background subtraction can be varied in empirical tests until the output appears to be an accurate rendering of the original fluorescence signals.

3. Save the output from the deconvolution as an 8-bit TIFF image sequence.

4. In ImageJ, choose File → Import → Image Sequence to convert the image sequence to a stack. Then choose Image → Hyperstacks → Stack to Hyperstack, select order "xyzct", and input the appropriate number of channels, slices per stack, and frames.

5. To correct for photobleaching (see Note 8), first use Image → Color → Split Channels to separate the channels. For each of the fluorescence channels, use Plugins → EMBLtools → Bleach Correction, and choose "Exponential Fit (Frame-wise)". Make sure the plot shows a good curve fit, then close the plot window and log window and original channel window, leaving the new corrected channel window. Finally, use Image → Color → Merge channels to regenerate a hyperstack with the bleach-corrected fluorescence data.

V. Editing 4D Data Sets with Custom ImageJ Plugins

These procedures are used when the goal is to create an edited 4D data set that includes only one or a few structures. The edited data set can be analyzed to quantify the time course of the fluorescence signals.

1. Examine a projected movie that was generated as described in Section *VI* from a non-edited 4D data set. Identify candidate structures that can potentially be tracked for

an extended period without interference from other nearby structures, keeping in mind that the 4D data set may permit resolution of structures that occasionally overlap in a projection.

2. Identify the 8-bit TIFF hyperstack that was used to generate the non-edited projected movie. With the custom plugin called "Make Montage Series", open this hyperstack, scale the images, and create the montage series.

3. With the custom plugin called "Edit Montage Series", choose a single structure that will be tracked through part or all of the movie. Delete the fluorescence signals for all of the other structures at each time point.

4. With the custom plugin called "Montage Series to Hyperstack", generate a hyperstack for the edited 4D data set. The images in this hyperstack will normally be magnified due to scaling that occurred during creation of the montage series.

5. With the custom plugin called "Analyze Edited Movie", open the hyperstack for the edited 4D data set and specify the time interval between Z-stacks. The "Red" and "Green" columns in the output file represent the total fluorescence signals from the structure of interest at each time point. Save this file, and open it in Microsoft Excel or another data analysis program to plot the fluorescence signals as a function of time.

VI. Processing 4D Data Sets for Presentation

After performing any or all of the filtering, deconvolution, bleach correction, and editing steps, a 4D data set needs to be converted from a hyperstack to a form that is suitable for presentation and publication.

1. The first step is to convert the data to 16-bit, to prevent information loss during the subsequent average projection. In ImageJ, choose Image → Color → Split Channels. For each of the resulting three windows, choose Image → Type → 16-bit. Then choose

Image → Color → Merge Channels to restore the hyperstack. Finally, choose Process → Math → Multiply, and use a multiplication factor of 256 (see Note 9).

2. If desired, merge the fluorescence from two 4D movies using the custom ImageJ plugin called "Merge Two Hyperstacks". This plugin allows two edited 4D movies to be merged, or alternatively allows one 4D movie to be placed above the othere.g., an original movie above the corresponding edited movie.

3. The next step is to create an average projection. In ImageJ, choose Image → Stacks → Z Project. If desired, select a subset of each Z-stack by choosing the Start and Stop slices. Choose the "Average Intensity" option.

4. Adjust the brightness and contrast of the individual channels as follows. Choose Image → Adjust → Brightness/Contrast. For each channel, press the "Auto" button. These settings can be fine tuned using the sliders or the "Set" button.

5. To add a time stamp, use Image → Stacks → Label. Use the format 00:00, with the appropriate time interval in seconds. To place the label in the lower left corner, set the Y location to be 1 less than the Y value of the lowest row of pixels in the image.

6. The final step is to make a movie. In ImageJ, choose File → Save As → AVI. Choose PNG compression. A frame rate of 10 fps is generally suitable. If desired, open the resulting AVI file with QuickTime Player 7 and then export a MOV file, which will often have a much smaller file size with no loss of image quality.

Notes

1. Nonfluorescent glucose medium (NSD) can be made by assembling the components of normal SD medium except for riboflavin and folic acid. To make 100 mL of a 500x vitamin stock solution, add 100 mg calcium pantothenate, 500 mg myo-inositol, 20 mg niacin, 10 mg p-aminobenzoic acid, 20 mg pyridoxine hydrochloride, 20 mg

thiamine hydrochloride, and 20 mg biotin. To make 1 liter of NSD, add 20 g glucose, 5 g ammonium sulfate, 5 g potassium phosphate monobasic, 1 g magnesium sulfate heptahydrate, 0.5 g sodium chloride, and 0.1 g calcium chloride dihydrate. Add 2 mL of the vitamin stock solution, which is stored at 4°C. Add YNB trace elements (ANACHEM) from a concentrated stock solution, which is stored at 4°C. If desired, add a CSM complete supplement mixture or dropout mixture. Adjust the pH to 5.5 with NaOH.

2. Frame height is the main determinant of the total scan time. If desired, a wider frame can be used to capture more data.

3. The typical recommendation is to use 1.0 Airy unit. However, that setting assumes optimal conditions with no refractive index mismatch between the sample and the oil/glass, whereas the actual refractive index of the cell is lower than that of the oil/glass. Empirically, we find that increasing the pinhole to 1.2 Airy units results in the capture of significantly more light with a negligible decrease in resolution.

4. Fast scans with line averaging tend to cause less photobleaching than slower scans without line averaging. Image quality is dramatically improved by line averaging, but at the expense of increasing the acquisition time. A line averaging setting of 4-8 is typically a good compromise.

5. Each laser should be used at a power that yields a decent signal while keeping the photobleaching rate acceptably low. During collection, the signal often is barely visible and is accompanied by significant noise, but such data sets can be processed to obtain usable movies. Set the laser power to 5% or even lower if possible. Photobleaching increases nonlinearly with laser intensity, so a reduction in laser power may yield a signal that is weaker at first but persists for much longer.

6. Ensure that the confocal microscope is configured with notch filters to suppress background signals from the excitation lasers.

7. Hybrid median filters work optimally when the image collection settings are near the Nyquist limit. For imaging with a high-NA objective, the pixel size should be in the range of 60-90 nm and the Z-stack interval should be in the range of 0.2-0.4 μm. Filtering before deconvolution is not generally encouraged by makers of deconvolution software because it alters the characteristics of the data, but empirically, this approach sometimes improves the movies by preserving biologically meaningful signals.

8. Unless the signal is quite strong, photobleaching is usually significant. The correction procedure involves fitting the signal intensity decay to an exponential curve and then multiplying each Z-stack by an appropriate factor to compensate. This procedure is effective up to a point, but as the original signal becomes fainter, the weaker signals in the data set will be progressively lost and will not be recovered after the correction for photobleaching.

9. After conversion to 16-bit and multiplication by 256, the image display may not be scaled appropriately, but the data are still suitable for further processing.

Movies Associated with Chapter 4

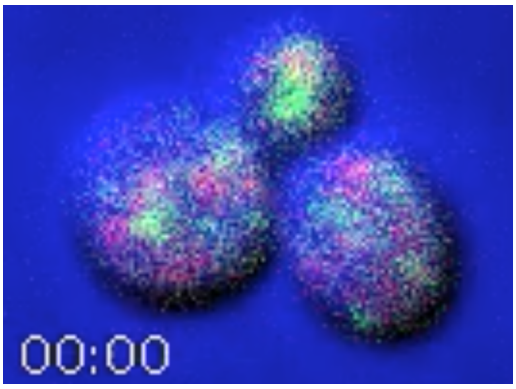

Movie 4.1: 4D movie before deconvolution. Yeast cells expressing GFP-Vrg4 as an early Golgi marker and Sec7-DsRed as a late Golgi marker were imaged by confocal microscopy, with cell images in the blue channel. Z-stacks of 24 optical sections each were collected every 2 s. The movie frames are average projections of the raw Z-stacks.

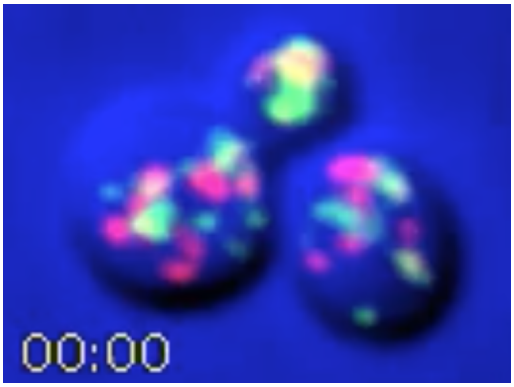

Movie 4.2: 4D movie after deconvolution. Yeast cells expressing GFP-Vrg4 as an early Golgi marker and Sec7-DsRed as a late Golgi marker were imaged by confocal microscopy, with cell images in the blue channel. Z-stacks of 24 optical sections each were collected every 2 s. The red and green channels were deconvolved. Maturation events can be observed when green Golgi cisternae turn red.

CHAPTER 5

IMPROVED DECONVOLUTION OF VERY WEAK CONFOCAL SIGNALS

Abstract

Deconvolution is typically used to sharpen fluorescence images, but when the signal-to-noise ratio is low, the primary benefit is reduced noise and a smoother appearance of the fluorescent structures. 3D time-lapse (4D) confocal image sets can be improved by deconvolution. However, when the confocal signals are very weak, the popular Huygens deconvolution software erases fluorescent structures that are clearly visible in the raw data. We find that this problem can be avoided by prefiltering the optical sections with a Gaussian blur. Analysis of real and simulated data indicates that the Gaussian blur prefilter preserves meaningful signals while enabling removal of background noise. This approach is very simple, and it allows Huygens to be used with 4D imaging conditions that minimize photodamage.

Introduction

Deconvolution is an established method for sharpening fluorescence images and removing background noise (Biggs, 2010; Sage et al., 2017). The usual input to a deconvolution algorithm is a Z-stack of optical sections generated by widefield or confocal microscopy. Because the benefits of deconvolution are fully realized when the signals are strong, the creators of deconvolution software recommend capturing a large number of photons while keeping the pixel sizes and Z-step intervals relatively small.

This chapter is a manuscript under review with the same title and the following author list: Kasey J. Day, Patrick J. La Rivière, Talon Chandler, Vytas P. Bindokas, Nicola J. Ferrier, Benjamin S. Glick. I performed all data acquisition and processing, and assisted with software testing and the interpretations. P.J.L.R. performed the simulations and assisted with the interpretations. T.C. performed exploratory tests with a variety of custom image filters. V.P.B. assisted with testing alternative deconvolution software and with the interpretations. N.J.F. converted ER-Decon data to a usable format and assisted with the interpretations. B.S.G. supervised the study, prepared final figures, and edited the manuscript.

Those conditions are hard to meet with live cell imaging if Z-stacks are being collected at regular intervals to create a 3D time-lapse (4D) data set (De Mey et al., 2008). Intracellular structures are dynamic, so the images need to be taken rapidly. Moreover, the number of captured photons is severely constrained by the need to avoid photodamage to the cells and fluorophores (Pawley, 2006; Carlton et al., 2010). Such issues are prominent in our 4D confocal microscopy studies of secretory compartments in yeast cells (Bevis et al., 2002; Losev et al., 2006; Papanikou et al., 2015). We maximize the scan speed, minimize the intensities of the excitation lasers, and set the pixel sizes and Z-step intervals at the Nyquist limit to achieve a tolerable light exposure while ensuring accurate representation of the imaged structures (Pawley, 2006; Day et al., 2016). The resulting data sets typically comprise thousands of optical sections and have a low signal-to-noise ratio (SNR).

Even though the characteristics of our 4D data are not ideal for deconvolution, the Huygens deconvolution software from Scientific Volume Imaging (SVI) can facilitate the analysis. A number of other freeware and commercial software packages are also available for deconvolution (Biggs, 2010; Sage et al., 2017), but in our experience, those programs are unsuitable for processing of multi-channel 4D confocal data due to some combination of cumbersome user interfaces, lack of compatibility with relevant file formats, and inadequate noise removal. Huygens is unique in that it readily deconvolves our data sets (Papanikou et al., 2015; Day et al., 2016). This software is widely used in the cell biology research community. Importantly, in addition to removing noise, Huygens smooths the uneven shapes and intensities obtained with low-SNR data to generate images that are easy to view and quantify.

Huygens works well for certain low-SNR fluorescence images, but this approach pushes the software to a regime for which it is not optimally designed, and when the fluorescence signals are very weak, Huygens performs poorly (Arigovindan et al., 2013). We encountered this problem when imaging low-abundance proteins associated with yeast organelles. In such experiments, a pixel in the signal-containing portion of a confocal section may capture as few

as 1-2 photons. To enable deconvolution of images with a very low SNR, Agard and colleagues developed deconvolution software called ER-Decon, which employs a novel regularization method tailored to fluorescence data (Arigovindan et al., 2013). However, ER-Decon has incompletely defined parameters, and it proved to be challenging to use. We therefore sought a method for processing very weak fluorescence signals with Huygens.

Results and Discussion

We generated two small 4D data sets to illustrate confocal imaging of organelles in live *Saccharomyces cerevisiae* cells. The parameters were adjusted to capture either weak signals using a line accumulation of 8x, where each line in the image was scanned eight times and the results were summed (Movie 5.1), or very weak signals using a line accumulation of 1x, where each line in the image was scanned only once (Movie 5.2). Projections of representative Z-stacks from the two movies are shown in Figure 5.1. The organelles were dynamic, so the labeling patterns in the two movies are not identical, but the movies were brief and were captured sequentially, so the labeling patterns are similar enough to allow for comparison. With 8x line accumulation, the raw projections are noisy and display fluorescent structures with uneven shapes and intensities (Movie 5.1 and Figure 5.1A). Deconvolution with Huygens efficiently removed the background noise and smoothed the structures. With 1x line accumulation, the data quality is even lower, but fluorescent structures can still be discerned in the raw projections (Movie 5.2 and Figure 5.1B). In this case, deconvolution with Huygens erased almost all of the fluorescent structures. The processing employed standard settings in the Huygens software, including deconvolution with the Classic Maximum Likelihood Estimation algorithm. Although a larger percentage of the fluorescent structures in very weak data sets could be preserved by greatly reducing the number of deconvolution iterations or by using different SNR or background settings, the preserved structures often had distorted shapes (not shown). Similar loss or poor preservation of very weak fluorescent structures was seen with the Good's roughness Maximum Likelihood Estimation algorithm, which is

recommended for use with noisy confocal data (not shown). Based on these observations, we have continued to use standard settings in Huygens. Our data sets often lie between the two extremes depicted in Figure 5.1, and when movies are generated after deconvolution, the fluorescent structures blink because a given structure is erased in some movie frames but not in others (see Movie 5.2). Such movies cannot be productively analyzed.

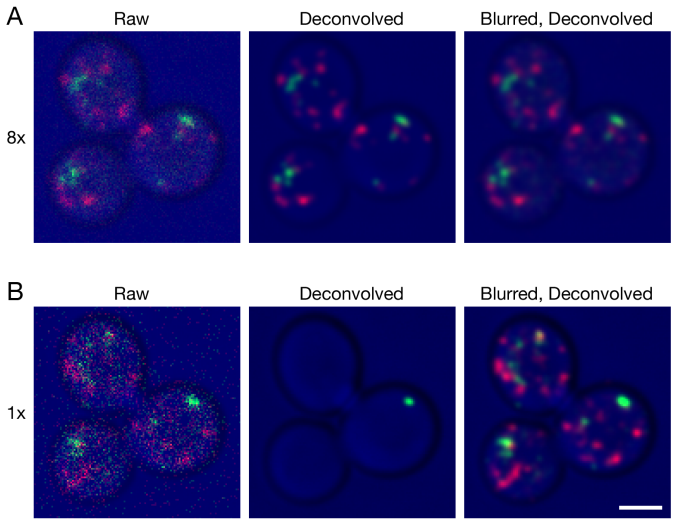

Figure 5.1: Improved deconvolution of live cell data with a Gaussian blur prefilter. Gene replacement in *Saccharomyces cerevisiae* was used to label late Golgi cisternae with Sec7-mCherry (red) and prevacuolar endosomes with Vps8-GFP (green) (Ref. 8). Cells were imaged by 4D confocal microscopy. In consecutive movies, line accumulation was set to (A) 8x or (B) 1x. The data were average projected either with no processing, or after deconvolution with Huygens, or after prefiltering with a 2D Gaussian blur using a radius of 0.75 pixels followed by deconvolution. Shown are representative frames from Movie 5.1 (8x) and Movie 5.2 (1x). Scale bar, 2 μm.

In the course of testing several types and combinations of image filters (Day et al., 2016), we discovered that for very weak confocal signals, the key step was to prefilter the optical sections in ImageJ with a Gaussian blur. That prefilter dramatically improved the results obtained after deconvolution (Movie 5.2 and Figure 5.1B). Fluorescent structures were no longer erased, and instead were preserved and smoothed while the background noise was largely eliminated. Most of the structures visualized by this method were biologically relevant because they persisted between movie frames (Movie 5.2). Essentially identical results were obtained with 2D and 3D Gaussian blurs (not shown), so we use a 2D Gaussian blur because

the processing is faster. This prefiltering step enables us to generate useful 4D movies from data sets that contain very weak confocal signals.

Application of the Gaussian blur prefilter requires the data to be in a suitable format. Our images are collected with a high-sensitivity detector in photon counting mode, and the pixel values are in 8-bit format. For very weak signals, typical pixel values are 0, 1, or 2 because a pixel rarely captures more than 2 photons. To obtain a meaningful blur, the numbers are scaled up to allow for intermediate integer values. We convert the images to 16-bit format and multiply by 256, resulting in typical pixel values of 0, 256, and 512. A Gaussian blur then generates a range of intermediate values, effectively spreading the individual photon signals over multiple pixels.

An important question is how to determine whether a confocal data set is suitable for processing with a Gaussian blur prefilter. Ideally, this prefilter would be used routinely, because even if the average signal intensity is strong, some structures may have very weak signals. The concern with routine application of a Gaussian blur prefilter is that blurring might be propagated to the deconvolved images. Indeed, when the Gaussian blur prefilter was applied to signals strong enough to be preserved during normal deconvolution, we saw some blurring of the fluorescent structures (Movie 5.1 and Figure 5.1A). However, this effect was minor with suitable parameters for the prefilter (see below). Our results indicate that a Gaussian blur prefilter can be used to image structures with a range of signal intensities, resulting in preservation of very weak signals without significant degradation of stronger signals.

Because the labeled structures in our 4D data sets were punctate, we tested whether a Gaussian blur prefilter would also improve deconvolution of other shapes. For this purpose, GFP was fused to a yeast endoplasmic reticulum (ER) protein that localizes mainly to the nuclear envelope (Koning et al., 1996). A single confocal Z-stack was captured at a low excitation laser setting. As shown in Figure 5.2A, which employed 8x line accumulation, the labeled protein appeared as prominent nuclear envelope rings with weaker labeling of

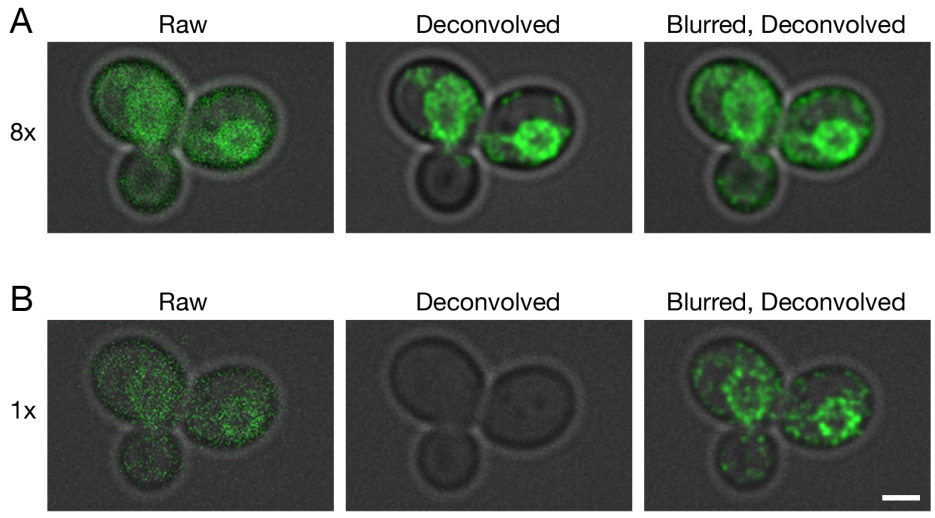

Figure 5.2: Improved deconvolution of non-punctate fluorescence signals with a Gaussian blur prefilter. Gene replacement in *Saccharomyces cerevisiae* was used to label ER membranes with Hmg1-GFP (Koning et al., 1996). A confocal Z-stack was captured with line accumulation set to (A) 8x or (B) 1x. The data were average projected either with no processing, or after deconvolution with Huygens, or after prefiltering with a 2D Gaussian blur using a radius of 0.75 pixels followed by deconvolution. Fluorescence data are superimposed on differential interference contrast images of the cells (gray). Scale bar, 2 μm.

peripheral ER membranes. Deconvolution of the raw data preserved the nuclear envelope rings. When a Gaussian blur was applied before deconvolution, additional signals outside the nuclear envelope were preserved. Figure 5.2B shows a parallel analysis with 1x line accumulation. In this case, the fluorescence signals were completely erased by deconvolution of the raw data, but application of a Gaussian blur before deconvolution preserved the nuclear envelope rings. We conclude that for various types of fluorescence patterns, a Gaussian blur prefilter preserves very weak confocal signals during deconvolution with Huygens.

To explore the Gaussian blur effect systematically, and to confirm that it was not limited to the particular configuration of our confocal microscopy setup, we used simulated data. 3D confocal imaging was simulated for an array of 64 faintly fluorescent point-like objects, each of which was represented by about 10-25 photons spread over multiple optical sections. Figure 5.3A shows projections of this simulated Z-stack before and after processing. After deconvolution with Huygens, only 7 objects were preserved, but after a Gaussian blur prefilter

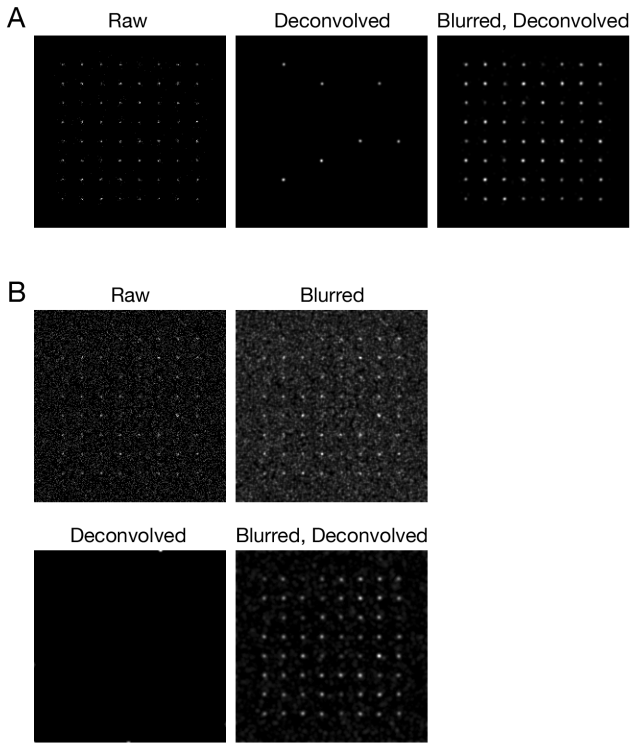

Figure 5.3: Improved deconvolution of simulated data with a Gaussian blur prefilter. Simulated confocal Z-stacks of fluorescent point sources were created as described in Materials and Methods, either (A) without background noise or (B) with background noise. The data were processed and average projected as in Figure 5.1.

followed by deconvolution, all 64 objects were preserved. The total signal intensities for the objects were largely unchanged after either a Gaussian blur alone or a Gaussian blur followed by deconvolution (Figure 5.4). A setting of 0.75 pixels for the radius (sigma) parameter of the prefilter preserved signals while causing very little blur in the final images (Figure 5.5). When the simulation was repeated with added background noise, a Gaussian blur prefilter followed by deconvolution removed most of the noise while preserving all of the objects (Figure 5.3B). In this case, deconvolution in the absence of a prefilter completely erased the objects. The voxels in those simulations were 80x80x250 nm to mimic Nyquist imaging with our confocal system (Pawley, 2006), but similar results were obtained with voxels of 40x40x120 nm (Figure 5.6). Thus, a Gaussian blur prefilter preserves weak confocal signals during deconvolution under multiple real and simulated conditions.

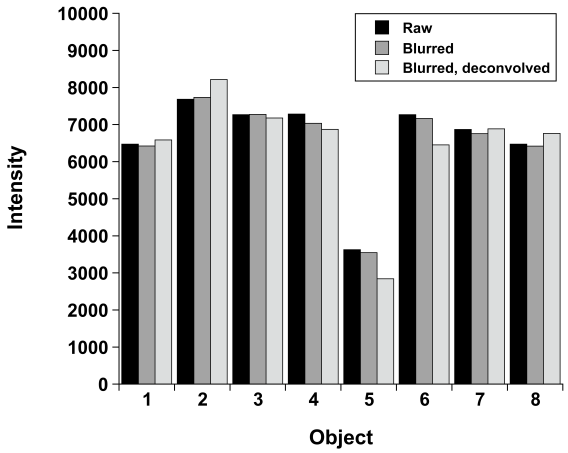

Figure 5.4: Preservation of signal intensities after image processing. For the simulated array shown in Figure 5.3A, the intensities after average projection for the 8 objects in the top row were measured using either the raw data, or the data after a Gaussian blur with a radius of 0.75 pixels, or the data after a Gaussian blur followed by deconvolution with Huygens. Intensity values are in arbitrary units.

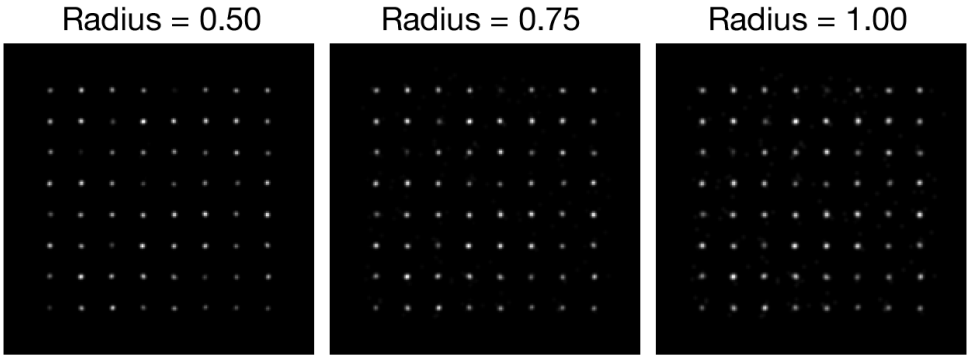

Figure 5.5: Comparison of different radius values for the Gaussian blur prefilter. The simulated confocal Z-stack in Figure 5.3A was subjected to a Gaussian blur prefilter using the indicated radius (sigma) values in pixels, then deconvolved with Huygens and average projected. A radius of 0.50 was not completely effective at preserving the objects, and a radius of 1.00 caused slight blurring in the final image, indicating that a radius of 0.75 was a good compromise.

The paper describing the ER-Decon software showed that Huygens could give unsatisfactory results with low-SNR widefield images (Arigovindan et al., 2013). We processed low-SNR widefield microscopy data from that study with a Gaussian blur prefilter before deconvolution. The improvement was only moderate because Huygens did not erase the structures, but when the signal was weak, the prefilter did increase contrast between labeled

structures and the background (Figure 5.7, right panels), yielding results similar to those obtained with ER-Decon (compare to Figure 5.7 in Arigovindan et al., 2013). The combined observations demonstrate that a Gaussian blur prefilter consistently improves deconvolution of low-SNR fluorescence data.

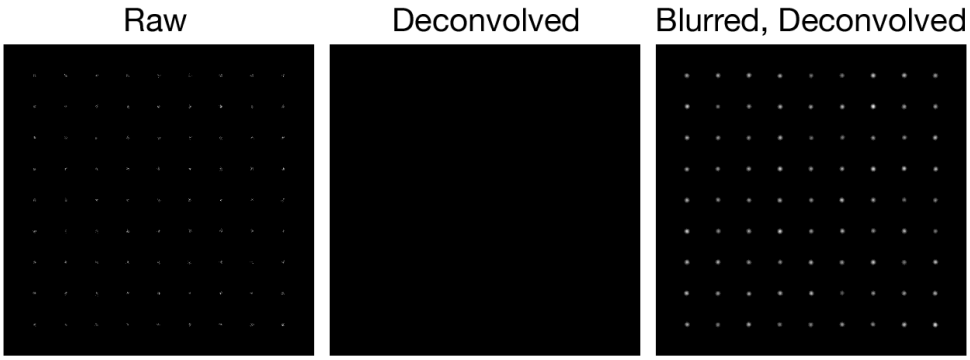

Figure 5.6: Effect of a Gaussian blur prefilter with a smaller voxel size. A simulated confocal Z-stack was generated and processed as in Figure 5.3A, except that the voxel size was 40x40x120 nm.

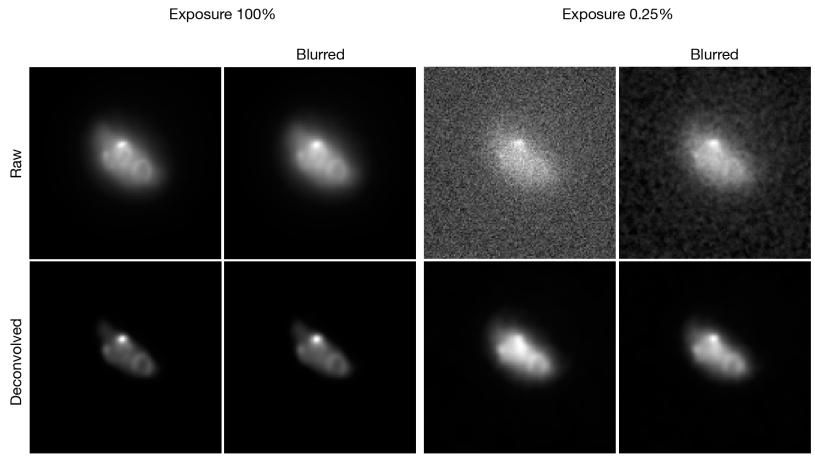

Figure 5.7: Effect of a Gaussian blur prefilter on deconvolution of widefield fluorescence data. Images of fluorescent yeast Zip1 filaments, corresponding to Figure 4 of Ref. 10, were obtained as part of the ER-Decon package and were converted to TIFF format using the Bio-Formats Importer plugin for ImageJ (http://www.openmicroscopy.org/site/support/bio-formats5.1/). The two exposure levels represent strong (100%) or weak (0.25%) signals, respectively. Where indicated, the data were subjected either to a Gaussian blur with a radius of 1.00 pixel, or to deconvolution with Huygens, or to a Gaussian blur prefilter followed by deconvolution. The theoretical PSF was based on imaging parameters supplied with ER-Decon.

The reason for this beneficial effect of the prefilter is not fully understood. Gaussian blurs suppress high-frequency noise. That approach reduces pixel-to-pixel intensity variations, and it can facilitate analysis methods such as edge detection and particle tracking (Cheezum et al., 2001; Russ and Neal, 2015). A different mechanism presumably underlies the ability of a Gaussian blur to prevent loss of very weak signals during deconvolution. Huygens apparently "expects" a gradually varying distribution of the signal intensities within a set of nearby voxels, and the Gaussian blur prefilter converts the data to a form suitable for the Huygens algorithm.

Is a Gaussian blur prefilter before deconvolution an acceptable procedure? Processing of images before deconvolution is not generally recommended, but a Gaussian blur is relatively safe. This filter causes a simple and well behaved transformation of the data, and it preserves the total intensity of a fluorescent structure (Burger and Burge, 2008). Gaussian blurs have previously been employed during deconvolution to suppress noise buildup (Agard et al., 1989). A Gaussian blur prefilter was actually proposed by the founder of SVI as a method for reducing noise sensitivity during deconvolution of confocal data (van Kempen et al., 1997). Therefore, it seems reasonable to apply this prefilter to very weak confocal signals for the novel purpose of avoiding complete erasure of biologically meaningful structures. When the signals are stronger, the Gaussian blur prefilter has a barely detectable effect on the final image, so there seems to be little risk in applying this prefilter routinely.

It could be argued that the Gaussian blur prefilter merely sidesteps a software flaw, in which case a better option would be to fix the Huygens algorithm. However, Huygens is optimized for processing images that exceed a minimum signal strength, and our confocal data sometimes fall below this threshold. Other deconvolution algorithms may perform differently. The available evidence specifically shows that the Gaussian blur prefilter is useful with Huygens. This straightforward method allows us to take advantage of the flexibility, noise removal capability, and smoothing properties of the Huygens software to process very weak fluorescence signals.

Update

After seeing the initial version of this manuscript, scientists at SVI analyzed the performance of Huygens with our data sets, and made a change that improves the deconvolution of images with very weak signals. We find that this change produces excellent results with both real and simulated confocal data obtained under our imaging conditions. The deconvolved images reliably preserve the signals while avoiding the slight loss of sharpness that we observed with a Gaussian blur prefilter. We are grateful to SVI for their responsiveness and constructive feedback.

The improved algorithm is available in Huygens versions 17.04 and later. For investigators running earlier versions of Huygens, the Gaussian blur prefilter remains an effective option for preserving very weak confocal signals during deconvolution.

Materials and Methods

Confocal Microscopy and Image Processing

4D imaging of live yeast cells was performed as described (Day et al., 2016) with a Leica SP5 confocal microscope. Briefly, images were collected at the maximum scan speed with a 63x 1.4-NA objective using a voxel size of 80x80x250 nm and a pinhole setting of 1.2 Airy units. Z-stacks of 28 optical sections were captured at 2 s intervals with the line accumulation (summing) set to either 8x or 1x. Image manipulations other than deconvolution employed ImageJ (http://rsbweb.nih.gov/ij/). Multi-channel 8-bit confocal 3D time series data were converted to TIFF format, and then the TIFF images were converted to 16-bit format, multiplied by 256, and Gaussian blurred where indicated. After deconvolution, the image stacks were average projected and then scaled to provide a quantitatively accurate view of the fluorescent structures (Hammond and Glick, 2000), and the series of projections was exported to AVI movie format. An online tool was used to convert the movies to MP4 format (http://video.online-convert.com/convert-to-mp4).

Simulation of Weakly Fluorescent Objects

A simulated point-like fluorescent object was generated in a voxel array of XYZ dimensions 200x200x40 with a voxel size of 80x80x250 nm. The fluorescent object was centered along the Z-axis, and was duplicated at an XY spacing of 20 pixels to create an 8x8 array.

The effective confocal PSF was generated by multiplying simulated excitation and emission PSFs, which were produced by the ImageJ plugin PSF Generator (http://bigwww.epfl.ch/algorithms/psfgenerator/) using the Born & Wolf 3D optical model with the following parameters: refractive index = 1.5, numerical aperture = 1.4, voxel size = 80x80x250 nm, excitation wavelength = 488 nm, emission wavelength = 510 nm.

The effective confocal PSF was convolved with the simulated objects using fast Fourier transform-based 3D convolution, and the image values were normalized so that the maximum pixel value corresponded to an average of 1 detected photon. The resulting image stack represented the average detected image, which comprised a total of 17.7 photons per object. Where indicated, random background noise was included by adding a value of 0.01 photons to every voxel in the average detected image. This information was used as input to a Poisson random number generator, yielding a simulated image stack in which each voxel value was drawn from a Poisson distribution whose mean was equal to the corresponding voxel value in the average detected image.

The output was saved in 8-bit TIFF format, and was scaled so that a pixel value of 255 corresponded to 4 photons. Further processing was carried out as for the live cell confocal data except that Gaussian blurring and/or deconvolution were performed with 8-bit format. The images were then converted to 16-bit format and multiplied by 256 followed by average projection.

To quantify the signal intensity for an object after average projection, ImageJ was used to create a selection of 20x20 pixels centered on the object, and the integrated density was measured. For the deconvolved image, the numbers were multiplied by a correction factor to compensate for scaling of the image by Huygens.

Deconvolution

Deconvolution with Huygens (https://svi.nl/HomePage) was performed on an iMac using up to 40 iterations of the Classic Maximum Likelihood Estimation algorithm with a theoretical point spread function (PSF). Background correction was automatic except in the case of the simulated confocal Z-stacks with added background noise, for which the background setting was manually adjusted to 0.8. The SNR setting, adjusted empirically to give satisfactory results, was 4 for the live cell confocal data, or 7 for the simulated confocal Z-stacks with no added background noise, or 1 for the simulated confocal Z-stack with added background noise, or 10 for the widefield data. The other parameters used by the Huygens algorithm were configured either for confocal microscopy of live yeast cells (Day et al., 2016), or confocal microscopy of simulated fluorescent objects imaged under the conditions specified during the simulation, or widefield microscopy under the conditions reported for the ER-Decon software (Arigovindan et al., 2013).

The ER-Decon software and associated image data were obtained from the University of California, San Francisco (http://msg.ucsf.edu/IVE/Download/).

Movies Associated with Chapter 5

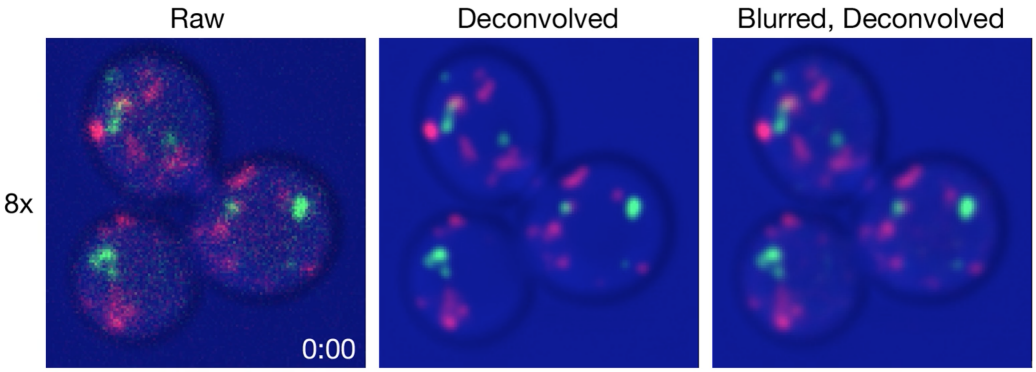

Movie 5.1: Movie generated with weak signals from labeled yeast organelles. Confocal Z-stacks were collected at 2 s intervals with a line accumulation setting of 8x. The final frame of this movie corresponds to Figure 5.1A.

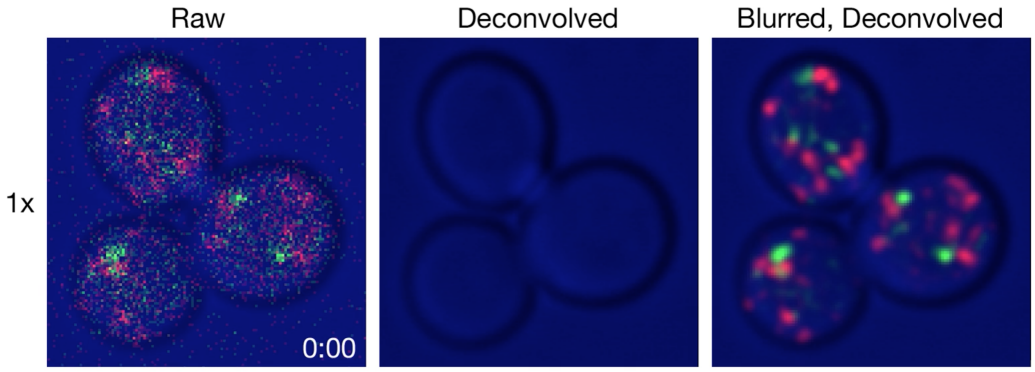

Movie 5.2: Movie generated with very weak signals from labeled yeast organelles. Confocal Z-stacks were collected at 2 s intervals with a line accumulation setting of 1x. The final frame of this movie corresponds to Figure 5.1B.

CHAPTER 6

DISCUSSION

The Merits of *S. cerevisiae* as a Model Organism

The eukaryotic cell uses membrane-bound compartments linked in networks of trafficking routes to process and sort biosynthetic and endocytic cargo. These trafficking routes require specific machineries to carry out the processes of membrane transport and compartment maturation. Despite significant progress, the field still lacked a comprehensive view of how compartments, trafficking routes, and molecular components are coordinated. I have addressed two key aspects: (1) the role of COPI in the Golgi and (2) the organization of the yeast endomembrane system.

COPI functions as a vesicular coat in intra-Golgi transport, but its exact function there was unclear. I helped test whether COPI plays a part in Golgi organization and maturation. Using the budding yeast *Saccharomyces cerevisiae*, I applied the anchor-away method to rapidly inactivate COPI, and then analyzed Golgi function and maturation. During Golgi maturation, a sharp transition from early to late Golgi occurs, in which an early Golgi marker departs just as a late Golgi marker arrives at a Golgi structure. When COPI was inactivated, the early Golgi marker failed to depart while the late Golgi marker continued to recycle, indicating that COPI is required to drive maturation specifically at the early Golgi. These results indicate that COPI is responsible for recycling early Golgi components during maturation, but that a different mechanism drives recycling of late Golgi components.

I also assessed endosomal organization in budding yeast. In mammalian cells, the endocytic pathway involves early, late, and recycling endosomal compartments, which can exchange material with the TGN. Contrary to prevailing assumptions, I found that budding yeast does not possess a distinct early or recycling endosome, but rather that the TGN fulfills the functions of those compartments. I showed that yeast also has a prevacuolar endosome, or PVE, which is analogous to a late endosome, but does not mature in the same way as

a mammalian late endosome. I propose that budding yeast has a simple endomembrane organization, and that the TGN is a compartment of both the biosynthetic and endocytic pathways.

If budding yeast differs significantly from mammals in its endosomal compartment organization, what are the implications for *S. cerevisiae* as a model organism for membrane traffic? The idea that yeast endosomes are more streamlined than the mammalian endosomal network might suggest that yeasts transport pathways and sorting mechanisms will not translate to higher eukaryotes. However, a more positive interpretation is that with an improved understanding of its organization, yeast is even better poised to address questions about endomembrane transport. Yeast still must carry out the same endocytic and biosynthetic functions using the same machineries, many of which are largely conserved throughout eukaryotes. The yeast TGN must have an even higher capacity for sorting than previously appreciated, as it now appears that it combines the functions of three compartments into one. The goal of a model organism is not necessarily to mirror the conditions of a higher organism, but to provide a simpler, more tractable system for study. In this respect, yeast is an ideal model for membrane traffic.

My work with both COPI and endosomes demonstrates the utility of budding yeast for studying features that are relevant to most endomembrane systems. The analysis of COPI function at the Golgi could not have been carried out in most organisms. The nonstacked Golgi of *S. cerevisiae* makes it possible to visualize cisternal maturation. Multiple paralogs of trafficking components, including COPI, occur more commonly in higher eukaryotes, and can complicate analysis (Moelleken et al., 2007). At yeast endosomes, the machineries responsible for regulating, forming, and recognizing vesicular traffic nearly all have homologs in mammalian cells, but act in fewer pathways, with fewer redundancies. Studies in the streamlined yeast endomembrane system will continue to parse out the roles of the SNAREs, GTPases, tethers, and coats that drive these pathways.

The work described in this thesis also highlights the role of the yeast TGN as the major sorting station in the endomembrane system. The sorting of endocytic cargo occurs at the TGN, not at a distinct early endosomal compartment. Recycling of components to the plasma membrane and sorting of polarized secretory cargo also occurs at the TGN, rather than in a distinct recycling endosome. With slightly improved resolution, we may soon be able to identify TGN subdomains that accomplish these sorting functions in yeast. One likely possibility is that the TGN achieves sorting into transport pathways through a temporal organization as well as spatial segregation. For instance, clathrin adaptors are recruited to the TGN sequentially, such that Gga-containing vesicles could segregate their cargo before AP-1-containing vesicles form (Daboussi et al., 2012). Understanding the mechanisms coordinating transport at the TGN has become a central focus of membrane traffic research.

The differences between yeast and mammalian endosomes also provide insight into an evolutionary understanding of endomembrane compartmentation. In plants, endocytic material is targeted to a TGN/early endosome compartment, and sorted cargo is delivered from this compartment to a PVE-like late endosome (Dettmer et al., 2006). Plants and budding yeast therefore bear striking similarities in endomembrane organization. An appealing possibility is that the yeast and plant systems represent an ancestral organization. According to this hypothesis, mammalian cells have segregated the functions of the TGN and PVE to distinct membrane-bound compartments, perhaps elaborating on a simple organization to fulfill increased sorting demands. It will be essential to examine the endomembrane organization of other organisms, including other yeasts and more divergent eukaryotes such as protists, to determine whether the yeast and plant systems are truly ancestral. Given the current limited understanding, another possibility is that both budding yeast and plants have simplified the organization of a more complex ancestor, collapsing the functions of multiple compartments into two types of endosomes. Both loss and gain of complexity occur in evolutionary lineages. Rab GTPases, which help define endomembrane compartments, provide a useful example. The last common eukaryotic ancestor had around 20 different Rab family

GTPases. *S. cerevisiae* has only 11 Rabs, while humans have over 60, and *D. melanogaster* and *C. elegans* each have almost 30 Rabs (Li and Marlin, 2015). Budding yeast has lost some Rabs that are conserved in other eukaryotic lineages while mammals have greatly expanded their Rab repertoire (Diekmann et al., 2011). This expansion is assumed to track with increased endomembrane trafficking complexity, but it is likely that the LECA already possessed a surprisingly complex endomembrane system.

Seeing Is Believing: Visualizing Compartmental Dynamics

Diagrams of the cell tend to suggest that compartments are static structures that exchange vesicular traffic but remain largely stable, isolated, and unchanging. In reality, subcellular compartments are highly dynamic and interactive. The cell tends to maintain homeostasis at a broad level, but on a short time scale, structures form, disappear, make contacts, and change morphologies. Static images of cells therefore do not provide a complete picture of compartmental activity.

Fluorescence 4D confocal microscopy has enabled the examination of subcellular compartments and greatly enhanced our understanding of compartmental dynamics. In the past several years, the sensitivity and resolution of confocal microscopy has improved drastically. For a large portion of the analysis described in this thesis, it was important to visualize compartments over time with fairly high spatial and temporal resolution. This requirement was often challenging to meet, especially when trying to visualize proteins tagged endogenously. I overcame several obstacles to generate movies that provided valuable information about compartmental dynamics.

Optimization of fluorescent tags has improved their brightness, photostability, and monomeric properties. With better fluorescent protein tags, I was able to collect longer movies, which permitted the analysis of long-lived PVE structures as well as the persistent early Golgi structures that formed when COPI was inactivated. I have found that using HaloTag with improved fluorescent ligands, it is now possible to visualize even lowly expressed components

of the endomembrane system at endogenous levels. This level of analysis opens the door to a detailed kinetic examination of an even wider range of endomembrane proteins.

To follow individual structures reliably over long periods, I found it necessary to optimize confocal imaging parameters as well. Multiple optical sections must be collected to image an entire cell for each frame of a movie, resulting in thousands of slices. My improved imaging techniques emphasize the importance of minimizing photobleaching, scanning rapidly, and making the few emitted photons count toward generating a meaningful signal. I then deconvolve the movies using an improved method that involves a pre-blurring step. I found that this additional step preserves signal from weak structures during the deconvolution process, resulting in clean structures that can be faithfully tracked from frame to frame.

Tracking of individual endomembrane compartments over time can provide information that is nearly impossible to glean from static images. Movies can show compartmental fusion and fission, as well as the kinetics of arrival, accumulation, and departure of molecular markers. By visualizing multiple markers on a compartment at a time, I was able to decipher their spatial and temporal relationships. Importantly, I found that temporal analysis is critical for determining the subcellular localization of markers on maturing compartments. For instance, I examined Sec7, Kex2, AP-1, and Tlg1 which do not always perfectly overlap in static images. Through temporal analysis, I found that they all localize to the same compartment, the TGN, at slightly different points in the lifetime of a maturing TGN structure. The kinetics of their arrival and departure provide interesting insight into the mechanisms that organize TGN trafficking pathways.

Future Directions

The proposed models for Golgi maturation, combined with the versatile analysis that is possible in the simple yeast endomembrane system, raise exciting prospects for determining how trafficking pathways are coordinated in budding yeast. First, the molecular determinants of late Golgi maturation remain to be identified. AP-1 is the strongest candidate, as it

has been implicated in targeting retrograde traffic to the Golgi (Valdivia et al., 2002). By inactivating AP-1 and perhaps other accessory clathrin adaptors, it may be possible to see a selective loss of intra-Golgi recycling of late Golgi components. The AP-3 adaptor complex also merits further study. An analysis of the interactions that AP-3 makes with membrane and with other proteins may result in a better understanding of the unique localization of AP-3 around TGN structures.

The prominent role of the yeast TGN in the endocytic pathway also merits further investigation. What molecular machineries enable the TGN to receive plasma membrane-derived endocytic traffic, and are these components distinct from the machinery that receives PVE-derived carriers? Based on my temporal data and interactions described by others, I propose that the Rab GTPase Ypt6 could drive the recruitment of tethers and SNAREs that capture incoming traffic from each of these destinations (Quenneville et al., 2006; Siniossoglou and Pelham, 2001). Finally, future studies on the yeast TGN will need to take into account the convergence of endocytic and biosynthetic cargo. Identifying the mechanisms that permit rapid exclusion or sorting of these cargoes into multiple outgoing pathways will be a challenging but worthwhile pursuit. It is likely that these sorting mechanisms will be broadly applicable to the endosomal compartments of mammalian cells as well.

This work has set the stage, both conceptually and technically, for creating a kinetic roadmap of Golgi maturation. The results will help the field to understand Golgi compartmentation in concrete molecular terms, and will take us closer to the long-standing goal of elucidating how the Golgi functions as a dynamic central sorting station in the cell.

REFERENCES

Abe, M., Noda, Y., Adachi, H., and Yoda, K. (2004). Localization of GDP-mannose transporter in the Golgi requires retrieval to the endoplasmic reticulum depending on its cytoplasmic tail and coatomer. J Cell Sci 117, 5687-5696.

Abeliovich, H., Grote, E., Novick, P., and Ferro-Novick, S. (1998). Tlg2p, a yeast syntaxin homolog that resides on the Golgi and endocytic structures. J Biol Chem 273, 11719-11727.

Agard, D.A., Hiraoka, Y., Shaw, P., and Sedat, J.W. (1989). Fluorescence microscopy in three dimensions. In Fluorescence Microscopy of Living Cells in Culture, Part B (Methods in Cell Biology, Vol 30), D.L. Taylor, and Y. Wang, eds. (San Diego: Academic Press), pp. 353-377.

Ang, A.L., Taguchi, T., Francis, S., Fölsch, H., Murrells, L.J., Pypaert, M., Warren, G., and Mellman, I. (2004). Recycling endosomes can serve as intermediates during transport from the Golgi to the plasma membrane of MDCK cells. J Cell Biol 167, 531-543.

Angers, C.G., and Merz, A.J. (2009). HOPS interacts with Apl5 at the vacuole membrane and is required for consumption of AP-3 transport vesicles. Mol Biol Cell 20, 4563-4574.

Appenzeller-Herzog, C., and Hauri, H.P. (2006). The ER-Golgi intermediate compartment (ERGIC): in search of its identity and function. J Cell Sci 119, 2173-2183.

Arai, S., Noda, Y., Kainuma, S., Wada, I., and Yoda, K. (2008). Ypt11 functions in bud-directed transport of the Golgi by linking Myo2 to the coatomer subunit Ret2. Curr Biol 18, 987-991.

Arigovindan, M., Fung, J.C., Elnatan, D., Menella, V., Chan, Y.H., Pollard, M., Branlund, E., Sedat, J.W., and Agard, D.A. (2013). High-resolution restoration of 3D structures from widefield images with extreme low signal-to-noise-ratio. Proc Natl Acad Sci USA 110, 17344-17349.

Arlt, H., Auffarth, K., Kurre, R., Lisse, D., Piehler, J., and Ungermann, C. (2015). Spatiotemporal dynamics of membrane remodeling and fusion proteins during endocytic transport. Mol Biol Cell 26, 1357-1370.

Audhya, A., Foti, M., and Emr, S.D. (2000). Distinct roles for the yeast phosphatidylinositol 4-kinases, Stt4p and Pik1p, in secretion, cell growth, and organelle membrane dynamics. Mol Biol Cell 11, 2673-2689.

Banaszynski, L.A., Liu, C.W., and Wandless, T.J. (2005). Characterization of the FKBP·rapamycin·FRB ternary complex. J Am Chem Soc 127, 4715-4721.

Bankaitis, V.A., Garcia-Mata, R., and Mousley, C.J. (2012). Golgi membrane dynamics and lipid metabolism. Curr Biol 22, R414-R424.

Bard, F., and Malhotra, V. (2006). The formation of TGN-to-plasma-membrane transport carriers. Annu Rev Cell Dev Biol 22, 439-455.

Barlowe, C.K., and Miller, E.A. (2013). Secretory protein biogenesis and traffic in the early secretory pathway. Genetics 193, 383-410.

Barrero, J.J., Papanikou, E., Casler, J.C., Day, K.J., and Glick, B.S. (2016). An improved reversibly dimerizing mutant of the FK506-binding protein FKBP. Cell Logist 6, e1204848.

Bartnicki-Garcia, S. (2006). Chitosomes: past, present and future. FEMS Yeast Res 6, 957-965.

Bayle, J.H., Grimley, J.S., Stankunas, K., Gestwicki, J.E., Wandless, T.J., and Crabtree, G.R. (2006). Rapamycin analogs with differential binding specificity permit orthogonal control of protein activity. Chem Biol 13, 99-107.

Beck, R., Ravet, M., Wieland, F.T., and Cassel, D. (2009). The COPI system: Molecular mechanisms and function. FEBS Lett 583, 2701-2709.

Becker, B., Bölinger, B., and Melkonian, M. (1995). Anterograde transport of algal scales through the Golgi complex is not mediated by vesicles. Trends Cell Biol 5, 305-307.

Becuwe, M., and Léon, S. (2014). Integrated control of transporter endocytosis and recycling by the arrestin-related protein Rod1 and the ubiquitin ligase Rsp5. Elife 3.

Benli, M., Döring, F., Robinson, D.G., Yang, X., and Gallwitz, D. (1996). Two GTPase isoforms, Ypt31p and Ypt32p, are essential for Golgi function in yeast. EMBO J 15, 6460-6475.

Bevis, B.J., and Glick, B.S. (2002). Rapidly maturing variants of the Discosoma red fluorescent protein (DsRed). Nat Biotechnol 20, 83-87.

Bevis, B.J., Hammond, A.T., Reinke, C.A., and Glick, B.S. (2002). De novo formation of transitional ER sites and Golgi structures in Pichia pastoris. Nat Cell Biol 4, 750-756.

Beznoussenko, G.V., Dolgikh, V.V., Seliverstova, E.V., Semenov, P.B., Tokarev, Y.S., Trucco, A., Micaroni, M., Di Giandomenico, D., Auinger, O., Senderskiy, I.V., et al. (2007). Analogs of the Golgi complex in microsporidia: structure and avesicular mechanisms of function. J Cell Sci 120, 1288-1298.

Bharucha, N., Liu, Y., Papanikou, E., McMahon, C., Esaki, M., Jeffrey, P.D., Hughson, F.M., and Glick, B.S. (2013). Sec16 influences transitional ER sites by regulating rather than organizing COPII. Mol Biol Cell 24, 3406-3419.

Bhave, M., Papanikou, E., Iyer, P., Pandya, K., Jain, B.K., Ganguly, A., Sharma, C., Pawar, K., Austin, J., Day, K.J., et al. (2014). Golgi enlargement in Arf-depleted yeast cells is due to altered dynamics of cisternal maturation. J Cell Sci 127, 250-257.

Biggs, D.S. (2010). 3D Deconvolution Microscopy. Curr Protoc Cytom 52, 12.19.11-12.19.20.

Bilodeau, P.S., Urbanowski, J.L., Winistorfer, S.C., and Piper, R.C. (2002). The Vps27p Hse1p complex binds ubiquitin and mediates endosomal protein sorting. Nat Cell Biol 4, 534-539.

Black, M.W., and Pelham, H.R. (2000). A selective transport route from Golgi to late endosomes that requires the yeast GGA proteins. J Cell Biol 151, 587-600.

Bonfanti, L., Mironov, A.A., Jr., Martnez-Menrguez, J., Martella, O., Fusella, A., Baldassarre, M., Buccione, R., Geuze, H.J., Mironov, A.A., and Luini, A. (1998). Procollagen traverses the Golgi stack without leaving the lumen of cisternae: evidence for cisternal maturation. Cell 95, 993-1003.

Bonifacino, J.S. (2014). Adaptor proteins involved in polarized sorting. J Cell Biol 204, 7-17.

Bonifacino, J.S., and Glick, B.S. (2004). The mechanisms of vesicle budding and fusion. Cell 116, 153-166.

Bonifacino, J.S., and Traub, L.M. (2003). Signals for sorting of transmembrane proteins to endosomes and lysosomes. Annu Rev Biochem 72, 395-447.

Braulke, T., and Bonifacino, J.S. (2009). Sorting of lysosomal proteins. Biochim Biophys Acta 1793, 605-614.

Brigance, W.T., Barlowe, C., and Graham, T.R. (2000). Organization of the yeast Golgi complex into at least four functionally distinct compartments. Mol Biol Cell 11, 171-182.

Bright, N.A., Gratian, M.J., and Luzio, J.P. (2005). Endocytic delivery to lysosomes mediated by concurrent fusion and kissing events in living cells. Curr Biol 15, 360-365.

Burd, C., and Cullen, P.J. (2014). Retromer: a master conductor of endosome sorting. Cold Spring Harb Perspect Biol 6.

Burd, C.G., and Emr, S.D. (1998). Phosphatidylinositol(3)-phosphate signaling mediated by specific binding to RING FYVE domains. Mol Cell 2, 157-162.

Burger, W., and Burge, M.J. (2008). Digital Image Processing (New York, NY: Springer).

Cabrera, M., Ostrowicz, C.W., Mari, M., LaGrassa, T.J., Reggiori, F., and Ungermann, C. (2009). Vps41 phosphorylation and the Rab Ypt7 control the targeting of the HOPS complex to endosome-vacuole fusion sites. Mol Biol Cell 20, 1937-1948.

Cai, H., Reinisch, K., and Ferro-Novick, S. (2007). Coats, tethers, Rabs, and SNAREs work together to mediate the intracellular destination of a transport vesicle. Dev Cell 12, 671-682.

Carlsson, A.E., Shah, A.D., Elking, D., Karpova, T.S., and Cooper, J.A. (2002). Quantitative analysis of actin patch movement in yeast. Biophys J 82, 2333-2343.

Carlton, P.M., Boulanger, J., Kervrann, C., Sibarita, J.B., Salamero, J., Gordon-Messer, S., Bressan, D., Haber, J.E., Hasse, S., Shao, L., et al. (2010). Fast live simultaneous multiwavelength four-dimensional optical microscopy. Proc Natl Acad Sci USA 107, 16016-16022.

Casanova, J.E. (2007). Regulation of Arf activation: the Sec7 family of guanine nucleotide exchange factors. Traffic 8, 1476-1485.

Cerveny, K.L., McCaffery, J.M., and Jensen, R.E. (2001). Division of mitochondria requires a novel DNM1-interacting protein, Net2p. Mol Biol Cell 12, 309-321.

Chanat, E., and Huttner, W.B. (1991). Milieu-induced, selective aggregation of regulated secretory proteins in the trans-Golgi network. J Cell Biol 115, 1505-1519.

Cheezum, M.K., Walker, W.F., and Guilford, W.H. (2001). Quantitative comparison of algorithms for tracking single fluorescent particles. Biophys J 81, 2378-2388.

Chen, S.H., Chen, S., Tokarev, A.A., Liu, F., Jedd, G., and Segev, N. (2005). Ypt31/32 GTPases and their novel F-box effector protein Rcy1 regulate protein recycling. Mol Biol Cell 16, 178-192.

Chen, S.H., Shah, A.H., and Segev, N. (2011). Ypt31/32 GTPases and their F-Box effector Rcy1 regulate ubiquitination of recycling proteins. Cellular Logistics 1, 21.

Chi, R.J., Liu, J., West, M., Wang, J., Odorizzi, G., and Burd, C.G. (2014). Fission of SNX-BAR-coated endosomal retrograde transport carriers is promoted by the dynamin-related protein Vps1. J Cell Biol 204, 793-806.

Clermont, Y., Rambourg, A., and Hermo, L. (1995). Trans-Golgi network (TGN) of different cell types: three-dimensional structural characteristics and variability. Anat Rec 242, 289-301.

Conibear, E. (2010). Converging views of endocytosis in yeast and mammals. Curr Opin Cell Biol 22, 513-518.

Connerly, P.L., Esaki, M., Montegna, E.A., Strongin, D.E., Levi, S., Soderholm, J., and Glick, B.S. (2005). Sec16 is a determinant of transitional ER organization. Curr Biol 15, 1439-1447.

Cooper, A.A., and Stevens, T.H. (1996). Vps10p cycles between the late-Golgi and prevacuolar compartments in its function as the sorting receptor for multiple yeast vacuolar hydrolases. J Cell Biol 133, 529-541.

Cosson, P., Amherdt, M., Rothman, J.E., and Orci, L. (2002). A resident Golgi protein is excluded from peri-Golgi vesicles in NRK cells. Proc Natl Acad Sci USA 99, 12831-12834.

Cosson, P., and Letourneur, F. (1997). Coatomer (COPI)-coated vesicles: role in intracellular transport and protein sorting. Curr Opin Cell Biol 9, 484-487.

Costaguta, G., Stefan, C.J., Bensen, E.S., Emr, S.D., and Payne, G.S. (2001). Yeast Gga coat proteins function with clathrin in Golgi to endosome transport. Mol Biol Cell 12, 1885-1896.

Cowles, C.R., Odorizzi, G., Payne, G.S., and Emr, S.D. (1997). The AP-3 adaptor complex is essential for cargo-selective transport to the yeast vacuole. Cell 91, 109-118.

Daboussi, L., Costaguta, G., and Payne, G.S. (2012). Phosphoinositide-mediated clathrin adaptor progression at the trans-Golgi network. Nat Cell Biol 14, 239-248.

Dacks, J.B., and Field, M.C. (2007). Evolution of the eukaryotic membrane-trafficking system: origin, tempo and mode. J Cell Sci 120, 2977-2985.

Dancourt, J., and Barlowe, C. (2010). Protein sorting receptors in the early secretory pathway. Annu Rev Biochem 79, 777-802.

Day, K.J., Staehelin, L.A., and Glick, B.S. (2013). A three-stage model of Golgi structure and function. Histochem Cell Biol 140, 239-249.

Day, K.J., Papanikou, E., and Glick, B.S. (2016). 4D confocal imaging of yeast organelles. Methods Mol Biol 1496, 1-11.

De Matteis, M.A., and Luini, A. (2008). Exiting the Golgi complex. Nat Rev Mol Cell Biol 9, 273-284.

De Mey, J.R., Kessler, P., Dompierre, J., Cordelires, F.P., Dieterlen, A., Vonesch, J.L., and Sibarita, J.B. (2008). Fast 4D microscopy. Methods Cell Biol 85, 83-112.

Dean, N., Zhang, Y.B., and Poster, J.B. (1997). The VRG4 gene is required for GDP-mannose transport into the lumen of the golgi in the yeast, *Saccharomyces cerevisiae*. J Biol Chem 272, 31908-31914.

Delacour, D., Greb, C., Koch, A., Salomonsson, E., Leffler, H., Le Bivic, A., and Jacob, R. (2007). Apical sorting by galectin-3-dependent glycoprotein clustering. Traffic 8, 379-388.

Dell'Angelica, E.C., Puertollano, R., Mullins, C., Aguilar, R.C., Vargas, J.D., Hartnell, L.M., and Bonifacino, J.S. (2000). GGAs: a family of ADP ribosylation factor-binding proteins related to adaptors and associated with the Golgi complex. J Cell Biol 149, 81-94.

Deng, Y., Guo, Y., Watson, H., Au, W.C., Shakoury-Elizeh, M., Basrai, M.A., Bonifacino, J.S., and Philpott, C.C. (2009). Gga2 mediates sequential ubiquitin-independent and ubiquitin-dependent steps in the trafficking of ARN1 from the trans-Golgi network to the vacuole. J Biol Chem 284, 23830-23841.

Dettmer, J., Hong-Hermesdorf, A., Stierhof, Y.D., and Schumacher, K. (2006). Vacuolar H+-ATPase activity is required for endocytic and secretory trafficking in Arabidopsis. Plant Cell 18, 715-730.

Diekmann, Y., Seixas, E., Gouw, M., Tavares-Cadete, F., Seabra, M.C., Pereira-Leal, J.B. (2011) Thousands of Rab GTPases for the Cell Biologist. PLOS Computational Biology 7(10): e1002217.

Donohoe, B.S., Kang, B.H., Gerl, M.J., Gergely, Z.R., McMichael, C.M., Bednarek, S.Y., and Staehelin, L.A. (2013). cis-Golgi cisternal assembly and biosynthetic activation occur sequentially in plants and algae. Traffic 14, 551-567.

Donohoe, B.S., Kang, B.H., and Staehelin, L.A. (2007). Identification and characterization of COPIa- and COPIb-type vesicle classes associated with plant and algal Golgi. Proc Natl Acad Sci USA 104, 163-168.

Doray, B., Ghosh, P., Griffith, J., Geuze, H.J., and Kornfeld, S. (2002). Cooperation of GGAs and AP-1 in packaging MPRs at the trans-Golgi network. Science 297, 1700-1703.

Duden, R., and Schekman, R. (1997). Insights into Golgi function through mutants in yeast and animal cells. In The Golgi Apparatus, E.G. Berger, and J. Roth, eds. (Basel: Birkhuser Verlag), pp. 219-246.

Dunphy, W.G., and Rothman, J.E. (1985). Compartmental organization of the Golgi stack. Cell 42, 13-21.

Eckert, E.S.P., Reckmann, I., Hellwig, A., Röhling, S., El-Battari, A., Wieland, F.T., and Popoff, V. (2014). Golgi phosphoprotein 3 triggers signal-mediated incorporation of glycosyltransferases into coatomer-coated (COPI) vesicles. J Biol Chem 289, 31319-31329.

Emr, S., Glick, B.S., Linstedt, A.D., Lippincott-Schwartz, J., Luini, A., Malhotra, V., Marsh, B.J., Nakano, A., Pfeffer, S.R., Rabouille, C., et al. (2009). Journeys through the Golgi–taking stock in a new era. J Cell Biol 187, 449-453.

Engqvist-Goldstein, A.E., and Drubin, D.G. (2003). Actin assembly and endocytosis: from yeast to mammals. Annu Rev Cell Dev Biol 19, 287-332.

Faini, M., Beck, R., Wieland, F.T., and Briggs, J.A. (2013). Vesicle coats: structure, function, and general principles of assembly. Trends Cell Biol 23, 279-288.

Farquhar, M.G., and Palade, G.E. (1981). The Golgi apparatus (complex) - (1954-1981) - from artifact to center stage. J Cell Biol 91, 77s-103s.

Fasshauer, D., Sutton, R.B., Brunger, A.T., and Jahn, R. (1998). Conserved structural features of the synaptic fusion complex: SNARE proteins reclassified as Q- and R-SNAREs. Proc Natl Acad Sci U S A 95, 15781-15786.

Fishbain, S., Prakash, S., Herrig, A., Elsasser, S., and Matouschek, A. (2011). Rad23 escapes degradation because it lacks a proteasome initiation region. Nat Commun 2, 192.

Fitzgerald, I., and Glick, B.S. (2014). Secretion of a foreign protein from budding yeasts is enhanced by cotranslational translocation and by suppression of vacuolar targeting. Microb Cell Fact 13, 125.

Flores Martinez, A., and Schwencke, J. (1988). Chitin synthetase activity is bound to chitosomes and to the plasma membrane in protoplasts of *Saccharomyces cerevisiae*. Biochim Biophys Acta 946, 328-336.

Furukawa, N., and Mima, J. (2014). Multiple and distinct strategies of yeast SNAREs to confer the specificity of membrane fusion. Sci Rep 4, 4277.

Gabriely, G., Kama, R., and Gerst, J.E. (2007). Involvement of specific COPI subunits in protein sorting from the late endosome to the vacuole in yeast. Mol Cell Biol 27, 526-540.

Gadila, S.K.G., and Kim, K. (2016). Cargo trafficking from the trans-Golgi network towards the endosome. Biol Cell 108, 205.

Gaynor, E.C., and Emr, S.D. (1997). COPI-independent anterograde transport: cargo-selective ER to Golgi protein transport in yeast COPI mutants. J Cell Biol 136, 789-802.

Gaynor, E.C., Chen, C.Y., Emr, S.D., and Graham, T.R. (1998a). ARF is required for maintenance of yeast Golgi and endosome structure and function. Mol Biol Cell 9, 653-670.

Gaynor, E.C., Graham, T.R., and Emr, S.D. (1998b). COPI in ER/Golgi and intra-Golgi transport: do yeast COPI mutants point the way? Biochim Biophys Acta 1404, 33-51.

Genov, G., Glick, B.S., and Barth, A.L. (2005). Brighter reporter genes from multimerized fluorescent proteins. BioTechniques 39, 814-822.

Gilchrist, A., Au, C.E., Hiding, J., Bell, A.W., Fernandez-Rodriguez, J., Lesimple, S., Nagaya, H., Roy, L., Gosline, S.J., Hallett, M., et al. (2006). Quantitative proteomics analysis of the secretory pathway. Cell 127, 1265-1281.

Gillingham, A.K., and Munro, S. (2007). The small G proteins of the Arf family and their regulators. Annu Rev Cell Dev Biol 23, 579-611.

Gleeson, P.A., Lock, J.G., Luke, M.R., and Stow, J.L. (2004). Domains of the TGN: coats, tethers and G proteins. Traffic 5, 315-326.

Glick, B.S., Elston, T., and Oster, G. (1997). A cisternal maturation mechanism can explain the asymmetry of the Golgi stack. FEBS Lett 414, 177-181.

Glick, B.S., and Luini, A. (2011). Models for Golgi traffic: a critical assessment. Cold Spring Harb Perspect Biol 3, a005215.

Glick, B.S., and Malhotra, V. (1998). The curious status of the Golgi apparatus. Cell 95, 883-889.

Goldberg, D.E., and Kornfeld, S. (1983). Evidence for extensive subcellular organization of asparagine-linked oligosaccharide processing and lysosomal enzyme phosphorylation. J Biol Chem 258, 3159-3165.

Goldenring, J.R. (2015). Recycling endosomes. Curr Opin Cell Biol 35, 117-122.

Goldstein, A.L., and McCusker, J.H. (1999). Three new dominant drug resistance cassettes for gene disruption in *Saccharomyces cerevisiae*. Yeast 15, 1541-1553.

Goode, B.L., Eskin, J.A., and Wendland, B. (2015). Actin and endocytosis in budding yeast. Genetics 199, 315-358.

Grant, B.D., and Donaldson, J.G. (2009). Pathways and mechanisms of endocytic recycling. Nat Rev Mol Cell Biol 10, 597-608.

Griffiths, G., Quinn, P., and Warren, G. (1983). Dissection of the Golgi complex. I. Monensin inhibits the transport of viral membrane proteins from medial to trans Golgi cisternae in baby hamster kidney cells infected with Semliki Forest virus. J Cell Biol 96, 835-850.

Grünberg, R., Ferrar, T.S., van der Slot, A.M., Constante, M., and Serrano, L. (2010). Building blocks for protein interaction devices. Nucleic Acids Res 38, 2645-2662.

Guo, Y., Sirkis, D.W., and Schekman, R. (2014). Protein sorting at the trans-Golgi network. Annu Rev Cell Dev Biol 30, 169-206.

Gurunathan, S., Chapman-Shimshoni, D., Trajkovic, S., and Gerst, J.E. (2000). Yeast exocytic v-SNAREs confer endocytosis. Mol Biol Cell 11, 3629-3643.

Hama, H., Schnieders, E.A., Thorner, J., Takemoto, J.Y., and DeWald, D.B. (1999). Direct involvement of phosphatidylinositol 4-phosphate in secretion in the yeast *Saccharomyces cerevisiae*. J Biol Chem 274, 34294-34300.

Hammond, A.T., and Glick, B.S. (2000). Raising the speed limits for 4D fluorescence microscopy. Traffic 1, 935-940.

Hao, M., and Maxfield, F.R. (2000). Characterization of rapid membrane internalization and recycling. J Biol Chem 275, 15279-15286.

Hara-Kuge, S., Kuge, O., Orci, L., Amherdt, M., Ravazzola, M., Wieland, F.T., and Rothman, J.E. (1994). En bloc incorporation of coatomer subunits during the assembly of COP-coated vesicles. J Cell Biol 124, 883-892.

Haruki, H., Nishikawa, J., and Laemmli, U.K. (2008). The anchor-away technique: rapid, conditional establishment of yeast mutant phenotypes. Mol Cell 31, 925-932.

Heitman, J., Movva, N.R., Hiestand, P.C., and Hall, M.N. (1991). FK 506-binding protein proline rotamase is a target for the immunosuppressive agent FK 506 in *Saccharomyces cerevisiae*. Proc Natl Acad Sci U S A 88, 1948-1952.

Helliwell, S.B., Wagner, P., Kunz, J., Deuter-Reinhard, M., Henriquez, R., and Hall, M.N. (1994). TOR1 and TOR2 are structurally and functionally similar but not identical phosphatidylinositol kinase homologues in yeast. Mol Biol Cell 5, 105-118.

Hendricks, K.B., Wang, B.Q., Schnieders, E.A., and Thorner, J. (1999). Yeast homologue of neuronal frequenin is a regulator of phosphatidylinositol-4-OH kinase. Nat Cell Biol 1, 234-241.

Henne, W.M., Buchkovich, N.J., and Emr, S.D. (2011). The ESCRT pathway. Dev Cell 21, 77-91.

Hettema, E.H., Lewis, M.J., Black, M.W., and Pelham, H.R. (2003). Retromer and the sorting nexins Snx4/41/42 mediate distinct retrieval pathways from yeast endosomes. EMBO J 22, 548-557.

Hicke, L., and Riezman, H. (1996). Ubiquitination of a yeast plasma membrane receptor signals its ligand-stimulated endocytosis. Cell 84, 277-287.

Hicke, L., Zanolari, B., Pypaert, M., Rohrer, J., and Riezman, H. (1997). Transport through the yeast endocytic pathway occurs through morphologically distinct compartments and requires an active secretory pathway and Sec18p/N-ethylmaleimide-sensitive fusion protein. Mol Biol Cell 8, 13-31.

Hinners, I., and Tooze, S.A. (2003). Changing directions: clathrin-mediated transport between the Golgi and endosomes. J Cell Sci 116, 763-771.

Hirst, J., Borner, G.H., Antrobus, R., Peden, A.A., Hodson, N.A., Sahlender, D.A., and Robinson, M.S. (2012). Distinct and overlapping roles for AP-1 and GGAs revealed by the "knocksideways" system. Curr Biol 22, 1711-1716.

Hosobuchi, M., Kreis, T., and Schekman, R. (1992). SEC21 is a gene required for ER to Golgi protein transport that encodes a subunit of a yeast coatomer. Nature 360, 603-605.

Huckaba, T.M., Gay, A.C., Pantalena, L.F., Yang, H.C., and Pon, L.A. (2004). Live cell imaging of the assembly, disassembly, and actin cable-dependent movement of endosomes and actin patches in the budding yeast, *Saccharomyces cerevisiae*. J Cell Biol 167, 519-530.

Huotari, J., and Helenius, A. (2011). Endosome maturation. EMBO J 30, 3481-3500.

Hutagalung, A.H., and Novick, P.J. (2011). Role of Rab GTPases in membrane traffic and cell physiology. Physiol Rev 91, 119-149.

Jackson, L.P. (2014). Structure and mechanism of COPI vesicle biogenesis. Curr Opin Cell Biol 29, 67-73.

Jahn, R., and Scheller, R.H. (2006). SNAREs–engines for membrane fusion. Nat Rev Mol Cell Biol 7, 631-643.

Jedd, G., Mulholland, J., and Segev, N. (1997). Two new Ypt GTPases are required for exit from the yeast trans-Golgi compartment. J Cell Biol 137, 563-580.

Jensen, D., and Schekman, R. (2011). COPII-mediated vesicle formation at a glance. J Cell Sci 124, 1-4.

Kelly, B.T., and Owen, D.J. (2011). Endocytic sorting of transmembrane protein cargo. Curr Opin Cell Biol 23, 404-412.

Kim, J.J., Lipatova, Z., Majumdar, U., and Segev, N. (2016). Regulation of Golgi Cisternal Progression by Ypt/Rab GTPases. Dev Cell 36, 440-452.

Kirchhausen, T. (2000). Three ways to make a vesicle. Nat Rev Mol Cell Biol 1, 187-198.

Klausner, R.D., Donaldson, J.G., and Lippincott-Schwartz, J. (1992). Brefeldin A: insights into the control of membrane traffic and organelle structure. J Cell Biol 116, 1071-1080.

Klumperman, J. (2011). Architecture of the mammalian Golgi. Cold Spring Harb Perspect Biol 3, a005181.

Kornfeld, R., and Kornfeld, S. (1985). Assembly of asparagine-linked oligosaccharides. Annu Rev Biochem 54, 631-664.

Kornfeld, S., and Mellman, I. (1989). The biogenesis of lysosomes. Annu Rev Cell Biol 5, 483-525.

Kremers, G.J., Goedhart, J., van Munster, E.B., and Gadella, T.W. (2006). Cyan and yellow super fluorescent proteins with improved brightness, protein folding, and FRET Förster radius. Biochemistry 45, 6570-6580.

Kunz, J., Schneider, U., Deuter-Reinhard, M., Movva, N.R., and Hall, M.N. (1993). Target of rapamycin in yeast, TOR2, is an essential phosphatidylinositol kinase homolog required for G1 progression. Cell 73, 585-596.

Kurokawa, K., Ishii, M., Suda, Y., Ichihara, A., and Nakano, A. (2013). Live cell visualization of Golgi membrane dynamics by super-resolution confocal live imaging microscopy. Methods Cell Biol 118, 235-242.

Kweon, H.S., Beznoussenko, G.V., Micaroni, M., R.S., P., Trucco, A., Martella, O., Di Giandomenico, D., Marra, P., Fusella, A., Di Pentima, A., et al. (2004). Golgi enzymes are enriched in perforated zones of Golgi cisternae but are depleted in COPI vesicles. Mol Biol Cell 15, 4710-4724.

Ladinsky, M.S., Kremer, J.R., Furcinitti, P.S., McIntosh, J.R., and Howell, K.E. (1994). HVEM tomography of the trans-Golgi network: structural insights and identification of a lace-like vesicle coat. J Cell Biol 127, 29-38.

Ladinsky, M.S., Mastronarde, D.N., McIntosh, J.R., Howell, K.E., and Staehelin, L.A. (1999). Golgi structure in three dimensions: functional insights from the normal rat kidney cell. J Cell Biol 144, 1135-1149.

Ladinsky, M.S., Wu, C.C., McIntosh, S., McIntosh, J.R., and Howell, K.E. (2002). Structure of the Golgi and distribution of reporter molecules at 20 degrees C reveals the complexity of the exit compartments. Mol Biol Cell 13, 2810-2825.

Lane, N., and Martin, W. (2010). The energetics of genome complexity. Nature 467, 929-934.

Lanoix, J., Ouwendijk, J., Stark, A., Szafer, E., Cassel, D., Dejgaard, K., Weiss, M., and Nilsson, T. (2001). Sorting of Golgi resident proteins into different subpopulations of COPI vesicles: a role for ArfGAP1. J Cell Biol 155, 1199-1212.

Lauwers, E., Jacob, C., and André, B. (2009). K63-linked ubiquitin chains as a specific signal for protein sorting into the multivesicular body pathway. J Cell Biol 185, 493-502.

Leblond, C.P. (1989). Synthesis and secretion of collagen by cells of connective tissue, bone and dentin. Anat Rec 224, 123-138.

Lee, C., and Goldberg, J. (2010). Structure of coatomer cage proteins and the relationship among COPI, COPII, and clathrin vesicle coats. Cell 142, 123-132.

Levi, S.K., Bhattacharyya, D., Strack, R.L., Austin, J.R., and Glick, B.S. (2010). The yeast GRASP Grh1 colocalizes with COPII and is dispensable for organizing the secretory pathway. Traffic 11, 1168-1179.

Levine, T.P., and Munro, S. (2001). Dual targeting of Osh1p, a yeast homologue of oxysterol-binding protein, to both the Golgi and the nucleus-vacuole junction. Mol Biol Cell 12, 1633-1644.

Lewis, M.J., Nichols, B.J., Prescianotto-Baschong, C., Riezman, H., and Pelham, H.R. (2000). Specific retrieval of the exocytic SNARE Snc1p from early yeast endosomes. Mol Biol Cell 11, 23-38.

Li, G. and Marlin, M.C. (2015). Rab Family of GTPases. In Rab GTPases, (Humana Press, New York, NY), pp. 115.

Lieu, Z.Z., and Gleeson, P.A. (2010). Identification of different itineraries and retromer components for endosome-to-Golgi transport of TGN38 and Shiga toxin. Eur J Cell Biol 89, 379-393.

Lin, C.H., MacGurn, J.A., Chu, T., Stefan, C.J., and Emr, S.D. (2008). Arrestin-related ubiquitin-ligase adaptors regulate endocytosis and protein turnover at the cell surface. Cell 135, 714-725.

Lin, S.X., Mallet, W.G., Huang, A.Y., and Maxfield, F.R. (2004). Endocytosed cation-independent mannose 6-phosphate receptor traffics via the endocytic recycling compartment en route to the trans-Golgi network and a subpopulation of late endosomes. Mol Biol Cell 15, 721-733.

Liu, K., Surendhran, K., Nothwehr, S.F., and Graham, T.R. (2008). P4-ATPase requirement for AP-1/clathrin function in protein transport from the trans-Golgi network and early endosomes. Mol Biol Cell 19, 3526-3535.

Llinares, E., Barry, A.O., and André, B. (2015). The AP-3 adaptor complex mediates sorting of yeast and mammalian PQ-loop-family basic amino acid transporters to the vacuolar/lysosomal membrane. Sci Rep 5, 16665.

Lock, J.G., and Stow, J.L. (2005). Rab11 in recycling endosomes regulates the sorting and basolateral transport of E-cadherin. Mol Biol Cell 16, 1744-1755.

Lorenz, M.C., and Heitman, J. (1995). TOR mutations confer rapamycin resistance by preventing interaction with FKBP12-rapamycin. J Biol Chem 270, 27531-27537.

Losev, E., Reinke, C.A., Jellen, J., Strongin, D.E., Bevis, B.J., and Glick, B.S. (2006). Golgi maturation visualized in living yeast. Nature 22, 1002-1006.

Lowe, M., and Kreis, T.E. (1995). In vitro assembly and disassembly of coatomer. J Biol Chem 270, 31364-31371.

Lu, R., and Drubin, D.G. (2017). Selection and stabilization of endocytic sites by Ede1, a yeast functional homologue of human Eps15. Mol Biol Cell 28, 567-575.

Luzio, J.P., Pryor, P.R., and Bright, N.A. (2007). Lysosomes: fusion and function. Nat Rev Mol Cell Biol 8, 622-632.

Ma, M., Burd, C.G., and Chi, R.J. (2017). Distinct complexes of yeast Snx4 family SNX-BARs mediate retrograde trafficking of Snc1 and Atg27. Traffic 18, 134-144.

Malhotra, V., Serafini, T., Orci, L., Shepherd, J.C., and Rothman, J.E. (1989). Purification of a novel class of coated vesicles mediating biosynthetic protein transport through the Golgi stack. Cell 58, 329-336.

Malsam, J., Satoh, A., Pelletier, L., and Warren, G. (2005). Golgin tethers define subpopulations of COPI vesicles. Science 307, 1095-1098.

Mani, S., and Thattai, M. (2016). Stacking the odds for Golgi cisternal maturation. Elife 5.

Mari, M., Geerts, W.J., and Reggiori, F. (2014). Immuno- and correlative light microscopy-electron tomography methods for 3D protein localization in yeast. Traffic 15, 1164-1178.

Martínez-Menárguez, J.A., Prekeris, R., Oorschot, V.M.J., Scheller, R., Slot, J.W., Geuze, H.J., and Klumperman, J. (2001). Peri-Golgi vesicles contain retrograde but not anterograde proteins consistent with the cisternal progression model of intra-Golgi transport. J Cell Biol 155, 1213-1224.

Matsudaira, T., Niki, T., Taguchi, T., and Arai, H. (2015). Transport of the cholera toxin B-subunit from recycling endosomes to the Golgi requires clathrin and AP-1. J Cell Sci 128, 3131-3142.

Matsuura-Tokita, K., Takeuchi, M., Ichihara, A., Mikuriya, K., and Nakano, A. (2006). Live imaging of yeast Golgi cisternal maturation. Nature 22, 1007-1010.

Maxfield, F.R., and McGraw, T.E. (2004). Endocytic recycling. Nat Rev Mol Cell Biol 5, 121-132.

McDonold, C.M., and Fromme, J.C. (2014). Four GTPases differentially regulate the Sec7 Arf-GEF to direct traffic at the trans-golgi network. Dev Cell 30, 759-767.

Menant, A., Barbey, R., and Thomas, D. (2006). Substrate-mediated remodeling of methionine transport by multiple ubiquitin-dependent mechanisms in yeast cells. EMBO J 25, 4436-4447.

Michelsen, K., Schmid, V., Metz, J., Heusser, K., Liebel, U., Schwede, T., Spang, A., and Schwappach, B. (2007). Novel cargo-binding site in the and subunits of coatomer. J Cell Biol 179, 209-217.

Miller, E.A., Beilharz, T.H., Malkus, P.N., Lee, M.C., Hamamoto, S., Orci, L., and Schekman, R. (2003). Multiple cargo binding sites on the COPII subunit Sec24p ensure capture of diverse membrane proteins into transport vesicles. Cell 114, 497-509.

Mironov, A.A., Weidman, P., and Luini, A. (1997). Variations on the intracellular transport theme: maturing cisternae and trafficking tubules. J Cell Biol 138, 481-484.

Misaki, R., Nakagawa, T., Fukuda, M., Taniguchi, N., and Taguchi, T. (2007). Spatial segregation of degradation- and recycling-trafficking pathways in COS-1 cells. Biochem Biophys Res Commun 360, 580-585.

Moelleken, J., Malsam, J., Betts, M.J., Movafeghi, A., Reckmann, I., Meissner, I., Hellwig, A., Russell, R.B., Sllner, T., Brgger, B., et al. (2007). Differential localization of coatomer complex isoforms within the Golgi apparatus. Proc Natl Acad Sci USA 104, 4425-4430.

Mogelsvang, S., Marsh, B.J., Ladinsky, M.S., and Howell, K.E. (2004). Predicting function from structure: 3D structure studies of the mammalian Golgi complex. Traffic 5, 338-345.

Morin-Ganet, M.N., Rambourg, A., Deitz, S.B., Franzusoff, A., and Képès, F. (2000). Morphogenesis and dynamics of the yeast Golgi apparatus. Traffic 1, 56-68.

Mowbrey, K., and Dacks, J.B. (2009). Evolution and diversity of the Golgi body. FEBS Lett 583, 3738-3745.

Munro, S. (1998). Localization of proteins to the Golgi apparatus. Trends Cell Biol 8, 11-15.

Myers, M.D., and Payne, G.S. (2013). Clathrin, adaptors and disease: insights from the yeast *Saccharomyces cerevisiae*. Front Biosci (Landmark Ed) 18, 862-891.

Nickerson, D.P., Russell, M.R., Lo, S.Y., Chapin, H.C., Milnes, J.M., and Merz, A.J. (2012). Termination of isoform-selective Vps21/Rab5 signaling at endolysosomal organelles by Msb3/Gyp3. Traffic 13, 1411-1428.

Nordmann, M., Cabrera, M., Perz, A., Bröcker, C., Ostrowicz, C., Engelbrecht-Vandré, S., and Ungermann, C. (2010). The Mon1-Ccz1 complex is the GEF of the late endosomal Rab7 homolog Ypt7. Curr Biol 20, 1654-1659.

Orci, L., Glick, B.S., and Rothman, J.E. (1986). A new type of coated vesicular carrier that appears not to contain clathrin: its possible role in protein transport within the Golgi stack. Cell 46, 171-184.

Orci, L., Malhotra, V., Amherdt, M., Serafini, T., and Rothman, J.E. (1989). Dissection of a single round of vesicular transport: sequential intermediates for intercisternal movement in the Golgi stack. Cell 56, 357-368.

Orci, L., Stamnes, M., Ravazzola, M., Amherdt, M., Perrelet, A., Söllner, T.H., and Rothman, J.E. (1997). Bidirectional transport by distinct populations of COPI-coated vesicles. Cell 90, 335-349.

Orci, L., Amherdt, M., Ravazzola, M., Perrelet, A., and Rothman, J.E. (2000a). Exclusion of Golgi residents from transport vesicles budding from Golgi cisternae in intact cells. J Cell Biol 150, 1263-1270.

Orci, L., Ravazzola, M., Volchuk, A., Engel, T., Gmachl, M., Amherdt, M., Perrelet, A., Söllner, T.H., and Rothman, J.E. (2000b). Anterograde flow of cargo across the Golgi stack potentially mediated via bidirectional "percolating" COPI vesicles. Proc Natl Acad Sci USA 97, 10400-10405.

Papanikou, E., and Glick, B.S. (2009). The yeast Golgi apparatus: insights and mysteries. FEBS Lett 583, 3746-3751.

Papanikou, E., and Glick, B.S. (2014). Golgi compartmentation and identity. Curr Opin Cell Biol 29, 74-81.

Papanikou, E., Day, K.J., Austin, J., 2nd, and Glick, B.S. (2015). COPI selectively drives maturation of the early Golgi. eLife 4, e13232.

Patterson, G.H., Hirschberg, K., Polishchuk, R.S., Gerlich, D., Phair, R.D., and Lippincott-Schwartz, J. (2008). Transport through the Golgi apparatus by rapid partitioning within a two-phase membrane system. Cell 133, 1055-1067.

Pawley, J.B. (2006). Handbook of Biological Confocal Microscopy, 3rd ed. (Springer).

Peden, A.A., Oorschot, V., Hesser, B.A., Austin, C.D., Scheller, R.H., and Klumperman, J. (2004). Localization of the AP-3 adaptor complex defines a novel endosomal exit site for lysosomal membrane proteins. J Cell Biol 164, 1065-1076.

Pelham, H.R. (1994). About turn for the COPs? Cell 79, 11125-11127.

Pelham, H.R.B. (1998). Getting through the Golgi complex. Trends Cell Biol 8, 45-49.

Pelham, H.R., and Rothman, J.E. (2000). The debate about transport in the Golgi–two sides of the same coin? Cell 102, 713-719.

Pelham, H.R. (2002). Insights from yeast endosomes. Curr Opin Cell Biol 14, 454-462.

Pellett, P.A., Dietrich, F., Bewersdorf, J., Rothman, J.E., and Lavieu, G. (2013). Inter-Golgi transport mediated by COPI vesicles carrying small cargoes. eLife 2, e01296.

Peplowska, K., Markgraf, D.F., Ostrowicz, C.W., Bange, G., and Ungermann, C. (2007). The CORVET tethering complex interacts with the yeast Rab5 homolog Vps21 and is involved in endo-lysosomal biogenesis. Dev Cell 12, 739-750.

Peyroche, A., Courbeyrette, R., Rambourg, A., and Jackson, C.L. (2001). The ARF exchange factors Gea1p and Gea2p regulate Golgi structure and function in yeast. J Cell Sci 114, 2241-2253.

Pfeffer, S. (2003). Membrane domains in the secretory and endocytic pathways. Cell 112, 507-517.

Phillips, M.J., and Voeltz, G.K. (2016). Structure and function of ER membrane contact sites with other organelles. Nat Rev Mol Cell Biol 17, 69-82.

Piper, R.C., Cooper, A.A., Yang, H., and Stevens, T.H. (1995). VPS27 controls vacuolar and endocytic traffic through a prevacuolar compartment in *Saccharomyces cerevisiae*. J Cell Biol 131, 603-617.

Prakash, S., Tian, L., Ratliff, K.S., Lehotzky, R.E., and Matouschek, A. (2004). An unstructured initiation site is required for efficient proteasome-mediated degradation. Nat Struct Mol Biol 11, 830-837.

Prescianotto-Baschong, C., and Riezman, H. (1998). Morphology of the yeast endocytic pathway. Mol Biol Cell 9, 173-189.

Prescianotto-Baschong, C., and Riezman, H. (2002). Ordering of compartments in the yeast endocytic pathway. Traffic 3, 37-49.

Prosser, D.C., Whitworth, K., and Wendland, B. (2010). Quantitative analysis of endocytosis with cytoplasmic pHluorin chimeras. Traffic 11, 1141-1150.

Puertollano, R., Aguilar, R.C., Gorshkova, I., Crouch, R.J., and Bonifacino, J.S. (2001). Sorting of mannose 6-phosphate receptors mediated by the GGAs. Science 292, 1712-1716.

Rabouille, C., Hui, N., Hunte, F., Kieckbusch, R., Berger, E.G., Warren, G., and Nilsson, T. (1995). Mapping the distribution of Golgi enzymes involved in the construction of complex oligosaccharides. J Cell Sci 108, 1617-1627.

Rabouille, C., and Klumperman, J. (2005). Opinion: The maturing role of COPI vesicles in intra-Golgi transport. Nat Rev Mol Cell Biol 6, 812-817.

Ren, Y., Yip, C.K., Tripathi, A., Huie, D., Jeffrey, P.D., Walz, T., and Hughson, F.M. (2009). A structure-based mechanism for vesicle capture by the multisubunit tethering complex Dsl1. Cell 139, 1119-1129.

Rink, J., Ghigo, E., Kalaidzidis, Y., and Zerial, M. (2005). Rab conversion as a mechanism of progression from early to late endosomes. Cell 122, 735-749.

Rossanese, O.W., Soderholm, J., Bevis, B.J., Sears, I.B., O'Connor, J., Williamson, E.K., and Glick, B.S. (1999). Golgi structure correlates with transitional endoplasmic reticulum organization in Pichia pastoris and *Saccharomyces cerevisiae*. J Cell Biol 145, 69-81.

Rossanese, O.W., Reinke, C.A., Bevis, B.J., Hammond, A.T., Sears, I.B., O'Connor, J., and Glick, B.S. (2001). A role for actin, Cdc1p, and Myo2p in the inheritance of late Golgi elements in *Saccharomyces cerevisiae*. J Cell Biol 153, 47-62.

Rothman, J.E. (1996). The protein machinery of vesicle budding and fusion. Protein Sci 5, 185-194.

Rothstein, R. (1991). Targeting, disruption, replacement, and allele rescue: integrative DNA transformation in yeast. Methods Enzymol 194, 281-301.

Ruiz-May, E., Kim, S.J., Brandizzi, F., and Rose, J.K. (2012). The secreted plant N-glycoproteome and associated secretory pathways. Front Plant Sci 3, 117.

Russ, J.C., and Neal, F.B. (2015). The Image Processing Handbook, Seventh Edition (Boca Raton, FL: CRC Press).

Sage, D., Donati, L., Soulez, F., Fortun, D., Schmit, G., Seitz, A., Guiet, R., Vonesch, C., and Unser, M. (2017). DeconvolutionLab2: an open-source software for deconvolution microscopy. Methods 115, 28-41.

Sahlmüller, M.C., Strating, J.R., Beck, R., Eckert, P., Popoff, V., Haag, M., Hellwig, A., Berger, I., Brügger, B., and Wieland, F.T. (2011). Recombinant heptameric coatomer complexes: novel tools to study isoform-specific functions. Traffic 12, 682-692.

Salama, N.R., Chuang, J.S., and Schekman, R. (1997). SEC31 encodes an essential component of the COPII coat required for transport vesicle budding from the endoplasmic reticulum. Mol Biol Cell 8, 205-217.

Santos, B., and Snyder, M. (1997). Targeting of chitin synthase 3 to polarized growth sites in yeast requires Chs5p and Myo2p. J Cell Biol 136, 95-110.

Sato, K., Sato, M., and Nakano, A. (2001). Rer1p, a retrieval receptor for endoplasmic reticulum membrane proteins, is dynamically localized to the Golgi apparatus by coatomer. J Cell Biol 152, 935-944.

Schlacht, A., Herman, E.K., Klute, M.J., Field, M.C., and Dacks, J.B. (2014). Missing pieces of an ancient puzzle: evolution of the eukaryotic membrane-trafficking system. Cold Spring Harb Perspect Biol 6, a016048.

Scott, P.M., Bilodeau, P.S., Zhdankina, O., Winistorfer, S.C., Hauglund, M.J., Allaman, M.M., Kearney, W.R., Robertson, A.D., Boman, A.L., and Piper, R.C. (2004). GGA proteins bind ubiquitin to facilitate sorting at the trans-Golgi network. Nat Cell Biol 6, 252-259.

Scott, C.C., Vacca, F., and Gruenberg, J. (2014). Endosome maturation, transport and functions. Semin Cell Dev Biol 31, 2-10.

Seals, D.F., Eitzen, G., Margolis, N., Wickner, W.T., and Price, A. (2000). A Ypt/Rab effector complex containing the Sec1 homolog Vps33p is required for homotypic vacuole fusion. Proc Natl Acad Sci U S A 97, 9402-9407.

Seaman, M.N. (2012). The retromer complex - endosomal protein recycling and beyond. J Cell Sci 125, 4693-4702.

Seaman, M.N., McCaffery, J.M., and Emr, S.D. (1998). A membrane coat complex essential for endosome-to-Golgi retrograde transport in yeast. J Cell Biol 142, 665-681.

Serafini, T., Orci, L., Amherdt, M., Brunner, M., Kahn, R.A., and Rothman, J.E. (1991). ADP-ribosylation factor is a subunit of the coat of Golgi-derived COP-coated vesicles: a novel role for a GTP-binding protein. Cell 67, 239-253.

Sesaki, H., and Jensen, R.E. (1999). Division versus fusion: Dnm1p and Fzo1p antagonistically regulate mitochondrial shape. J Cell Biol 147, 699-706.

Shaner, N.C., Campbell, R.E., Steinbach, P.A., Giepmans, B.N.G., Palmer, A.E., and Tsien, R.Y. (2004). Improved monomeric red, orange and yellow fluorescent proteins derived from Discosoma sp. red fluorescent protein. Nat Biotechnol 22, 1567-1572.

Sharpe, H.J., Stevens, T.J., and Munro, S. (2010). A comprehensive comparison of transmembrane domains reveals organelle-specific properties. Cell 142, 158-169.

Sherman, F. (1991). Getting started with yeast. Methods Enzymol 194, 3-21.

Shi, Y., Stefan, C.J., Rue, S.M., Teis, D., and Emr, S.D. (2011). Two novel WD40 domain-containing proteins, Ere1 and Ere2, function in the retromer-mediated endosomal recycling pathway. Mol Biol Cell 22, 4093-4107.

Singer-Krüger, B., Frank, R., Crausaz, F., and Riezman, H. (1993). Partial purification and characterization of early and late endosomes from yeast. Identification of four novel proteins. J Biol Chem 268, 14376-14386.

Singer-Krüger, B., Stenmark, H., Dsterhöft, A., Philippsen, P., Yoo, J.S., Gallwitz, D., and Zerial, M. (1994). Role of three Rab5-like GTPases, Ypt51p, Ypt52p, and Ypt53p, in the endocytic and vacuolar protein sorting pathways of yeast. J Cell Biol 125, 283-298.

Siniossoglou, S., and Pelham, H.R. (2001). An effector of Ypt6p binds the SNARE Tlg1p and mediates selective fusion of vesicles with late Golgi membranes. EMBO J 20, 5991-5998.

Sönnichsen, B., De Renzis, S., Nielsen, E., Rietdorf, J., and Zerial, M. (2000). Distinct membrane domains on endosomes in the recycling pathway visualized by multicolor imaging of Rab4, Rab5, and Rab11. J Cell Biol 149, 901-914. Spang, A. (2008). The life cycle of a transport vesicle. Cell Mol Life Sci 65, 2781-2789.

Spang, A. (2015). The Road not Taken: Less Traveled Roads from the TGN to the Plasma Membrane. Membranes (Basel) 5, 84-98.

Staehelin, L.A., and Kang, B.H. (2008). Nanoscale architecture of endoplasmic reticulum export sites and of Golgi membranes as determined by electron tomography. Plant Physiol 147, 1454-1468.

Stankunas, K., Bayle, J.H., Havranek, J.J., Wandless, T.J., Baker, D., Crabtree, G.R., and Gestwicki, J.E. (2007). Rescue of degradation-prone mutants of FK506-rapamycin binding (FRB) protein with chemical ligands. ChemBioChem 8, 1162-1169.

Stanley, P. (2011). Golgi glycosylation. Cold Spring Harb Perspect Biol 3, a005199.

Szul, T., and Sztul, E. (2011). COPII and COPI traffic at the ER-Golgi interface. Physiology 26, 348-364.

Séron, K., Tieaho, V., Prescianotto-Baschong, C., Aust, T., Blondel, M.O., Guillaud, P., Devilliers, G., Rossanese, O.W., Glick, B.S., Riezman, H., et al. (1998). A yeast t-SNARE involved in endocytosis. Mol Biol Cell 9, 2873-2889.

Takvorian, P.M., Buttle, K.F., Mankus, D., Mannella, C.A., Weiss, L.M., and Cali, A. (2013). The multilayered interlaced network (MIN) in the sporoplasm of the microsporidium Anncaliia algerae is derived from the Golgi. J Eukaryot Microbiol 60, 166-178.

Thor, F., Gautschi, M., Geiger, R., and Helenius, A. (2009). Bulk flow revisited: transport of a soluble protein in the secretory pathway. Traffic 10, 1819-1830.

Thuenauer, R., Hsu, Y.C., Carvajal-Gonzalez, J.M., Deborde, S., Chuang, J.Z., Römer, W., Sonnleitner, A., Rodriguez-Boulan, E., and Sung, C.H. (2014). Four-dimensional live imaging of apical biosynthetic trafficking reveals a post-Golgi sorting role of apical endosomal intermediates. Proc Natl Acad Sci U S A 111, 4127-4132.

Toret, C.P., and Drubin, D.G. (2006). The budding yeast endocytic pathway. J Cell Sci 119, 4585-4587.

Toshima, J.Y., Toshima, J., Kaksonen, M., Martin, A.C., King, D.S., and Drubin, D.G. (2006). Spatial dynamics of receptor-mediated endocytic trafficking in budding yeast revealed by using fluorescent alpha-factor derivatives. Proc Natl Acad Sci U S A 103, 5793-5798.

Toshima, J.Y., Nishinoaki, S., Sato, Y., Yamamoto, W., Furukawa, D., Siekhaus, D.E., Sawaguchi, A., and Toshima, J. (2014). Bifurcation of the endocytic pathway into Rab5-dependent and -independent transport to the vacuole. Nat Commun 5, 3498.

Tsui, M.M., and Banfield, D.K. (2000). Yeast Golgi SNARE interactions are promiscuous. J Cell Sci 113 (Pt 1), 145-152.

Tu, L., Tai, W.C., Chen, L., and Banfield, D.K. (2008). Signal-mediated dynamic retention of glycosyltransferases in the Golgi. Science 321, 404-407.

Valdivia, R.H., Baggott, D., Chuang, J.S., and Schekman, R. (2002). The yeast clathrin adaptor protein complex 1 is required for the efficient retention of a subset of late Golgi membrane proteins. Dev Cell 2, 283-294.

van Kempen, G.M.P., van Vliet, L.J., Verveer, P.J., and van der Voort, H.T.M. (1997). A quantitative comparison of image restoration methods for confocal microscopy. J Microsc 185, 354-365.

Velasco, A., Hendricks, L., Moremen, K.W., Tulsiani, D.R.P., Touster, O., and Farquhar, M.G. (1993). Cell type-dependent variations in the subcellular distribution of a-mannosidase I and II. J Cell Biol 122, 39-51.

Vida, T.A., and Emr, S.D. (1995). A new vital stain for visualizing vacuolar membrane dynamics and endocytosis in yeast. J Cell Biol 128, 779-792.

Viotti, C., Bubeck, J., Stierhof, Y.D., Krebs, M., Langhans, M., van den Berg, W., van Dongen, W., Richter, S., Geldner, N., Takano, J., et al. (2010). Endocytic and secretory traffic in Arabidopsis merge in the trans-Golgi network/early endosome, an independent and highly dynamic organelle. Plant Cell 22, 1344-1357.

von Blume, J., Alleaume, A.M., Kienzle, C., Carreras-Sureda, A., Valverde, M., and Malhotra, V. (2012). Cab45 is required for Ca2+-dependent secretory cargo sorting at the trans-Golgi network. J Cell Biol 199, 1057-1066.

Wach, A., Brachat, A., Pöhlmann, R., and Philippsen, P. (1994). New heterologous modules for classical or PCR-based gene disruptions in *Saccharomyces cerevisiae*. Yeast 10, 1793-1808.

Walch-Solimena, C., and Novick, P. (1999). The yeast phosphatidylinositol-4-OH kinase pik1 regulates secretion at the Golgi. Nat Cell Biol 1, 523-525.

Waters, M.G., Serafini, T., and Rothman, J.E. (1991). 'Coatomer': a cytosolic protein complex containing subunits of non-clathrin-coated Golgi transport vesicles. Nature 349, 248-251.

Wiederkehr, A., Avaro, S., Prescianotto-Baschong, C., Haguenauer-Tsapis, R., and Riezman, H. (2000). The F-box protein Rcy1p is involved in endocytic membrane traffic and recycling out of an early endosome in *Saccharomyces cerevisiae*. J Cell Biol 149, 397-410.

Willett, R., Ungar, D., and Lupashin, V. (2013). The Golgi puppet master: COG complex at center stage of membrane trafficking interactions. Histochem Cell Biol 140, 271-283.

Wong, M., and Munro, S. (2014). Membrane trafficking. The specificity of vesicle traffic to the Golgi is encoded in the golgin coiled-coil proteins. Science 346, 1256898.

Woodman, P.G. (2000). Biogenesis of the sorting endosome: the role of Rab5. Traffic 1, 695-701.

Yaffe, M.P., Jensen, R.E., and Guido, E.C. (1989). The major 45-kDa protein of the yeast mitochondrial outer membrane is not essential for cell growth or mitochondrial function. J Biol Chem 264, 21091-21096.

Yeaman, C., Le Gall, A.H., Baldwin, A.N., Monlauzeur, L., Le Bivic, A., and Rodriguez-Boulan, E. (1997). The O-glycosylated stalk domain is required for apical sorting of neurotrophin receptors in polarized MDCK cells. J Cell Biol 139, 929-940.

Yip, C.K., and Walz, T. (2011). Molecular structure and flexibility of the yeast coatomer as revealed by electron microscopy. J Mol Biol 408, 825-831.

Yu, I.M., and Hughson, F.M. (2010). Tethering factors as organizers of intracellular vesicular traffic. Annu Rev Cell Dev Biol 26, 137-156.

Yu, X., Breitman, M., and Goldberg, J. (2012). A structure-based mechanism for Arf1-dependent recruitment of coatomer to membranes. Cell 148, 530-542.

Zacharias, D.A., Violin, J.D., Newton, A.C., and Tsien, R.Y. (2002). Partitioning of lipid-modified monomeric GFPs into membrane microdomains of live cells. Science 296, 913-916.

Zanolari, B., Rockenbauch, U., Trautwein, M., Clay, L., Barral, Y., and Spang, A. (2011). Transport to the plasma membrane is regulated differently early and late in the cell cycle in *Saccharomyces cerevisiae*. J Cell Sci 124, 1055-1066.

Zaremba-Niedzwiedzka, K., Caceres, E.F., Saw, J.H., Bckstrm, D., Juzokaite, L., Vancaester, E., Seitz, K.W., Anantharaman, K., Starnawski, P., Kjeldsen, K.U., et al. (2017). Asgard archaea illuminate the origin of eukaryotic cellular complexity. Nature 541, 353-358.

Zerial, M., and McBride, H. (2001). Rab proteins as membrane organizers. Nat Rev Mol Cell Biol 2, 107-117.

Zhang, X., and Wang, Y. (2016). Glycosylation Quality Control by the Golgi Structure. J Mol Biol 428, 3183-3193.

Ziman, M., Chuang, J.S., and Schekman, R.W. (1996). Chs1p and Chs3p, two proteins involved in chitin synthesis, populate a compartment of the *Saccharomyces cerevisiae* endocytic pathway. Mol Biol Cell 7, 1909-1919.

Zink, S., Wenzel, D., Wurm, C.A., and Schmitt, H.D. (2009). A link between ER tethering and COP-I vesicle uncoating. Dev Cell 17, 403-416.

Zlatic, S.A., Grossniklaus, E.J., Ryder, P.V., Salazar, G., Mattheyses, A.L., Peden, A.A., and Faundez, V. (2013). Chemical-genetic disruption of clathrin function spares adaptor complex 3-dependent endosome vesicle biogenesis. Mol Biol Cell 24, 2378-2388.